Big
11/5/09

MODELLING OF THE ROTATIONAL MOULDING PROCESS FOR THE MANUFACTURE OF PLASTIC PRODUCTS

Lim Kok Khoon

A thesis submitted in partial fulfilment of the requirements of
The Nottingham Trent University for the degree of
Doctor of Philosophy

The research program was carried out in the
Faculty of Construction, Computing and Technology
School of Computing and Technology

December 2003

To my parent and my grandmother
with love and gratitude

ABSTRACT

The present research is mainly focused on two-dimensional non-linear thermal modelling, numerical procedures and software development for the rotational moulding process. The RotoFEM program is developed for the rotational moulding process using finite element procedures. The program is written in the MATLAB environment. The research includes the development of new slip flow models, phase change study, warpage study and process analyses. A new *slip flow methodology* is derived for the heat transfer problem inside the enclosed rotating mould during the heating stage of the tumbling powder. The methodology enables the discontinuous powder to be modelled by the continuous-based finite element method. The *Galerkin Finite Element Method* is incorporated with the *lumped-parameter system* and the *coincident node technique* in finding the multi-interacting heat transfer solutions inside the mould.

Two s*lip flow models* arise from the slip flow methodology; they are SDM (single-layered deposition method) and MDM (multi-layered deposition method). These two models have differences in their thermal description for the internal air energy balance and the computational procedure for the *deposition* of the molten polymer. The SDM model assumes the macroscopic deposition of the molten polymer bed exists only between the bed and the inner mould surface. On the other hand, the MDM model allows the layer-by-layer deposition of the molten polymer bed macroscopically. In addition, the latter has a more detailed heat transfer description for the internal air inside the mould during the powder heating cycle. In slip flow models, the semi-implicit approach has been introduced to solve the final quasi-equilibrium internal air temperature during the heating cycle. A notable feature of this slip flow methodology is that the slip flow models are capable of producing good results for the internal air at the heating powder stage, without the consideration of the powder movement and changeable powder mass. This makes the modelling of the rotational moulding process much simpler.

In the simulation of the cooling stage in rotational moulding, the thermal aspects of the inherent warpage problem and external-internal cooling method have been explored. The predicted internal air temperature profiles have shown that the less apparent crystallization plateau in the experimental internal air in practice could be related to warpage. Various phase change algorithms have been reviewed and compared, and thus the most convenient and considerable effective algorithm is proposed. The dimensional analysis method, expressed by means of dimensionless combinations of physical, boundary, and time variables, is utilized to study the dependence of the key thermal parameters on the processing times of rotational moulding. Lastly, the predicted results have been compared with the experimental results from two different external resources. The predicted temperature profiles of the internal air, oven times and other process conditions are consistent with the available data.

ACKNOWLEDGEMENTS

Firstly, I would like to express my sincere gratitude to Dr Anton Ianakiev for helping and supervising me throughout my PhD. Many thanks to him above all for his friendship, constructive advices, worthwhole discussions and supports throughout my PhD. His friendliness and technical expertise in the rotational moulding research have provided greater latitude to settle many doubts and questions in amicable, confident and effective manners.

Secondly, I am grateful to Prof. John Henshall for his remarks on my technical reports and many constructive suggestions and guidances on foregoing research objectives. I am also indebted to Dr Anton Ianakiev, Prof. John Henshall and Miss Judith Kipling, who have been providing an uncountable number of helps and comments on this thesis.

Thirdly, I am also thankful to The Nottingham Trent University for the sponsorship on this research. I would like to extend my gratitude to Mrs Doreen Corlett and other related staffs in this university for their information, helps, supports and hospitality.

The preface would not be complete without acknowledging my parent and my family for their continued supports that I received over the pass three years of my PhD. I deeply appreciate all the loving supports and cares from them, which have been essential driving forces throughout these years. Last but not least, I would especially thank to my friend Celine Yee for her encouragements and motivations during my PhD.

CONTENTS

Page No

ABSTRACT **I**

ACKNOWLEDGEMENTS **III**

CONTENTS **IV**

LIST OF FIGURES **VIII**

LIST OF TABLES **XIV**

NOMENCLATURE **XV**

CHAPTER 1 INTRODUCTION **1**

1.1 Rotational Moulding 1
1.2 Introduction to Engineering Plastics for Moulding Industries 5
1.3 Processing Stages of Rotational Moulding 7
1.4 Uniqueness of Rotational Moulding Process 9
1.5 Advantages of Rotational Moulding Process 10
1.6 Disadvantages of Rotational Moulding Process 10

CHAPTER 2 LITERATURE REVIEW **11**

2.1 Rotational Motion of Moulds 11
2.2 Heating and Cooling Methods of Rotational Moulding 12
2.3 Air Vent Pipes 14
2.4 Rotational Moulds 14
2.5 Induction and Fusion Times 16
2.6 Sintering and Densification of Polymers 18
2.7 Bubble Phenomenon 20
2.8 Shrinkage and Warpage of Plastic Products 20
2.9 Pressurization and Internal Cooling of Moulds 26
2.10 Flow Characteristics of Rotating Polymer Powder 27
2.11 Particle Segregation inside Rotational Moulds 30
2.12 Numerical Approaches and Process Control Systems of Rotational Moulding 31

2.13 Thermal Properties of Plastics 42
  2.13.1 Thermal Conductivity 42
  2.13.2 Density 44
  2.13.3 Specific Heat 44
2.14 Mechanism of Heat Transfer 45
  2.14.1 Heat Conduction Equation: Conductive heat transfer 46
  2.14.2 Boundary Conditions 47
2.15 Research Objectives 50

CHAPTER 3 FINITE ELEMENT METHOD AND MODELLING OF PHASE CHANGE 51
3.1 Finite Element Method (FEM) 51
  3.1.1 Spatial and Temporal Discretizations 54
  3.1.2 Galerkin Finite Element Method 54
3.2 Mathematical Expressions for Modelling of Phase Change 56
  3.2.1 Front-Tracking Techniques for Phase Changes 58
  3.2.2 Fixed-Domain Techniques for Phase Changes 59
  3.2.3 Categories of Fixed-Domain Techniques 60
    3.2.3.1 Enthalpy-based Approach 60
    3.2.3.2 Temperature-based Approach 61
    3.2.3.3 Source-based Approach 66
  3.2.4 Spatial and Temporal Averaging Techniques 67

CHAPTER 4 DEVELOPMENT OF NEW SLIP FLOW MODELS FOR ROTATIONAL MOULDING 69
4.1 Consideration of Slip Flow (Static-Bed Flow) Models 69
4.2 Description and Development of Slip Flow Models 71
  4.2.1 Single-layer Deposition Method (SDM) 73
  4.2.2 Multi-layer Deposition Method (MDM) 74
  4.2.3 Semi-implicit Approach for Internal Air of a Rotational Mould 74
4.3 Governing Equations of Rotational Moulding Process 75
  4.3.1 Heat Transfer within Mould 76
  4.3.2 Heat Transfer within Polymer 76

4.3.3 Initial Condition 76
4.3.4 Boundary Condition 1: Between external air and mould surface 76
4.3.5 Boundary Condition 2: Between mould and stagnant bed 77
4.3.6 Boundary Condition 3: Between innermost surface of static bed and internal air 77
4.3.7 Boundary Condition 4: At outermost surface of mixing bed or warpage problem 78
4.3.8 Heat Transfer within Internal Air (Ideal Gas Assumption) 78
4.4 External Heat Transfer Coefficients for Rotational Heating Processes 82

CHAPTER 5 IMPLEMENTATION OF FINITE ELEMENT METHOD FOR ROTATIONAL MOULDING FORMULATIONS, PHASE CHANGE AND WARPAGE 85
5.1 Galerkin Finite Element Approximation 85
5.1.1 Spatial Discretized Governing Equations 85
5.1.2 Eularian-Lagrangian Coordinate Transformation and Area Integration 88
5.1.3 Temporal Discretized Governing Equations 91
5.2 Numerical Implementation of Phase Change Algorithm 92
5.3 Coincident Node Technique 95

CHAPTER 6 RESULTS AND DISCUSSION 100
6.1 Geometry of Slip Flow Models 100
6.2 Determination of Average External and Internal Heat Transfer Coefficients 101
6.2.1 Perspective of Varying External Heat Transfer Coefficient for Slip Flow Models 104
6.3 Reliability of the Proposed Phase Change Algorithm 106
6.4 Internal Air Temperature: Model Verification and Indication of the Six Major Processing Stages 113
6.5 Numerical Simulations of Slip Flow Models 115
6.5.1 Results of Single-layer Deposition Method (SDM) 118
6.5.2 Results of Multi-layer Deposition Method (MDM) 118

6.6 Achievements of Slip Flow Models 122

6.6.1 Model Simplifications for Rotational Moulding Modelling 122

6.6.2 Prediction of Six Major Stages in a Rotational Moulding Cycle 124

6.7 Modelling of Warpage and Internal Cooling Processes 125

6.8 Dimensional Analysis of Process Parameters 142

CHAPTER 7 CONCLUSIONS 154

CHAPTER 8 FUTURE WORK 158

REFERENCES 159

LIST OF PUBLICATIONS 169

APPENDIX A BASIC VERIFICATION OF FINITE ELEMENT CODES 170

APPENDIX B RotoFEM PROGRAM STRUCTURE 172

B.1 Preface of RotoFEM Program 172

B.2 Structure of RotoFEM and Slip Flow Models 173

B.3 Data Input for RotoFEM Program 174

B.3.1 Primary Data Input of Heating Process 174

B.3.2 Primary Data Input of Cooling Process 174

B.4 Main Manual of RotoFEM Code 175

B.5 Flow Chart of RotoFEM Solution Procedure 177

LIST OF FIGURES

Page No

Figure 1-1 North American market sectors by product types of rotational moulding 3
Figure 1-2 European market sectors by product types of rotational moulding 3
Figure 1-3 General categories of plastic materials 6
Figure 1-4 Principal stages of a rotational moulding process 8
Figure 1-5 Biaxial rotation of a rotational mould 9

Figure 2-1 Regions in a rotational moulding cycle 17
Figure 2-2 Example of experimental temperature profiles for 2.7 *mm* part during a rotational moulding cycle 17
Figure 2-3 Heating zones in a powder mass 19
Figure 2-4 Cross-sectional view of convex, concave and irregular warpages 22
Figure 2-5 Convex warpage and concave warpage 23
Figure 2-6 Level of shrinkage by different cooling methods 25
Figure 2-7 Types of powder bed circulation 28
Figure 2-8 Idealized flow configuration for flow in a horizontal cylinder 32
Figure 2-9 Model of the melting mechanism for plastic powder 33
Figure 2-10 Model with well-mixed powder assumption 33
Figure 2-11 Superimposed heat transfer model 34
Figure 2-12 Example of predicted temperatures using moving plastic boundary 41
Figure 2-13 Example of predicted temperatures using well-mixed assumption 41
Figure 2-14 Classification of thermally conducting media in terms of their homogeneity and isotropy 43
Figure 2-15 Boundary conditions of a rectangular model in rectangular coordinates 48

Figure 3-1 Comparison of weighted residual methods 53 and variational principles

Figure 3-2 Variations of $H(T)$ and C_{eff} with temperature for isothermal phase change 62

Figure 3-3 Variations of $H(T)$ and C_{eff} with temperature for non-isothermal phase change 62

Figure 4-1 Axial motion of powder pools in a rotating mould 71

Figure 4-2 Geometrical domains of slip flow models 73

Figure 4-3 Thermal interaction of Mould/Static bed/Internal air 78

Figure 4-4 Thermal interaction of Mould/Internal air/Mixing bed 80

Figure 4-5 Thermal interaction of Deposited mixing bed/Internal air/Mixing bed 80

Figure 5-1 Eularian-Lagragian coordinate transformation 88

Figure 5-2 Relationship between Gauss integration points and possible phase change regions within an element 91

Figure 5-3 Structure of coincident node elements 95

Figure 6-1 Mesh generation for a $315\,mm$ x $315\,mm$ square model 101

Figure 6-2 Effects of external heat transfer coefficients on the temperature of an empty mould surface during a rotomoulding heating cycle 102

Figure 6-3 Comparisons between the experimental and predicted oven times for parts with different initial and deheating temperatures 103

Figure 6-4 Effects of external heat transfer coefficients on the temperature of an empty mould surface during a rotomoulding cooling cycle 104

Figure 6-5 Comparisons of external heat coefficients on predicted oven times for similar parts with the same initial and deheating temperatures 105

Figure 6-6 Comparisons of external heat coefficients on predicted cycle times for similar parts with the same initial and demoulding 106

temperatures
Figure 6-7 Experimental/Analytical type of effective polymer heat capacity for heating process 108
Figure 6-8 Experimental/Analytical type of effective polymer heat capacity for cooling process 108
Figure 6-9 Discrete type of effective polymer heat capacity for heating process 109
Figure 6-10 Discrete type of effective polymer heat capacity for cooling process 109
Figure 6-11 Experimental and discrete types of effective polymer thermal conductivity for heating and cooling processes 110
Figure 6-12 Experimental and discrete types of effective polymer density for heating process 110
Figure 6-13 Experimental and discrete types of effective polymer density for cooling process 111
Figure 6-14 Comparisons of phase change algorithms 111
Figure 6-15 Comparison between experimental and predicted external wall temperatures 114
Figure 6-16 Comparison between experimental and predicted internal air temperatures 115
Figure 6-17 Comparisons between experimental and predicted internal air temperatures of 2, 6 and 12 mm parts using SDM model (constant h_{ov}) 117
Figure 6-18 Comparisons between experimental and predicted internal air temperatures of 4 and 10 mm parts using SDM model (constant h_{ov}) 117
Figure 6-19 Comparisons between experimental and predicted internal air temperatures of 2, 6 and 12 mm parts using MDM model (varying h_{ov}) 119
Figure 6-20 Comparisons between experimental and predicted internal air temperatures of 4 and 10 mm parts using MDM model (varying h_{ov}) 119
Figure 6-21 Predicted temperature profiles of the internal air and various points across a 12 mm plastic bed using 120

	MDM model	
Figure 6-22	Comparisons of oven times over a range of oven temperatures for 2.7 *mm* part using MDM model	121
Figure 6-23	Predicted temperature profiles of the internal air and the 8 *mm* plastic bed at various points using SDM model	123
Figure 6-24	Predicted temperature profiles of the internal air and the 8 *mm* plastic bed at various points using MDM model	123
Figure 6-25(a)	Centre warpage - predicted temperature profiles across a 4 *mm* un-warped region during external cooling process	126
Figure 6-25(b)	Centre warpage - predicted temperature profiles across a 4 *mm* warped region during external cooling process	126
Figure 6-25(c)	Corner warpage - predicted temperature profiles across a 4 *mm* warped region during external cooling process	127
Figure 6-26	Comparison of the internal air temperatures between warped and un-warped 4 *mm* parts	127
Figure 6-27	Comparisons of cycle times between external cooling and external-internal cooling processes	130
Figure 6-28	Demoulding temperatures inside a 12 *mm* un-warped part for external cooling process	130
Figure 6-29	Demoulding temperatures inside a 12 *mm* centre-warped part for external cooling process	132
Figure 6-30	Demoulding temperatures inside a 12 *mm* corner-warped part for external cooling process	132
Figure 6-31	Demoulding temperatures inside a 12 *mm* un-warped part for external-internal cooling process	133
Figure 6-32	Demoulding temperatures inside a 12 *mm* centre-warped part for external-internal cooling process	134
Figure 6-33	Demoulding temperatures inside a 12 *mm* corner-warped part for external-internal cooling process	134
Figure 6-34	Comparisons of cycle times between warped and un-warped parts for external cooling process	135

Figure 6-35 Comparisons of cycle times between warped and un-warped problems for external-internal cooling process 135

Figure 6-36 Parametric contour plots of a 12 *mm* un-warped part during external cooling process 137

Figure 6-37 Parametric contour plots of a 12 *mm* un-warped part during external-internal cooling process 138

Figure 6-38 Parametric contour plots of a 12 *mm* centre-warped part during external cooling process 139

Figure 6-39 Parametric contour plots of a 12 *mm* corner-warped part during external cooling process 140

Figure 6-40 Parametric contour plots of a 12 *mm* centre-warped part during external-internal cooling process 141

Figure 6-41(a) Dimensionless heating time (Π_1) versus dimensionless plastics to mould thermal capacitance ratio (Π_3) 144

Figure 6-41(b) Dimensionless cycle time (Π_2) versus dimensionless plastics to mould thermal capacitance ratio (Π_3) 144

Figure 6-42(a) Dimensionless heating time (Π_1) versus dimensionless latent heat per unit volume for plastic phase change (Π_4) 145

Figure 6-42(b) Dimensionless cycle time (Π_2) versus dimensionless latent heat per unit volume for plastic phase change (Π_4) 145

Figure 6-43(a) Dimensionless heating time (Π_1) versus dimensionless plastic conductance (Π_5) 146

Figure 6-43(b) Dimensionless cycle time (Π_2) versus dimensionless plastic conductance (Π_5) 146

Figure 6-44(a) Dimensionless heating time (Π_1) versus dimensionless mould conductance (Π_6) 149

Figure 6-44(b) Dimensionless cycle time (Π_2) versus dimensionless mould conductance (Π_6) 149

Figure 6-45 Dimensionless cycle time (Π_2) versus dimensionless demoulding temperature (Π_7) 150

Figure 6-46 Dimensionless cycle time (Π_2) versus external heating to cooling heat transfer coefficient ratio (Π_8) 150

Figure 6-47(a) Dimensionless heating time (Π_1) versus internal air to external cooling heat transfer coefficient ratio (Π_9) 152

Figure 6-47(b) Dimensionless cycle time (Π_2) versus internal air to external cooling heat transfer coefficient ratio (Π_9) 152

Figure 6-48 Dimensionless cycle time (Π_2) versus air gap to external cooling heat transfer coefficient ratio (Π_{10}) 153

Figure A-1 Finite element mesh of the present eight-noded rectangular element 171

Figure A-2 Comparison between Kwon *et al.* and present results 171

LIST OF TABLES

		Page No
Table 6-1	Heat transfer coefficients for a range of rotomoulded parts of different thickness	102
Table 6-2	Discrete thermal properties of air, mould and polymer RP246H	107
Table 6-3	Physical and numerical representations of semi-crystalline polymers in rotational moulding process.	113
Table 6-4	Experimental process conditions and results for various rotomoulded parts	116

NOMENCLATURE

Symbol	Meaning	SI Unit
c	specific heat	$\mathrm{J\,kg^{-1}\,K^{-1}}$
$c_{a,p}$	specific heat of air at constant pressure	$\mathrm{J\,kg^{-1}\,K^{-1}}$
$c_{a,v}$	specific heat of air at constant volume	$\mathrm{J\,kg^{-1}\,K^{-1}}$
C_{app}	apparent heat capacity	$\mathrm{J\,m^{-3}\,K^{-1}}$
C_{eff}	effective heat capacity	$\mathrm{J\,m^{-3}\,K^{-1}}$
g	acceleration due to gravity	$\mathrm{m\,s^{-2}}$
h_{ex}	convective heat transfer coefficient at the interface of the external mould surface and the external air	$\mathrm{W\,m^{-2}\,K^{-1}}$
h_{in}	convective heat transfer coefficient at the interface of the innermost surface of the static bed (mixing bed and stagnant bed) and the internal air	$\mathrm{W\,m^{-2}\,K^{-1}}$
h_{oc}	convective heat transfer coefficient at the interface of the external mould surface and external cooling air	$\mathrm{W\,m^{-2}\,K^{-1}}$
h_{ov}	convective heat transfer coefficient at the interface of the external mould surface and the external heating air	$\mathrm{W\,m^{-2}\,K^{-1}}$
h_{int}	convective heat transfer coefficient at the interface of the coincident node elements	$\mathrm{W\,m^{-2}\,K^{-1}}$
H	volumetric enthalpy	$\mathrm{J\,m^{-3}}$
J	Jacobian matrix of coordinate transformation	-
$\hat{J}$	inverse Jacobian matrix of coordinate transformation	-
k	thermal conductivity	$\mathrm{W\,m^{-1}\,K^{-1}}$
L	latent heat per unit volume	$\mathrm{J\,m^{-3}}$
L_0	characteristic length	m
m	total mass of the internal air	kg
δm	total mass exchanges between the external and internal air	kg
$\dot{\delta m}$	mass exchange rate between the external	$\mathrm{kg\,s^{-1}}$

	and internal air	
n	unit outward normal from each surface	m
N	shape function	-
$\hat{R}$	residual for an equation	-
S_a	boundary of the innermost surface of the static bed and the internal air	m
S_{am}	boundary of the internal mould surface and the internal air	m
S_{ap}	boundary of the internal air and the outermost surface of the mixing bed	m
S_{ex}	boundary of the external mould surface and the external air	m
S_{mp}	boundary of the internal mould surface and the stagnant bed	m
S_{oc}	boundary of the external mould surface and the external cooling air	m
S_{ov}	boundary of the external mould surface and the external heating air	m
S_{pa}	boundary of the deposited mixing bed and the internal air	m
t	time	s
t_{cy}	cycle time	s
t_{ov}	heating (oven) time	s
T	temperature	K
T_a	quasi-equilibrium internal air temperature	K
T_o	initial internal air temperature	K
T_p	temperature at the innermost surface of the static bed	K
$\widetilde{T}_p$	temperature of the mixing bed	K
ΔT	temperature difference between two media	K
T_{am}	temperature at the internal mould surface	K

	which the surface faces the mixing bed	
T_{ap}	temperature at the outermost surface of the mixing bed	K
T_{cm}	crystalline melting temperature	K
T_{ex}	external/ambient (oven or cooling chamber) temperature	K
T_{pa}	temperature at the innermost surface of the deposited mixing bed	K
T_{map}	internal air temperature which receives the heat from the mould or the deposited mixing bed	K
T_{mpa}	internal air temperature which receives the heat from the innermost static bed	K
w	Gauss quadrature weightings	-
x, y	x, y coordinates	m
Gr	Grashof number	-
Nu	Nusselt number	-
Pr	Prandtl number	-
$[C]$	capacitance matrix	$\mathrm{J\ K^{-1}}$
$[K]$	stiffness matrix	$\mathrm{J\ s^{-1}\ K^{-1}}$
$\{F\}$	load vector	$\mathrm{J\ s^{-1}}$
β	volumetric coefficient of thermal expansion	$\mathrm{K^{-1}}$
δ_p	part thickness	m
μ	dynamic viscosity of fluid	$\mathrm{kg\ m^{-1}\ s^{-1}}$
v	thermal interactive fraction of internal air	-
ρ	density	$\mathrm{kg\ m^{-3}}$
ψ	weighted residual	-
max, min	maximum and minimum values	-
FEM	finite element method	-
SDM	single-layer deposition method	-
MDM	multi-layer deposition method	-
tWarp	total time since warpage begins.	s

Subscripts

a	internal air	-
l	liquid phase of polymer	-
m	mould	-
$\hat{m}$	mass fraction of polymer	-
p	polymer	-
s	solid phase of polymer	-
ex	parameter represents oc or ov for cooling or heating environment, respectively	-
mu	mushy phase of polymer	-
oc	cooling environment	-
ov	heating environment	-
tc	tacky phase of polymer	-
eff	effective	-
γ	parameter represents map or mpa	-
ξ,η	local coordinate	-
Γ	area	m^2
Ω	volume	m^3

Superscripts

e	element	-

CHAPTER 1

INTRODUCTION

1.1 Rotational Moulding

Rotational moulding, also known as rotocasting or rotomoulding, is a method for producing seamless, hollow, one-piece plastic articles by using heat and biaxial rotation. The process is regarded as transient, high-temperature, zero-pressure and low-shear [1,3,4]. Generally, the final rotomoulded part is considered to be pressure-free and stress-free since the process does not utilize pressure to force the melt into a mould shape. The concept of rotational moulding originated from 'slush moulding' in the polyvinyl (PVC) manufacturing process. The technology was first developed in the USA in the 1940's before it was brought in to the Europe in the 1950's [2,5].

In the initial years (early 1940's), the development of the rotational moulding process was limited due to there not being any suitable plastic materials and the cycle times were relatively long. At that time, the only ideal material for the industry was vinyl plastisol. In addition, there were only a few conferences and little published technical information regarding the process, particularly before the formation of the Association of Rotational Molder (ARM) in 1976 [2,4]. Furthermore, these factors had prevented new investors from venturing into the industry and existing moulders being able to improve their expertise.

In 1961, a more suitable ground Microthene polyethylene was produced by USI (Quantum Corporation) [8,9]. The invention of this powdered polyethylene stimulated the industry to grow steadily. This is because polyethylene is an ideal material for the rotational moulding owing to its low cost, excellent processing properties (e.g. powder flow, melt flow), resistance to longer processing time and thermal stability [8]. In the present rotational moulding industry, polyethylene (PE) has become the major material to be used, followed by plastisol. It accounts for over 90% of the total tonnage of plastics used in the industry [10]. Further improvements in PE's stiffness and temperature resistance, however, are still needed to keep it as this industry's material of choice. In the meantime, any shortcomings on the mechanical properties of PE or rotomoulded materials, such as stiffness, can be readily overcome through the use of *geometrical features* [10].

In the 1960's, the rotational moulding process was limited to the toy industry. This was because the early types of rotomoulded polymer PVC and polyethylene had relatively low strength and stiffness. To improve the situation, cross-linkable grades of polyethylene, and special grades of nylon, ABS, polycarbonate, etc have been developed. Today, the industry has managed to diversify its markets into different sectors (mass-produced products, higher value articles and high-tech applications) according to recent surveys as shown in Figures 1-1 and 1-2 [2]. The process is now being recognized as one of the most versatile manufacturing methods for producing a wide range of thermoplastic products, in particular for the part thicknesses between 0.5–13 mm. This can be attributed to the fact that a rotomoulded part can be made as small as a doll's eye and as large as a 100 000 litre storage tank [8,11,14]. Rotomoulded parts, however, are often produced with wall thinkness of between 2 and 8 mm.

Generally speaking, the rotational moulding process is very ideal for a relatively short

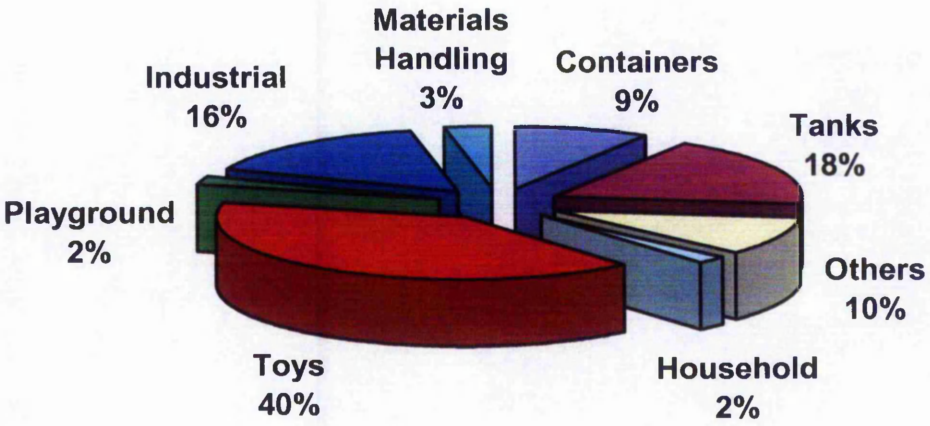

Figure 1-1: North American market sectors by product types of rotational moulding [2]

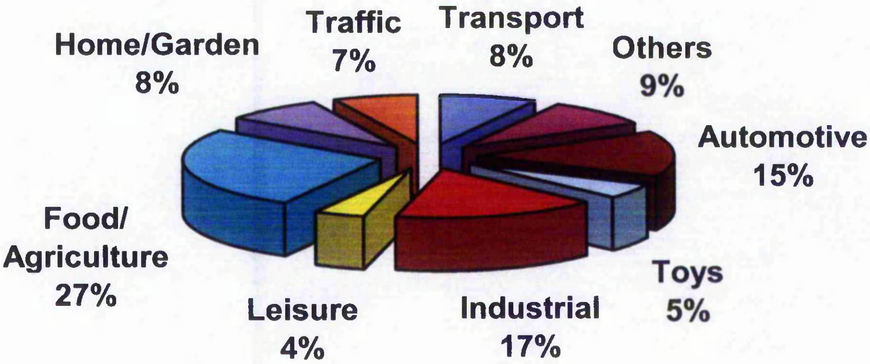

Figure 1-2: European market sectors by product types of rotational moulding [2]

run production. It is regarded as having low processing cost in 100 000-300 000 parts per year range, and competes well with the other plastic moulding processes through to 1 000 000 parts per year [13]. To date, the rotational moulding industry is a fast growing process with an average growth rate of 10% annually. This is because a relatively low capital cost is required, the availability of suitable raw materials and technical advances, and its process adaptability for manufacturing different sizes [1,2]. For the North American market alone, it already had a market value of about US$1250 million in 1995 and escalated to US$1650 million in 1997 [2]. To further enhance the future advancement of rotational moulding (other than ARM), the Society of Plastic Engineers (SPE) had also chartered the Rotational Moulding Division in 2000 in order to promote technical discussion about the rotational moulding process [2]. With the current encouraging growth rate, technical advances and new types of machines, the process has turned into an alternative to injection moulding, twin-sheet thermoforming and blow moulding (main competitor), especially for producing large hollow parts.

The rotational moulding, blow moulding and twin-sheet thermoforming processes are still limited in their ability to produce product with moulded-in open holes. They require secondary machining operations to produce small holes, large openings, critical dimensions, etc. A CNC (Computer Numerically Controlled) router [4] can be used to perform these features for increasing the manufacturing accuracy and reliability at a lower cost. The rotational moulding industry is indeed still lagging behind the other two in adopting the CNC router, making the process more labour intensive. The adoption of these automated routers is inevitable in the future machine developments. This will help the rotational moulding industry to produce progressively and economically and to be more competitive in the industry of hollow article. In spite of the CNC limitation, rotational moulding is the best of these processes for moulding parts that require a uniform wall thickness, a high degree of toughness/impact strength (low residual stress), large inserts, multi-material layers and a mix of multiple moulds [4].

1.2 Introduction to Engineering Plastics for Moulding Industries

Ranges of engineering plastics are now available to the plastic moulding industries. The plastics that have been developed to cater for the rotational moulding process include polyethylene, plastisol, polycarbonate, polystyrene, polypropylene, polyamide, nylon, Hytrel and Ethylene Vinyl Acetate (EVA) [5,13,15]. The general categories of plastic materials can be classified as those listed in Figure 1-3 [16]. About 80% of the worldwide plastic consumption is thermoplastics, despite the fact that thermosets have better physical properties. This is because of the thermoplastics' low cost, ease of processing and broad range of mechanical/thermal properties [2,3,10]. In the rotational moulding industry, thermoplastics are also the primary raw material, followed by a limited extent of thermosetting materials.

In thermosets, heat must be applied to them in order to *cure* the materials. The process is associated with a chemical process of crosslinking. It is an irreversible chemical process that transforms them into infusible polymer. Thus, the cured plastics cannot be recycled by conventional means. On the other hand, thermoplastics can undergo physical change via a simple physical process of melting and freezing without involving any chemical reaction. The process is reversible, therefore, the scraps (regrinds) are recyclable after grinding into powder. Thermoplastics are solidified through the removal of heating (i.e. latent heat release). In the solid phase they are generally tougher, less rigid and have poorer thermal properties than thermosets [2,12,15,16,20].

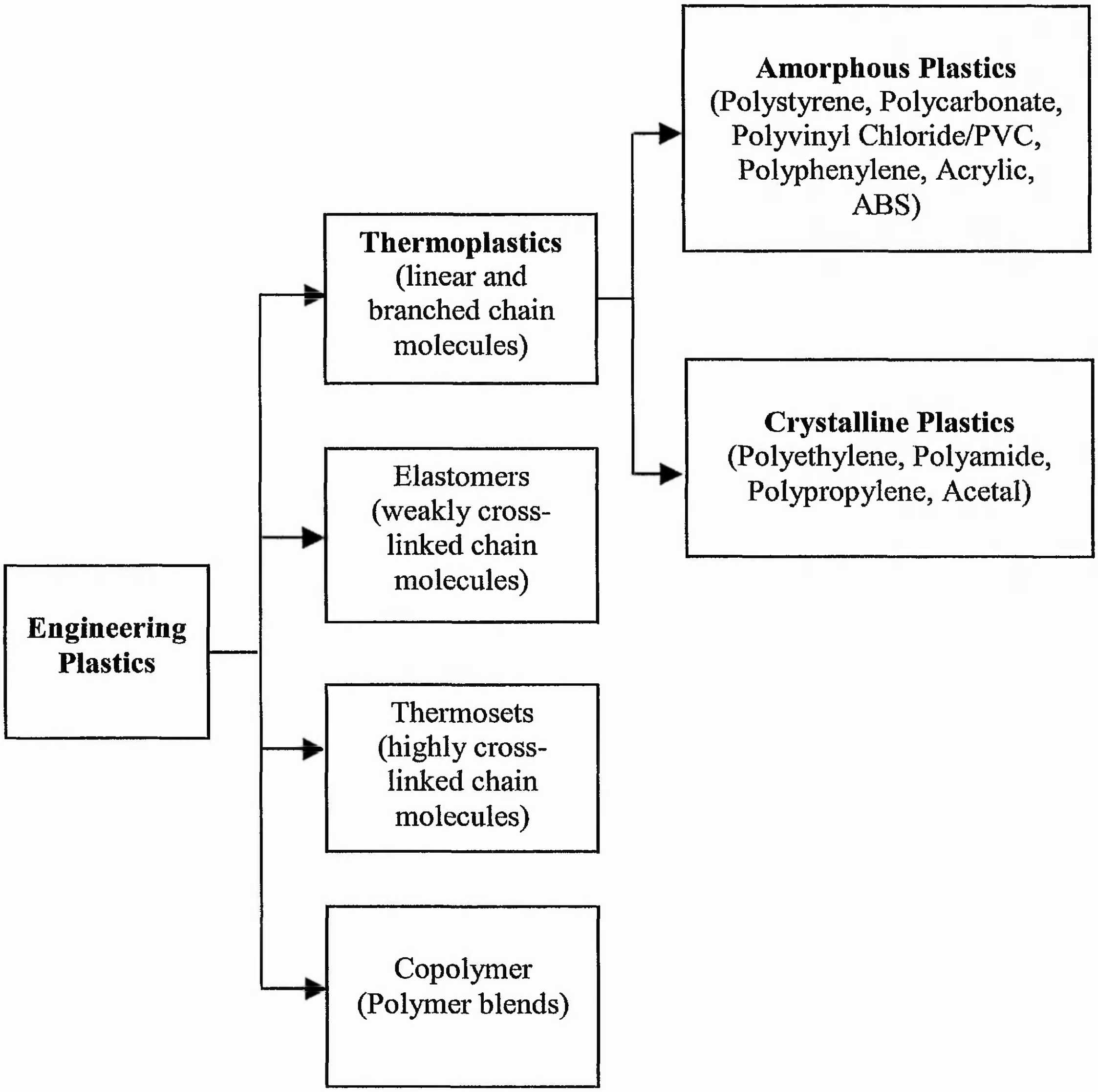

Figure 1-3: General categories of plastic materials [16]

According to the Figure 1-3, thermoplastic materials can be further categorized into amorphous and crystalline groups of plastics. The amorphous polymers contribute only little to the rotational moulding industry, as compared with the crystalline polymers. Under normal conditions (room temperature), the former are brittle and the latter are tough and elastic [16]. From the heat transfer viewpoint, the crystalline/semi-crystalline and amorphous polymers are different in terms of:

(i) Crystalline or semi-crystalline polymers (e.g. polyethylene): Generate latent heat upon solidification and exhibit a freezing range. Rate of cooling, chemical structure and thermal history in the post-moulded state will decide the degree of crystallation. One of the advantages of the semi-crystalline products is that the crystalline structure helps to enhance the mechanical properties such as toughness, elasticity and permeability. The 'tacky' temperature is about equal to the polymer melt temperature [2].

- Characteristics of Polyethylene: Tough, light weight (less dense than water [16]), flexibility, excellent chemical resistance, excellent electrical insulating properties and ease of processing [3,4].

(ii) Amorphous polymers (e.g. polystyrene): Do not undergo crystallisation. During the phase change process, amorphous polymers undergo a physical change from melt to rubber and to glass. The 'tacky' temperature is about equal to or slightly greater than the glass transition temperature of the polymer [2]. The rate of cooling has only little effect on its physical properties, since there is no crystal growth control involved [1].

1.3 Processing Stages of Rotational Moulding

Loading, heating, cooling and unloading are the four principal stages in the rotational moulding process as depicted in Figure 1-4. At the loading station (Figure 1-4 a), an empty mould is filled with a pre-measured plastic powder with a typical particle size distribution from -30 mesh (500 microns) to +200 mesh (70 microns) [2]. The closed mould is then heated up in an oven while subjected to a biaxial motion (Figures 1-4 b and 1-5) with a relatively low rotational speed at about 4–20 rpm or 0.07–0.33 Hz [18].

A release agent will be sprayed onto the inner surface of a mould before the heating process begins to improve the releasability of final product. The most common classes of release agent are *transient*, *semi-permanent* and *permanent* release agents [10].

The heating cycle (Figure 1-4 b) is accomplished by heating up the mould and plastic powder contained therein at an oven set-point temperature of about 250–375 ^0C (482–707 ^0F). The powder tumbles, softens, compounds, melts, coalesces and intermittently coats onto the inner surface of the rotating mould at its tacky temperatures of about 100–130 ^0C, which depends on type and amount of polymer used. The powder, therefore, undergoes gradual change of physical, mechanical, thermal and rheological properties. The heating process continues until all the powder particles are completely fused and formed into the mould shape. At this stage, a homogeneous (monolithic) liquid layer of polymer is produced. The hot mould is then removed from

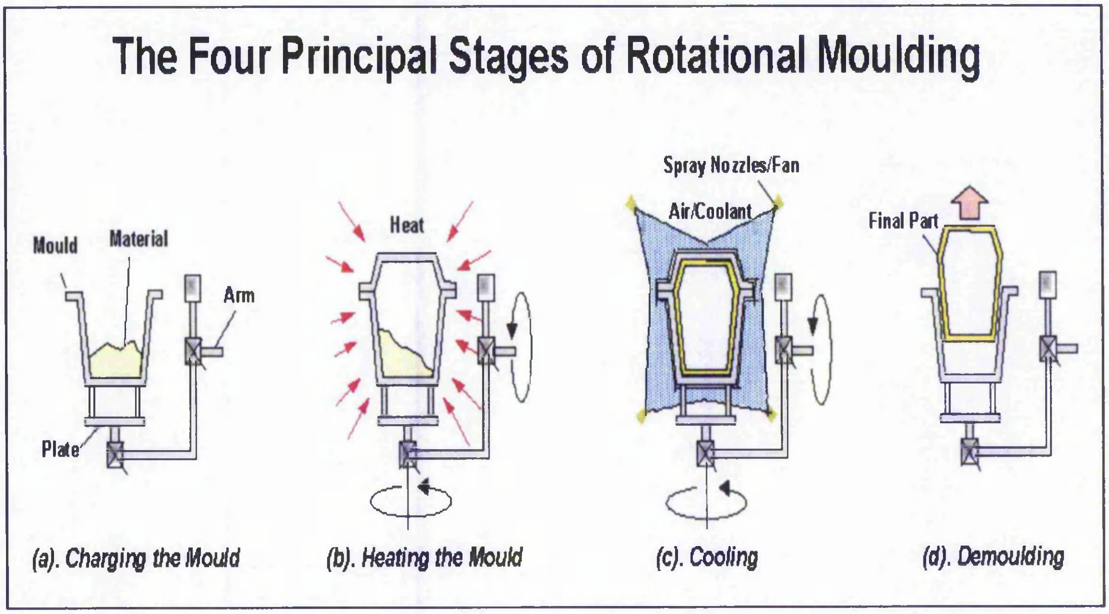

Figure 1-4: Principal stages of a rotational moulding process
(Illustration – courtesy of R.J.Crawford, Queen's University - Belfast)

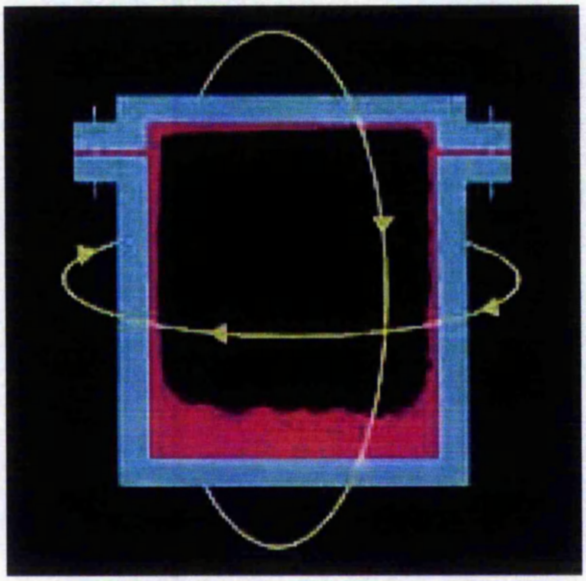

Figure 1-5: Biaxial rotation of a rotational mould [17]

the heating oven into a cooling chamber. During heating cycle, inserts and surface textures (i.e. wood grain, leather grain) are indeed allowed to be moulded-in. In addition, features such as logos or operating instructions can also be moulded onto the surfaces of products as well [5].

Inside the cooling chamber (Figure 1-4 c), the still-rotating mould is quenched. At this stage, the biaxial rotating motion of mould helps the molten part to maintain its shape until it has enough strength to retain the mould shape at a temperature that around 50–80 ^0C. The temperature at that time is termed the *demoulding temperature*. Finally, the mould is discharged (Figure 1-4 d) from the cooling bay. The rigid part is removed to end the entire rotational moulding cycle.

1.4 Uniqueness of Rotational Moulding Process [3]

(i) Use of biaxial rotation of the moulds.

(ii) Use of liquid plastisols or thermoplastic powders instead of pellets.

(iii) Apply heat instead of pressure or force to melt the materials.

(iv) Produce single-part hollow product.

1.5 Advantages of Rotational Moulding Process [2,3]

(i) Low investment cost in terms of a relatively simple machinery design.

(ii) Low tooling cost (due to low pressure) and quick to make.

(iii) Final products are stress free, no weld lines and no injection mark.

(iv) Little scrap is produced.

(v) Capability to produce parts with complex shape, thick wall and appropriate even/uneven wall thickness easily and economically.

(vi) Multiple moulds with different shapes and sizes can be moulded at the same time.

1.6 Disadvantages of Rotational Moulding Process [2,3,9]

(i) Formation of internal bubbles.

(ii) An obvious warpage or shrinkage might occur on fast quenching.

(iii) Long cycle time

(iv) Not suitable for products requiring high precision (i.e. 99.99% uniform parts).

(v) Relatively higher cost of materials; the materials are first produced in pellets and then ground to fine powder.

(vi) Relatively shorter mould lifetime compared with injection or blow moulding; the exteriors of the mould and its mounting assemblies are exposed to oxidizing atmospheres over a very wide range of temperature [9].

CHAPTER 2

LITERATURE REVIEW

2.1 Rotational Motion of Moulds

Rotational moulding is not a centrifugal casting process, as the centre of gravity of most moulds does not pass through the axes of rotation. Most mould surfaces are also not equidistant from the centre of rotation. Any *centrifugal forces* generated inside a mould would result in large variations in wall thickness of any rotomoulded part. This is because the forces generated by the high rotational speeds will cause the molten polymer to flow towards the highest force concentration rather than to distribute itself evenly about the entire mould surface. Care should also be taken in using large loads with high speed as the *gyroscopic forces*, created by the rotation of high inertial loads about two perpendicular axes, will cause a serious damage to the mould machine [12].

During the moulding process, two-axial (major and minor axes) rotation of a rotomoulded mould aims to ensure that the heating process is optimal at all parts of the mould surface and the melt forms a uniform coating on all interior mould surfaces throughout the entire moulding cycle. Generally, these major and minor axes are at 90^0 angles for simplification of mechanical design [4]. The major axis refers to the arm, which rotates around the X-axis, and the minor axis refers to the arm, which rotates around the Y-axis (Figure 1-4). For an even distribution of polymer on the mould walls, the best commonly practiced speed ratio (arm/plate) is usually 4:1 between the major and minor axes of rotation. The speed ratio can be determined by the Equation (2-1) in the unit of rpm [12,14,21].

$$\text{Speed ratio} = \frac{R_1}{R_2 - R_1} \qquad (2\text{-}1)$$

The symbols R_1 and R_2 signify the major-axis speed and minor-axis speed, respectively. In fact, the speed ratio of rotation can also be utilized to control the formation of an uneven thickness of a part, by bringing the portion of the mould surface to its inner powder pool more frequent [22].

2.2 Heating and Cooling Methods of Rotational Moulding

The heating temperature is a primary factor affecting part quality during the heating cycle. To provide fast heating with minimum part degradation, this temperature is set depending on the polymer type, part thickness and heating method [3]. Too higher heating temperature may cause product degradation and discolouration at the outer surface of an article but leave the inner layers unmelted. This is because the effectiveness of the heating cycle is often retarded by the poor thermal conductivity of the polymers [2,3,10,13]. Consequently, these undesirable phenomena lead to losses in physical properties of the plastics. They can be minimized by continuously purging an inert gas such as nitrogen or helium, into the mould during the heating cycle. In these cases, the moulding occurs in an oxygen-free environment [4]. An adequate flow of nitrogen will produce a non-oxidized, light-coloured interior to the moulded parts [10].

The heating process of rotational moulding can be performed by methods such as open-flame heating, hot-air recirculating oven (oven-heating), internal air heating, molten salts, hot-oil jacketed mould, infrared-red or electrical heating. Among them, the oven-heating method is the most popular today. In actual fact, the open-flame heating method was the first introduced to the rotational moulding industries in the early 1940's.

However, it was gradually changed to the oven-heating method owing to the conveniences the latter offers; for example, cleanliness, health and safety and mould design flexibility [6,7,23]. These advantages ensure the method still dominates the market today. Unfortunately, the oven-heating method was found very inefficient since only 1.7% of the heat generated would go to the polymer. This is because the method requires the oven air to be heated up before heating the mould. So the oven-heating method is relatively incompatible in the context of energy saving. Consequently, the approach results extra energy consumption mainly caused by significant energy losses to the surrounding and machine parts [6,7].

In open-flame heating, an alternative and favoured heating approach, heat is directly transferred to the mould from one or more flames. Scott and Crawford [24] found that the efficiency of the open-flame heating was related to the type of flame, gas flow rate and proximity of the burner to the mould (ideally 50–90 *mm* from mould). Research by Kearn [6] showed that the open-flame heating method helped to expedite the heating time; but its overall cycle time was still longer than the oven-heating method. This is the trade-off between an effective heating time and a long cooling time. It is also one of the reasons that the oven heating is favoured over the open flame method.

The applicable cooling methods for rotational moulding can be fan blowing (external forced convection), external-internal cooling, mist sprays, water showers, cold air jets and then spraying the moulds with water after a determined time and ambient air. From these, the fan blowing method is the most common cooling method used in the industry. Although the water spraying method helps to expedite the cooling, it is efficient only when the mould surface is hot enough (~100^0C) to evaporate the spray.

2.3 Air Vent Pipes

The rotational moulding process is a method to produce open-ended articles, therefore, its moulds can be fixed at one end with at least one vent pipe. The vent pipe aims to release the hot or cold air inside a mould to the mould's external surrounding. This helps to produce a stress-free product and to maintain the atmospheric pressure inside the mould, which prevent blowout. The common available vent pipes are disposable polytetrafluoroethlyene tubes (PTFE, Teflon) and steel pipes. In practice, the pipe is usually packed with glass or wire wool to minimize powder flows down the pipe and out into the oven [2,3].

Good venting of the mould will minimize flash and part/mould distortion [3]. Quantitatively, the mathematical expression of vent pipe diameter, *d*, for a cubical mould is given as [2]:

$$d = \sqrt{\frac{4*0.59\left[D-2*\left(\frac{\rho_p}{\rho_B}\right)h\right]^3}{60\pi v\left(\frac{D}{1000}\right)^{0.1}\times(h+2h^{0.2})}} \qquad (2\text{-}2)$$

where D is the side of the cube, h is part thickness, v is the gas speed in the vent pipe, ρ_p is the solid density of polymer, and ρ_B is the bulk density of the powder. The pipe diameter has an inverse relationship to the part thickness. For a $1\,m^3$ cubical mould, $d = 25mm$ and $d = 20mm$ are recommended for $6\,mm$ and $10\,mm$ thick parts, respectively.

2.4 Rotational Moulds

Aluminium and steel moulds are the most common types of rotomoulding cavities. A mould can be manufactured by at least four different processes:

(i) Casting,

(ii) Fabricating,

(iii) Electroforming,

(iv) Machining.

The method of choice is much depends on type, size and shape of mould for the product's application [2,4]. Additionally, the casting process can be further diversified into atmospheric, pressure and vacuum castings [2].

Cast aluminium moulds are commonly used by today rotomoulders due to being lightweight with good thermal conductivity and ability to be cast into complex shapes. The fabricated mould is the second choice for moulders. The fabricated mould is usually built by master craftspeople using materials such as mild steel, stainless steel and aluminium. The technique is best for large but simple parts. For highly detail parts and where liquid vinyl is used to produce parts, electroformed nickel moulds are recommended. Finally, machined moulds are an option to achieve a desirable level of precision for a simple shaped article.

Different thickness of a mould is usually required for strength as well as efficient heating and cooling. Under the same mould rigidity and quenching condition, steel cools more rapidly than aluminium. The efficiency can be determined by using the well-known dimensionless group – '*Fourier number*', $\frac{\alpha t}{L^2}$ [2,29,30].

$$\left[\frac{\alpha t}{L^2}\right]_{\text{steel}} > \left[\frac{\alpha t}{L^2}\right]_{\text{aluminum}} \qquad (2\text{-}3)$$

where t is time and L is the mould thickness. Although the aluminium has better thermal diffusivity, α, than steel, it requires a thicker wall (roughly 5 times greater) to compensate for its relatively lower strength, σ, and rigidity, G. Thus this readily overcomes the disparity in α.

2.5 Induction and Fusion Times

As depicted in Figure 2-1, the time required for heating a mould to reach the melt temperature of a polymer is termed the '*induction time*' or '*build-up time*' [1,12,14]. On the other hand, the duration from the beginning of the subsequent second phase until all the heating powder is completely coalesced and fused to end the heating cycle, is known as the '*fusion time*' [1,12,14,25]. Sun and Crawford [43] pointed out that the air inside the mould is hotter than the plastic powder during this induction period. In 1990, this phenomenon was indeed observed by Nugent [14] as shown in Figure 2-2. Thus, the powder is expected to be heated up by both the mould wall and its internal air at the same time.

Ramazzati listed the influencing parameters for the induction time as follows [1]:

(i) Heat transfer medium
(ii) Oven temperature
(iii) Velocity of heating medium
(iv) Melt temperature of polymer
(v) Mould wall thickness
(vi) Mould surface to volume ratio
(vii) Oven recovery time

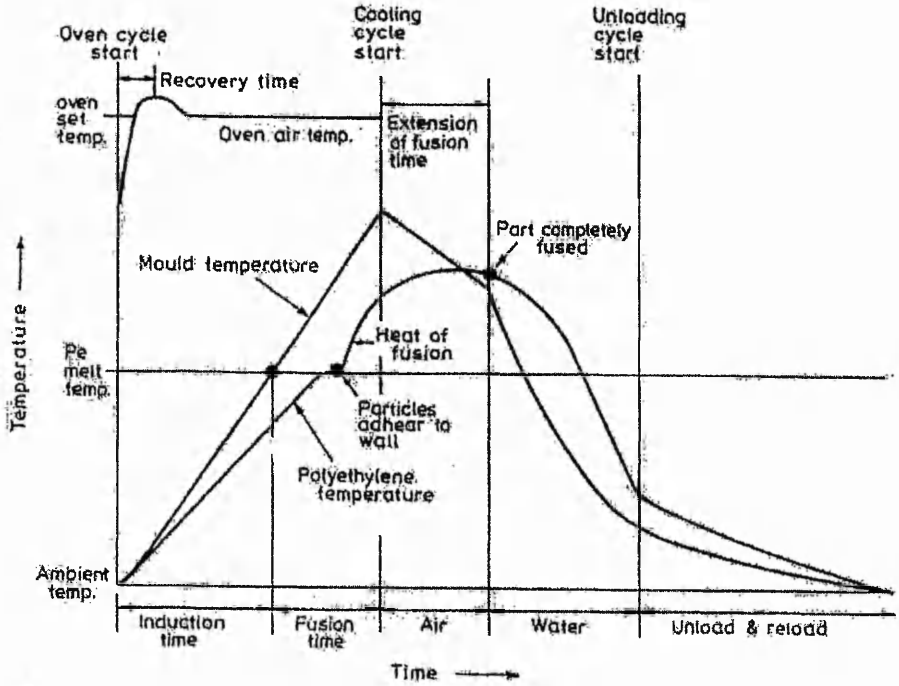

Figure 2-1: Regions in a rotational moulding cycle [14]

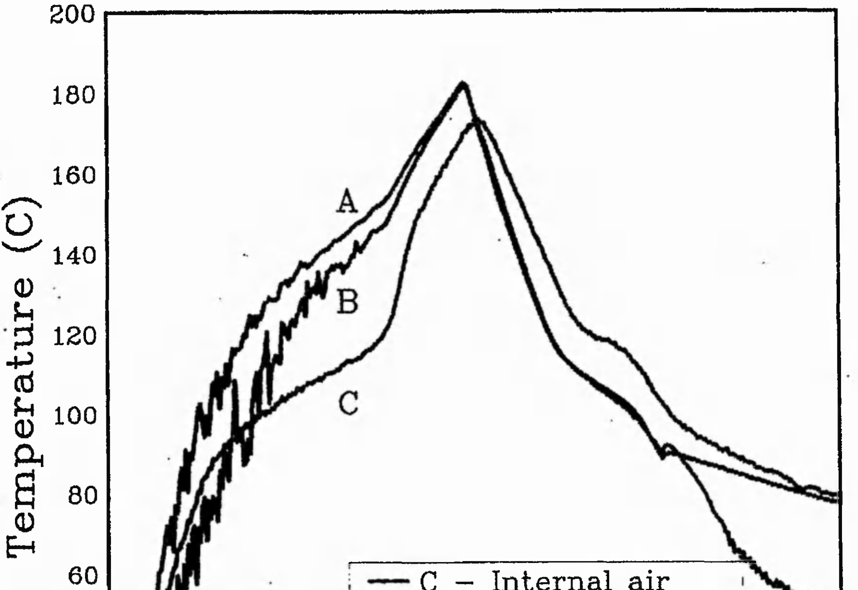

Figure 2-2: Example of experimental temperature profiles for 2.7 mm part during a rotational moulding cycle [14]

whereas the important factors for the fusion time included:

(i) Wall thickness of part

(ii) Oven temperature

(iii) Velocity of heating medium

(iv) Mould surface to volume ratio

(v) Particle size of the polymer

(vi) Mould heat capacity per unit area

2.6 Sintering and Densification of Polymers

Heating, sintering and densification of polymer powder accompany the heating cycle of the rotational moulding process. The evolution of a polymer from powder to molten polymer is diagrammatically sketched in Figure 2-3. In most materials, the sintering time is much longer than densification time, especially for those with a high degree of viscoelasticity [9]. Rao and Throne [9] suggested that the formation of a homogeneous layer starts from sintering and densification phases.

(i) Sintering (Coalescence): A stage where the powder particles reach their tacky temperature. These particles stick and agglomerate together to form a porous three-dimensional network. They are usually characterized by a little change in density of mass [9].

(ii) Densification (Fusion): At some point of fusion process, the 3-D network of the porous polymer begins to collapse into the void spaces. This is associated with the formation and dissolution of bubbles. These spaces are filled with molten polymer that is drawn into the region by *capillary forces* (i.e. microscopic flow of the polymer, which fills the voids between individual polymer particles [25]).

In 1982, Progelhof *et al.* [25] claimed a complete densification process occurs in three distinct stages:

- Melting,
- Bubbles migration & collapse,
- Levelling.

They urged that using small particles could minimize the phenomenon of levelling. Besides, it could also help to reduce the initial size of voids within the molten polymer. Throne *et al.* [9] suggested that the most mouldable powder particle would be cubic in shape with generously rounded corners and between 35 and 75 mesh size. The 'powder tail' should be avoided to prevent detrimental part properties.

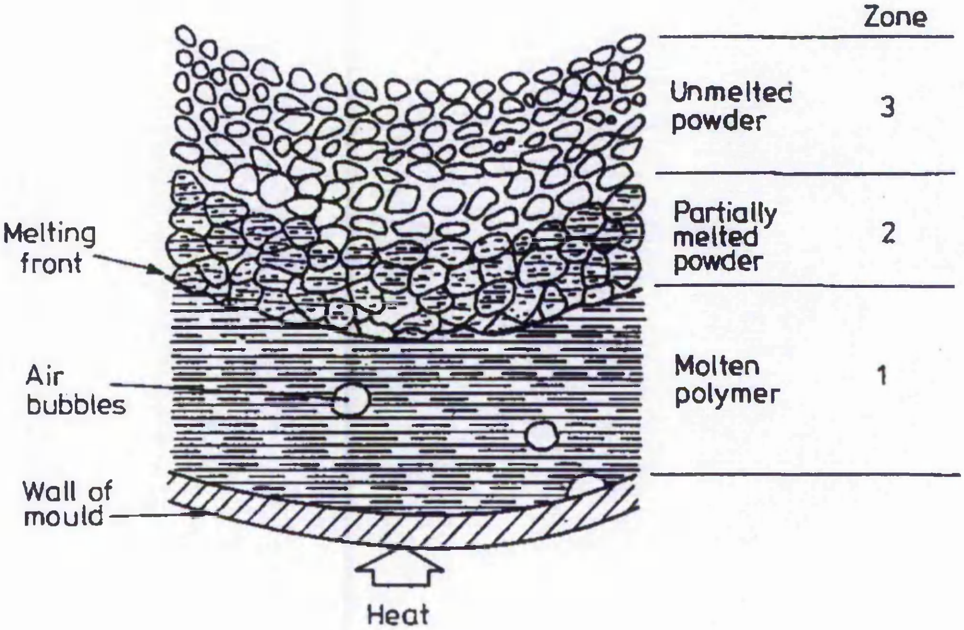

Figure 2-3: Heating zones in a powder mass [14]

2.7 Bubble Phenomenon

The presence of bubbles is an inherent defect in rotationally moulded products. Thus the optimum heating cycle should be based on the melting of polymer powder and the time required for the bubbles to migrate from the molten polymer [25]. In practice, some moulders do use the bubble density in a slice of moulded products as an indication of quality. A slice with too many bubbles or no bubbles indicates the moulding is undercured or overcured, respectively. In contrast, a slice with a small number of bubbles close to the inner free surface is usually regarded as a desired situation (i.e. less degradation). In addition, the appearance of the inner surface of a part and the smell of the interior of the moulding can be used to assess the quality of a rotationally moulded part [2]. For example, an 'undercooked' part will show powdery or rough feature on its inner surface, and an 'overcooked' part will show glossy inner surface, which is usually accompanied by an acrid smell.

2.8 Shrinkage and Warpage of Plastic Products

Global shrinkage and warpage are still the unsolved problems of rotational moulding. They start at the *crystalline melting temperature*. The problems not only prolong the cycle time but also lead to deterioration in the product quality. A product that experiences shrinkage will decrease in size. Warpage is known as a distortion where the surfaces of moulded part do not follow the intended cavity shape. The level of shrinkage is controlled by the rate of cooling, whereas warpage is influenced by the magnitude of temperature gradients across a product [26].

In 1989, Iwakura, *et al.* [29,30] correlated the thermal quench stresses to the mechanisms of warpage formation. Later, Chen *et al.* [27,28] performed a fundamental experimental study on the mechanisms of warpage and shrinkage of rotationally moulded polyethylene. They proposed mould pressurization as a method to reduce warpage. Further to the above investigations, Bawisker and White [31] made comparative studies of warpage, global shrinkage and residual quench stresses across a series of rotomoulded thermoplastics. They concluded that the levels of warpage and global shrinkage increase with the degree of crystallization of the polymer (i.e. HDPE > LDPE). In 1998, Liu and Ho. [32] examined the effect of various processing parameters on the mechanism of warpage and proposed the *structure buckling model* to simulate the measured warpages. More recently, Gogos *et al.* [37] introduced a one-dimensional (1-D) theoretical heat transfer model to simulate and to identify the key processing parameters of rotomoulding which affect warpage.

Part warpage is usually due to differential shrinkage of a product that may be induced by the type of material used, inappropriate design of the mould and processing conditions. It can be minimized or prevented if the shrinkage throughout a part is uniform or the cooling rates on the inside and outside surfaces of the plastic are the same. The former seems to be impossible because of rotational moulding process asymmetry. The latter is often retarded by the common practice in a single sided process of rotational moulding; for example, the heat transfer mechanism is utilized only from the external mould surface while leaving the potential control from the inner mould 'un-engined' [9,26,29,30,36,39,57]. Strictly speaking, it is very difficult to keep both the inner and outer surfaces of a part at the same cooling rate [26].

As schematically illustrated in Figure 2-4, warpage can be further categorized into three major types; concave, convex and irregular (combination of concave and convex at a

(a) Convex (Positive) Warpage

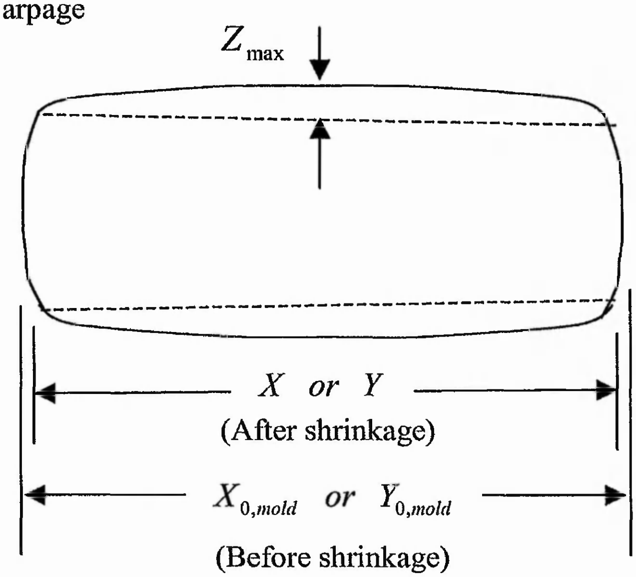

(b) Concave (Negative) Warpage

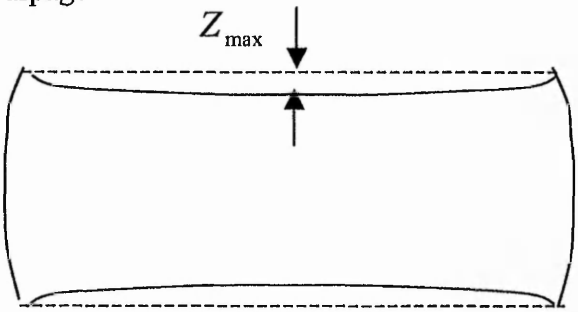

(c) Irregular Warpage

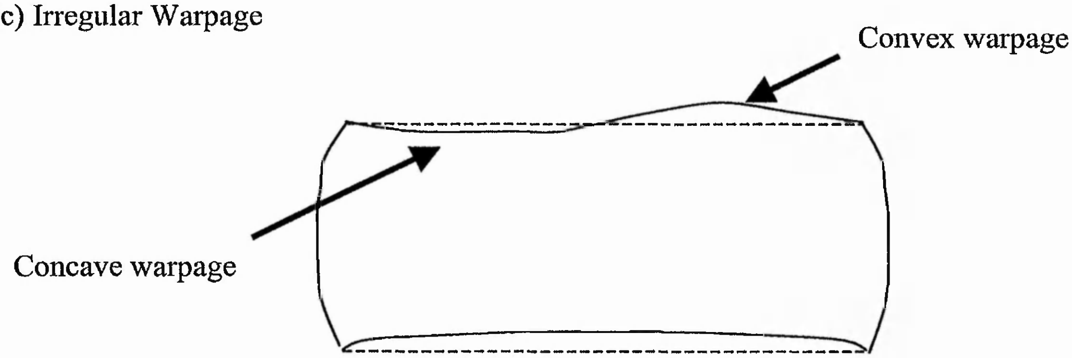

Figure 2-4: Cross-sectional view of convex, concave and irregular warpages

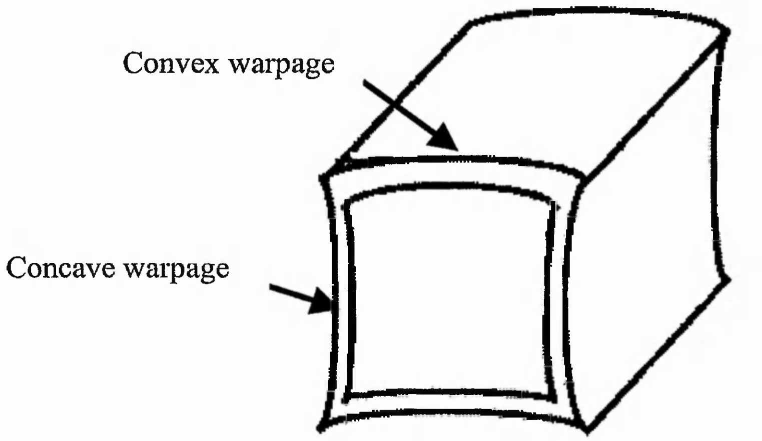

Figure 2-5: Convex warpage and concave warpage [32]

part surface) [30,32]. Liu *et al.* [32] suggested that the warpages of rotomoulded parts may be due to three different sources:

(i) Unbalanced *residual stress* through the part thickness (i.e. convex/positive warpage)

(ii) Geometric effect as in Figure 2-5 (i.e. convex/positive warpage)

(iii) Bucking of part surfaces (i.e. concave/negative or irregular warpage)

According to Liu *et al.* [32], unbalanced residual stress (thermal quench stress) through a part thickness is the source of *convex/positive warpage*. The unbalanced stress is as a result of the one-sided cooling process; the outside surface of the part is first cooled while the inner surface remains hot. So the stress tends to balance itself by deforming the part. In addition, the convex warpage can also be caused by the *geometric comer affect* (Figure 2-5), which results from the bending moment effect of the mould. The *concave/negative warpage* or an *irregular warpage* is due to the buckling of rotomoulded part. It happens when a hot mould shrinks faster than its moulded part during a rapid quenching. This is because a relatively quickly shrunken mould will exert a *compressive force* on the hot, soft plastic part. The compressive force, therefore, causes the part to buckle and warp. In contrast, when the temperature gradient between the mould and part is small, the problem rarely happens. The reason is that the part shrinks faster than the mould; this only occurs when the *thermal expansion coefficient* of the plastic is larger than that of mould, which is usually the case.

There are number of experimental studies [26-35,37] on the warpage problem. Consequently, the effect of process parameters on warpage can be summarized as the following:

(i) Warpage increases with the increase of temperature gradients across moulded part, polymer density, level of release agent, oven temperature and Fourier number.

(ii) Warpage decreases with the increase in part thickness [26,32], venting hole's dimension and pressurization.

Shrinkage is a function of process conditions, primarily cooling rate and wall thickness [3]. The global shrinkage is accompanied by circumferential residual stresses in the walls of the part as well as microscopic shrinkage [30]. Crystalline and semi-crystalline materials are more prone to thermal shrinkage (i.e. HDPE > LLDPE), whereas amorphous materials tend to shrink less [39]. Shrinkage increases when the wall thickness of a part increases. This is because a slow cooling rate encourages the formation of a high degree of crystalline material, which gives high levels of molecular orientation [39]. This makes shrinkage easier but warpage difficult.

It is worth noting that the off-line experiments by Chen [28] showed a part

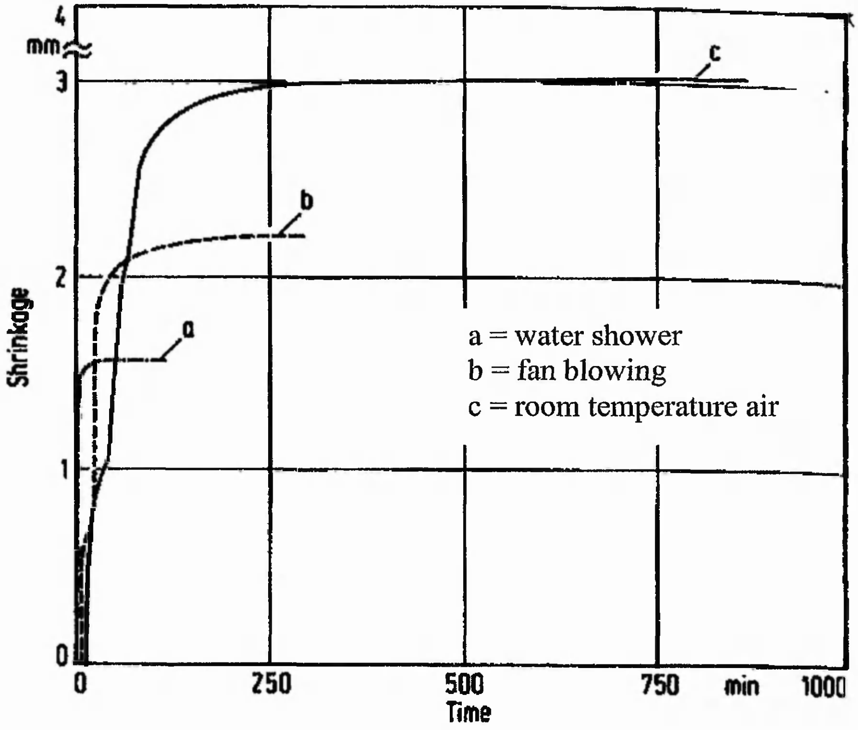

Figure 2-6: Level of shrinkage by different cooling methods [28]

experiencing more rapid shrinkage at the beginning of a fast cooling method such as water shower (Figure 2-6). However, the shrinkage level of the fast cooling test was overshadowed by slow cooling test after some time. This could probably be explained from the viewpoint of the above-mentioned molecular orientation. Since the warpage and shrinkage problems are inter-correlated, it is possible to relate the observations in Figure 2-6 to Crawford and Walls paper [26], which says warpage may occur some time after the moulding process. Macroscopically, it is because of the residual stress inside the plastic part.

According to Iwakura *et al.* [30], the measurements on warpage and shrinkage can be mathematically represented by the Equations (2-4)–(2-6) below (refer to Figure 2-4).

(i) Warp Temperature (WT): The temperature at which an unacceptable amount of component distortion occurs.

(ii) Warpage [27,30]: The deflection of the centre surface of a moulded part from a straight line essentially connecting the two ends of the mould.

- Maximum Warpage, $\varepsilon_{\max} = \dfrac{Z_{\max}}{X}$ *or* $\dfrac{Z_{\max}}{Y}$ (2-4)

(iii) Shrinkage [27,30]: Microscopic shrinkage is defined as densification due to crystallization. Global shrinkage is the percent reduction in dimensions of the longest length of the moulded part.

- Global Shrinkage, X-direction, $\gamma_x = \dfrac{X}{X_{0,mold}}$ (2-5)

- Global Shrinkage, Y-direction, $\gamma_y = \dfrac{Y}{Y_{0,mold}}$ (2-6)

2.9 Pressurization and Internal Cooling of Moulds

The experimental results from Chen *et al.* [27] showed that the mould pressurization reduced shrinkage and warpage had no detrimental effect on the mechanical behaviour of a polyethylene product produced by rotational moulding. Only a little change in the plastic density was observed with mould pressurization. Since the density distribution determines the residual stresses, the mould pressurization also has no effect on the residual stresses either. In addition, the mould pressurization also helps to remove bubbles and further consolidates the melt. Consequently, it can improve the material properties, for example up to a 25% increase in impact strength and 5% in tensile strength [33].

According to Crawford [40] the mould pressurization could speed up the sintering process and the internal cooling could reduce the warpage. However, any unbalanced mould pressurization might lead to an uneven part thickness and result in further warpage. A high mould pressure will create large forces that might blow the mould apart. Thus the imposed pressure should be just enough to hold the plastic against the mould wall until its mechanical properties are strong enough to resist any thermal quench stresses.

2.10 Flow Characteristics of Rotating Polymer Powder

The kinematics of a revolving mould and the energy exchanges between the enclosed polymer and its surroundings are the key aspects of the rotational moulding process [22]. Both factors contribute to the process optimisation such as the distribution of powder into the shaped mould and uniformity of wall part thickness [10,22,45]. With a low speed of mould rotation, the powder particles remain in the bottom of the mould. These powder particles are not still but are free to flow and mix vigorously inside the rotating mould for the first-third of the heating cycle [18]. An understanding of the general flow mechanisms and characteristics of the tumbling polymer powder is crucial to develop a new rotational moulding model for better predictions.

Coulomb flow powder and *viscous flow powder* are the most general kinds of tumbling powders commonly found in a revolving system. For *Coulomb flow powders*, the particles remain in continuous contact with their neighbours in any situation. On the other hand, *viscous flow powders* will experience steady-state powder flow and mixing [2]. Observation through a glass mould showed that the *powder motio*n in a rotating system could be categorized into three major types - circulation, slip-flow and avalanche, which are diagrammatically illustrated in Figure 2-7.

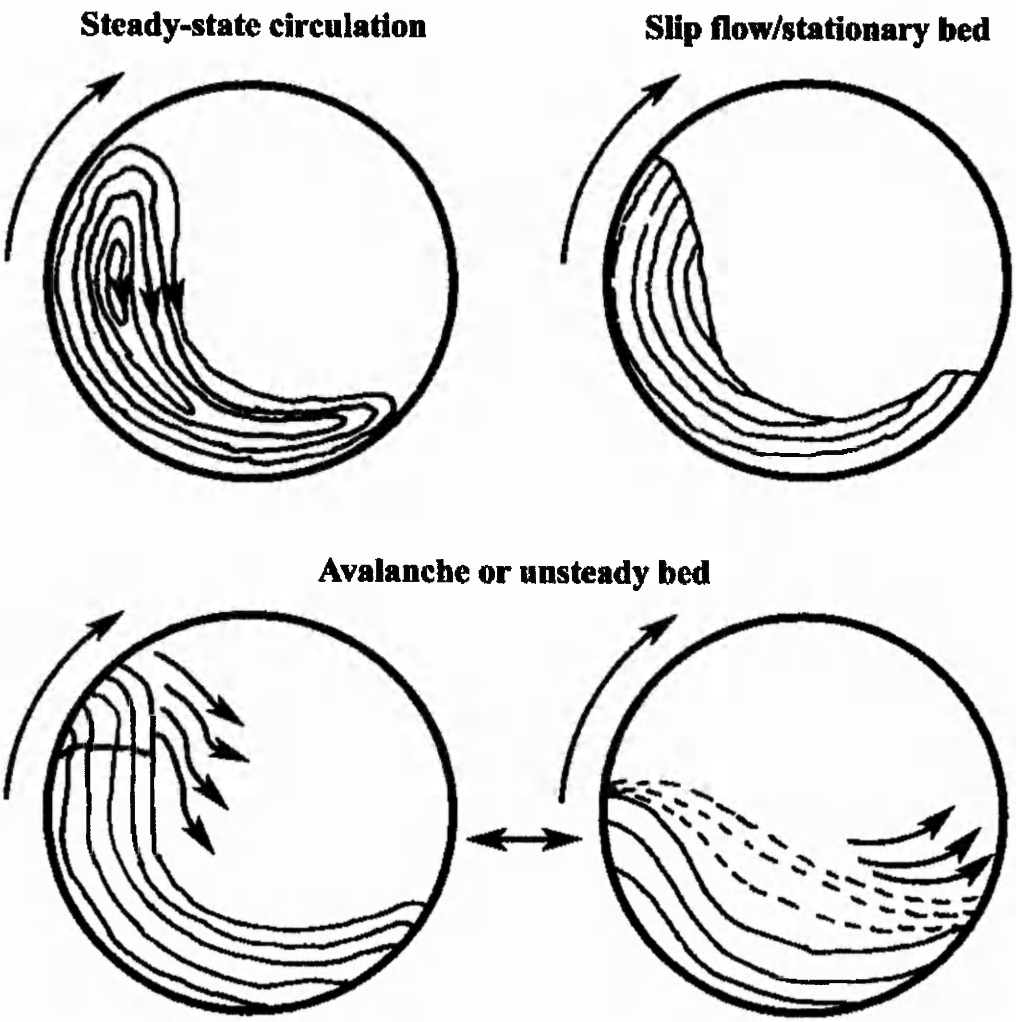

Figure 2-7: Types of powder bed circulation [2]

The flow motions of the tumbling powder can be broadly described as follows [2,18,19]:

(i) Steady-state circulating bed flow: The powder at the mould surface moves with the mould surface until the dynamic angle of repose reaches approximately 25^{0} – 50^{0}. At the point, the gravitational force overcomes the powder resistance to flow, and the friction between the mould surface and the powder particles is much greater than the internal friction between particles. Therefore, the steady-state bulk powder breaks away from the mould wall and cascades across the static surface of the powder bed to provide a maximum mixing. This phenomenon is often observed when the mould surface is rough, the particle sizes are quite large, and the powder volume is moderate when compared with the mould volume. Powders that exhibit this circulating flow are classified as *viscous flow powders*.

(ii) Slip flow or Static bed flow: This type of flow occurs when the mould surface is very smooth. It involves *no powder mixing* since the powder is treated as a monolithic structure and the particle-to-particle interactions of the powder are considered insignificant. The powder bed is initially static with respect to the mould surface. As the mould raises the powder bed to a point where the friction between the mould surface and the powder bulk is no longer sufficient to overcome the shearing forces provided by the tumbling of the mould. The bulk will slide against the mould surface. This implies that the friction between the mould surface and the powder bulk is substantially less than the internal friction between particles of the bulk. This is because of the bulk of powder has sufficient cohesiveness to overcome the shearing forces. The cohesiveness in powders might come from irregularly shaped particles, *Van der Waal* forces and sticky or tacky surfaces. Powders that exhibit slip flow are classified as *Coulomb flow powders*.

(iii) Avalanche or unsteady bed: The friction between the mould surface and the powder particles is sufficient to allow the bed to intermittently move with the mould surface. As a certain height is reached, the bed structure collapses and a major portion of the powder flows across the remaining static bed leading to relatively good powder mixing. The periodicity of the avalanche is independent of the speed that the drum rotates and the powder characteristics, but it does depend on the drum diameter. Since the avalanche flow is *unsteady-state*, the powder cannot be classified either as Coulomb flow or viscous flow.

In the context of theoretical and numerical difficulties, the Avalanche flow is the most complex to model. This is because the flow is in an unsteady-state. The second most difficulty flow pattern to model is the steady-state circulating bed flow, while the slip-bed flow is the easiest. In 1972, Roa and Throne [9] developed the first *circulating-bed-flow model* to predict the mould and plastic temperatures. Later in 1976, Throne [44] published a comparatively simple *static-bed-flow model.* The model worked better than the circulation model, and is the forerunner of the static model used today.

2.11 Particle Segregation inside Rotational Moulds

A revolving mould often causes *particle segregation* [18,46] in the mould, where particles of similar size, density or surface roughness form clusters inside the mould. Increase in the powder frictional coefficient discourages segregation. Generally, the time to the segregation is strongly dependent on:

(i) The rate of rotation of the mould
(ii) The volume fraction of the mould filled with powder - only in early stages of segregation

Segregation is only desired for industries such as the manufacturer of transparent or translucent lighting fixtures, where larger dimensioned polymer pieces are added to the polymer as diffusers. The phenomenon becomes undesirable when powder uniformity is essential to give uniform material properties [18].

2.12 Numerical Approaches and Process Control Systems of Rotational Moulding

In the rotational moulding industry, rotomoulders are mainly concerned with the length of times that the parts undergo heating and cooling. This is because these times will affect the total production time and the final product qualities. The primitive trial-and-error methods for determining the heating and cooling cycles are considered inefficient, time-consuming and expensive, in terms of labour, material wastage and equipment wastage. Fortunately, the air temperature inside the mould has been found to be useful for the optimisation of the process times [14].

A number of numerical approaches had also been developed to further simulate, investigate, understand and improve the process. Figures 2-8 to 2-11 [9,14,38,45] illustrate the existing numerical concepts, which have been used to model one-dimensional (1-D) and two-dimensional (2-D) heat transfer mechanisms of the rotational moulding. However, they all have their own advantages and drawbacks such as analytical limitations, numerical complexities, computational efforts or accuracy of predicted results.

In 1972, Roa and Throne [9] proposed a complicated *Goodman circulation model* describing heat transfer to powder and powder flow (circulating bed flow) inside a revolving mould. Their penetration model, shown in Figure 2-8, however, did not model the phase change. The model focused mainly on the heat conduction from the mould to the circulating powder pool sitting on the bottom of the mould. This was because the heat transfer from the mould to its cavity air had been neglected. In addition, they also presented extensive experimental and theoretical studies on the factors that influence the process conditions of rotational moulding. The studies included the relationships between heating rates and rates of degradation for rotationally moulded parts and the correlations between factors such as powder characteristics, melting-sintering mechanisms and process parameters to the process conditions.

Later in 1976, Throne [44] proposed a much simpler *static-bed-flow model*, which neglected the heat transfer to the circulating powder inside a revolving mould. In the model, the tumbling powder was assumed to be in static contact with the rotating mould surface at all times. This simple static model has better agreement with experimental data than the previous circulation model; despite the static model failing to describe

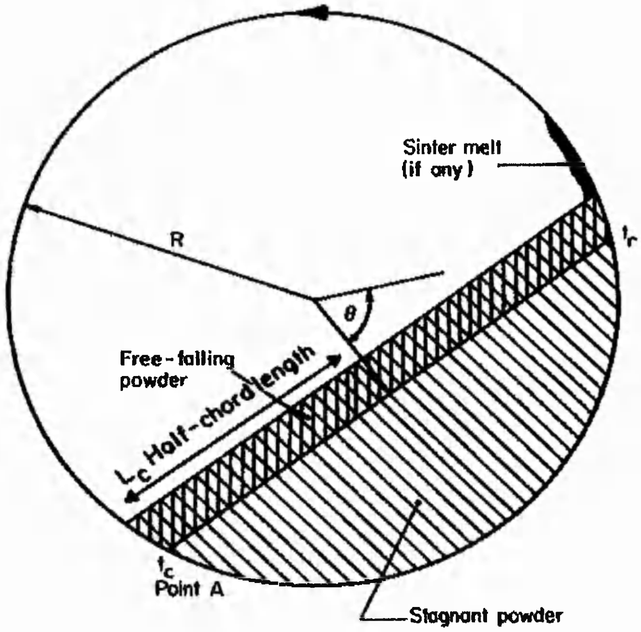

Figure 2-8: Idealized flow configuration for flow in a horizontal cylinder [9,66]

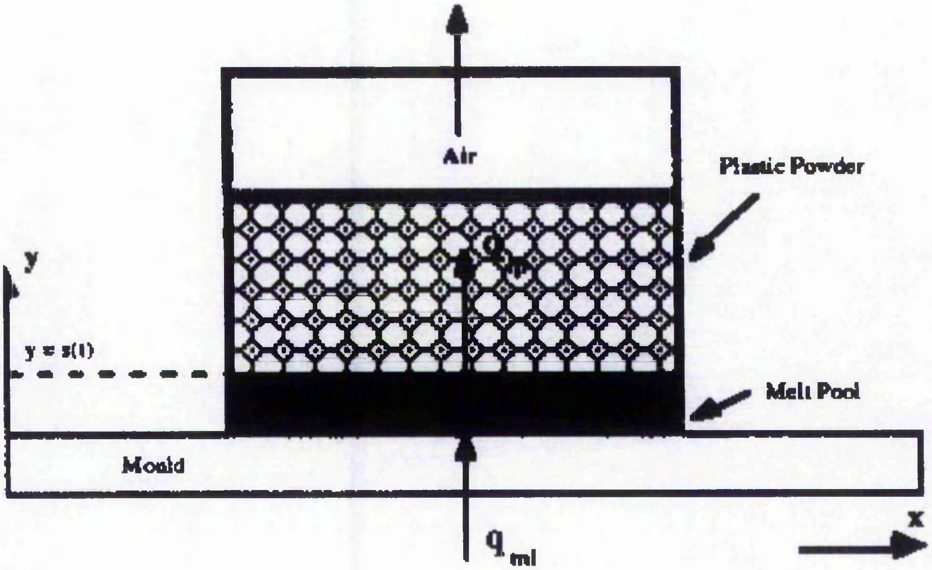

Figure 2-9: Model of the melting mechanism for plastic powder [45]

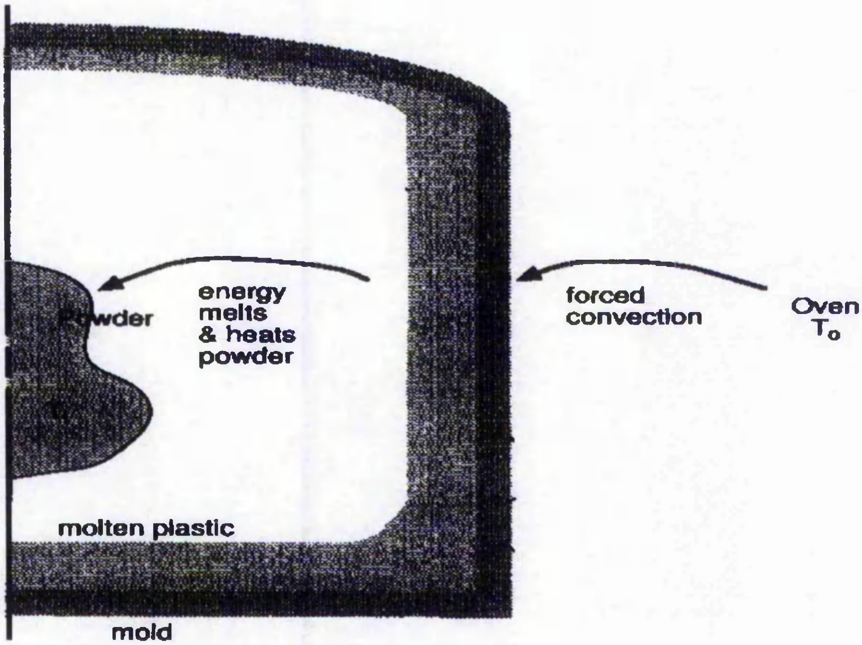

Figure 2-10: Model with well-mixed powder assumption [38]

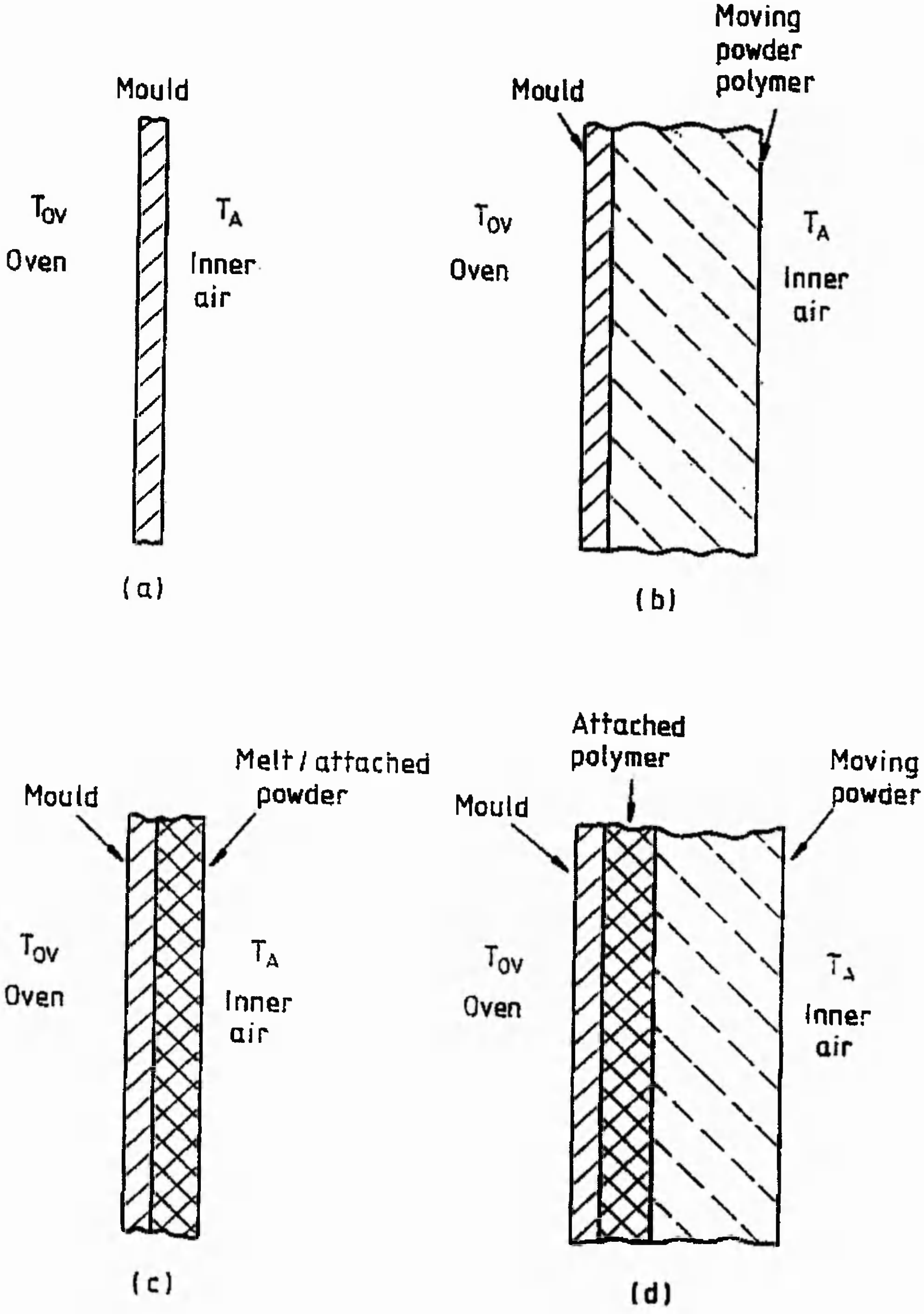

Figure 2-11: Superimposed heat transfer model [14]

the actual mixing of the powder inside the rotating mould. These probably can be explained by Tucker [47]. This states that accurate numerical solutions do not imply a correct model, and inaccurate numerical answers from the numerical method do not imply errors in the model. This is because the governing equations form a mathematical model via a numerical approach that will always remain an approximation of the real system. The better the model, the closer the model will approximate the real system.

In 1995, Bawisker and White [48] carried out an analytical study into the melting mechanism of the rotational moulding process to predict the melting front. In 1997, Attaran *et al.* [45] modelled the work, melting mechanism, numerically. In their model (Figure 2-9), the static powder bed was assumed to be of rectangular shape, with one side in contact with the mould surface and the other three sides exposed to the hot cavity air. However, this model was not useful for predicting the rotomoulding cycles.

The complex *Goodman circulation model* in Figure 2-8 [9] is briefly elaborated here to describe the modelling mechanism of the rotational moulding process. In the model, the mould was assumed to be very thin and to have a uniform temperature. As a result, the internal conductive resistance of the mould was neglected. The temperature of mould surface, obtained after the integration of its energy balance equation, rearrangement and further simplification, yields:

$$T_s = T_\infty(1-e^{-\beta t}) + T_0 e^{-\beta t} \approx T_\infty(1-e^{-\beta t}) \tag{2-7}$$

where the thermal diffusivity, $\alpha = k/\rho c$ and $\beta = h\alpha/Lk$. The k, ρ, c, h, and L are thermal conductivity, density, specific heat, heat transfer coefficient, and mould wall thickness, respectively. The thermal penetration thickness, δ, an artificial concept much like the fluid mechanical boundary layer thickness, was given as:

$$\delta =$$

$$\frac{2\sqrt{6\alpha_s}}{T_\infty(1-e^{-\beta t_2})+T^*}\left\{t_c[T_\infty^2+2T_\infty T^*+T^{*2}]+\left(\frac{2T_\infty^2}{\beta}+\frac{2T_\infty T^*}{\beta}\right)(e^{-\beta t_2}-e^{-\beta t_1})-\frac{T_\infty^2}{2\beta}(e^{-2\beta t_2}-e^{-2\beta t_1})\right\}^{1/2} \quad (2.8)$$

where T^* is the initial temperature difference between the mould surface and the powder re-contacting the mould surface. If the powder between $x=0$ and $x=x_1$ is above the melting temperature (T_m) at the point of release from the mould surface, this material is assumed to stick to the mould or itself. The average powder temperature was given as:

$$T_{av}=T_0(\delta-x_1)/(L_c-x_1)+[\delta T_s(t)/(L_c-x_1)](1-x_1/\delta)^4 \quad (2\text{-}9)$$

The thickness of the material that is at or above the T_m at the point of release was given as:

$$x_1=\delta\left\{1-[T_m/T_s(t)]^{1/3}\right\} \quad (2\text{-}10)$$

The time of free fall of powder between the release point and the re-contact point was

$$t_f=(2L_c/g\cos\beta')^{1/2} \quad (2\text{-}11)$$

where g is the gravitational constant, L_c is the half-chord length and β' is the dynamic angle of repose.

More recently, Gogos and co-workers [37,52,53] introduced another new theoretical heat transfer model for modelling the entire moulding cycle, in which a *well-mixed powder* was assumed. The assumption of a well-mixed powder pool was derived from Throne's conclusion [9], that further increased in the rotational speed of the mould (>10–20rpm) would not reduce the power-end-time. This generated a single equation for the mixing power pool, Equation 2-12, to represent the entire inner domain of a mould. The equation implies that the thermal capacitance of air is negligible. Gogos *et* *al.* further categorized the rotational moulding process into three distinct phases:

(i) *Phase 1*: This phase lasts until the inner mould surface reaches the isothermal melting temperature of the plastic.

(ii) *Phase 2*: The available plastic powder begins to deposit throughout the mould and this phase ends when all the powder has been deposited.

(iii) *Phase 3*: This phase begins as the cooling cycle starts and consists of three parts.

- Part 1: The moulded plastic layers across the part thickness undergo 'self-induced' further heating until some maximum temperature is attained.
- Part 2: The molten plastic solidifies.
- Part 3: Starts after the plastic begin to solidify, and ends when the solid plastic part is cooled down to the pre-assigned demoulding temperature.

Using the above theoretical model and well-mixed assumption, Gogos *et al.* [37] simplified the complex, multi-interacting heat transfer problem of the tumbling powder inside the rotating mould. Leaving only the heat balance relationship for the powder itself inside the mould cavity to be evaluated at *Phase 1* of the heating cycle, and it was given as:

$$m_p c_p \frac{dT_i}{dt} = \int_{S_i} h_i [T - T_i] dS_i \tag{2-12}$$

where m_p the mass of the plastic powder, c_p the specific heat of the plastic powder, T the temperature of mould, T_i the temperature of the well-mixed plastic powder, h_i the effective heat transfer coefficient of the energy transfer to the powder from the mould, and S_i inner surface of the mould. During *Phase 2* of the heating cycle, the heat balance equation for the powder becomes [38]:

$$m_p c_p \frac{dT_i}{dt} = \int_{S_p} h_i [T_m - T_i] dS_p + \int_{S_i} h_i [T - T_i] dS_i \tag{2-13}$$

and

$$m_p = m_o - \int_{V_p} \rho_p dV_p \tag{2-14}$$

where T_m the melting temperature of the plastic, S_p the are of the plastic inner surface, m_o the initial powder inside the mould, and V_p the volume of the sticking plastic layer. *Phase 2* ends when all of the available powder deposits on the mould surface, i.e. when $m_p = 0$. During *Phase 3* only the conventional energy equation is needed for modelling polymer.

Gogos *et al.* later introduced the *Arbitrary Lagrangian Eulerian* finite element models for a 1-D spherically symmetrical model [52] and a 2-D axisymmetric model (Figure 2-10) [38] for tracking the growth of the plastic layer at the isothermal phase change temperature. As a whole, Gogos *et al.* had derived a new theoretical model and also presented alternative 1-D and 2-D numerical approaches, such as finite difference and finite element techniques, to identify some key dimensionless groups affecting the process times [38,52,53,55].

A series of experimental and numerical studies and improvements on numerical modelling have recently been performed at Queen's University of Belfast (QUB) [11,14,22,24,42,43,45,49]. The first process controller (ROTOLOG, radio-based system) was developed by QUB for controlling the oven air temperature and for examining the temperature profiles of the internal air of the moulds [14]. The system helps to explore the plastic behaviour inside a closed mould and to verify numerical models. With the use of ROTOLOG, Nugent found that the control signal from the internal air could provide accurate control information of polymer properties and identify optimum heating and cooling times [14]. This was because the air profile exhibited a significant feature, which indicated the key process stages in rotational moulding. In addition, Nugent and Crawford [49] also discovered that the temperature profiles of rotational moulding are independent of mould shape.

In 1990, Nugent [14] developed a rotomoulding simulation program to examine the biaxial motion of a hollow mould containing a powder mass with a 1-D superimposed heat transfer mode, as shown in Figure 2-11. The simple model did not give satisfactory predictions partly because of the phase changes of the polymers had been neglected. Improvements were made in the Liang *et al.* [11,56] 1-D model to enable better prediction of the internal air temperature profile. In this model, the powder was initially assumed to be lying at the bottom of the mould, and it would then be in static contact with all parts of the inner surface of the mould at a pre-assigned plastic melting temperature. This approach allows the importance of the heat transfer between the inner mould surface and the internal air to be considered during the initial stages of heating. In 1993, Sun and Crawford [42,43] studied the efficiencies of 1-D internal heating and cooling effects with the ROHEAT program to improve the process times. The predicted results showed a considerable reduction in cycle time. In the ROHEAT model, the powder layers were treated as a packed bed (no mixing). Therefore, the approach did not consider the importance of the heat transfer between the inner mould surface and the internal air during the initial stages of the rotational moulding process.

According to Wright and Crawford [22], the distribution of plastic is controlled by two main factors - kinematics of the mould and heat transfer to the polymer. After some improvements and substantial simplifications (i.e. isothermal melting temperature and fluidization of the mixing pool), they developed a new combined thermal-kinematic model for the rotational moulding process. The kinematic model is to predict the polymer distribution inside a rotational mould. The thermal model for transient heat transfer was developed based on the energy equation in which the mass of the heated powder is continually changing. The thermal-kinematic model, ROTOSIM, is now commercially available and is used by processors worldwide. Wright and Crawford [22] also numerically found that the *radiation effect* makes a very minor contribution to the energy transfer of the rotational moulding, and consequently can be neglected.

Multidimensional models, which completely predict the temperature profile of the internal air, are still not possible. Wang [41] applied the *Alternating Direction Implicit method* (ADI) with a moving plastic boundary to trace the plastic growth in a 2-D static model. However, the predicted internal air temperature deviated substantially from the experimental result, as shown in Figure 2-12. The deviation was due to the fact that the internal air was heated up by the plastic layer rather than by the mould from the beginning of the simulation. This assumption did not reflect the real situation in rotational moulding. In addition, Wang [41] also applied the *coordinate transformation method* to determine the position and state of the mould with time. This technique was mainly for examining the best choice of rotating speeds. In Olson *et al.* [38], the growing plastic layer was tracked using the *Arbitrary Lagrangian Eulerian technique* at a distinct melting temperature. Owing to the assumption of a well-mixed powder (Figure 2-10), the approach had to initially neglect the thermal capacitance of the internal air compared to the thermal capacitance of the powder mass inside the revolving mould. As depicted in Figure 2-13, the Gogos *et al.* model led to a 'poor' prediction for the internal air temperature in *Phase 1* of the heating cycle [37]; for

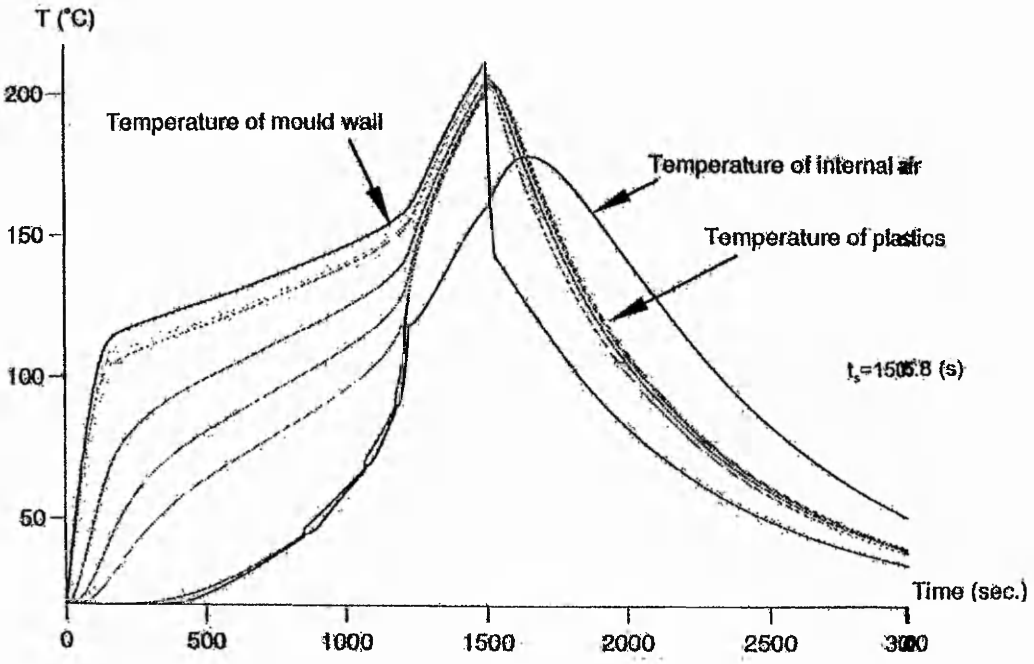

Figure 2-12: Example of predicted temperatures using moving plastic boundary [41]

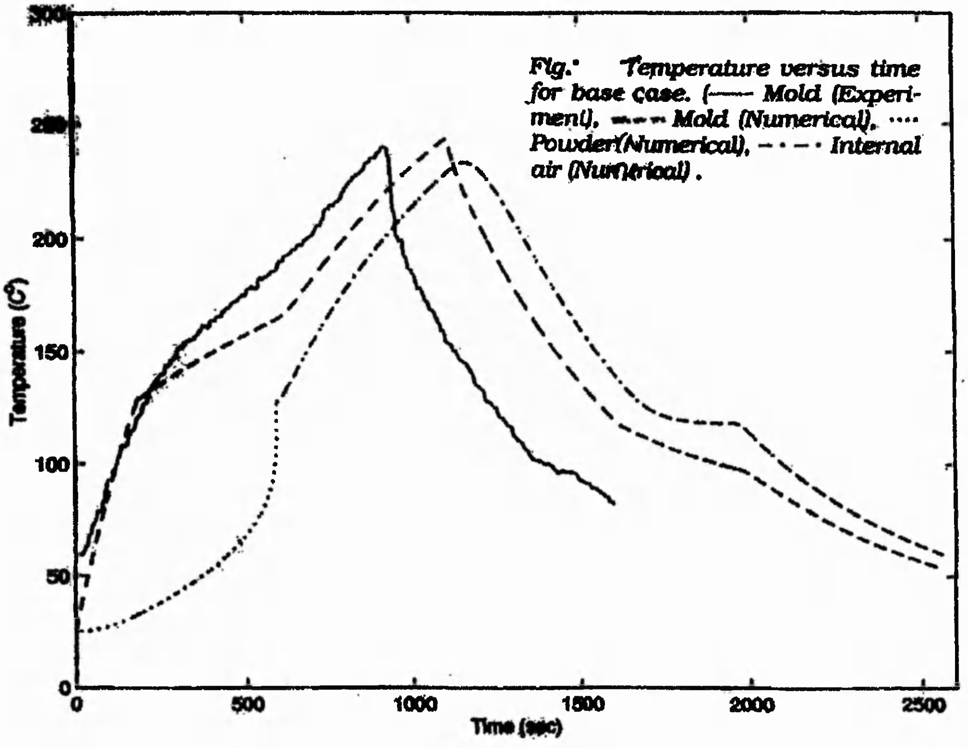

Figure 2-13: Example of predicted temperatures using well-mixed assumption [37]

example, an equal temperature was assumed for the internal air and the powder pool.

The initial ROTOLOG controller provides a detailed insight into the various stages of the rotational moulding cycle. However, the data collection was difficult owing to the rotational motion of the mould and the high oven temperatures. The latter limited the ROTOLOG's operation time, as the sensor must be removed periodically from operation to be cooled [14]. In view of these disadvantages, various potential control methods [50,51], such as infrared thermometry and dynamic machine control systems, have been studied and developed. Nugent [50] introduced infrared thermometry or IRT for measuring temperature data directly from the oven and mould surface. It is indeed a non-contact sensor. The IRT's temperature showed some close correlations with the direct experimental measurement. Unfortunately, it was unable to identify the key process stages of the rotational moulding. Using the *neural network method*, Fara *et al.* [51] presented a dynamic model to provide a control strategy for rotational moulding machines. This empirical dynamic model (deterministic type) allowed the oven temperature and the internal air temperature to be identified.

2.13 Thermal Properties of Plastics [13,20,58,59]

The thermal modelling of rotational moulding does require relatively accurate inputs of thermal properties of materials and some understanding on their behaviour. This is because the thermal properties such as thermal conductivity, thermal diffusivity, density and specific heat are influential temperature dependent parameters.

2.13.1 Thermal Conductivity

The thermal conductivity of plastics is about 300–1000 times lower than those of metals. For a pure plastics, the thermal conductivity, k, varies over a range of 0.15–0.50 W/mK. The thermal conductivities of semi-crystalline polymer are generally higher than those of amorphous polymers. Temperature has only a very little or almost negligible effect on the thermal conductivity of amorphous thermoplastics. In contrast, the thermal conductivity of semi-crystalline thermoplastics drops with increasing temperature up to the melting point. Above that point, the thermal conductivity remains relatively constant for polymer in their molten state. For an isotropic material, k is a scalar quantity. When a material is non-isotropic, k then becomes the following tensorial quantity [59]:

$$k = \begin{bmatrix} k_{11} & k_{12} & k_{13} \\ k_{21} & k_{22} & k_{23} \\ k_{31} & k_{32} & k_{33} \end{bmatrix} \tag{2-15}$$

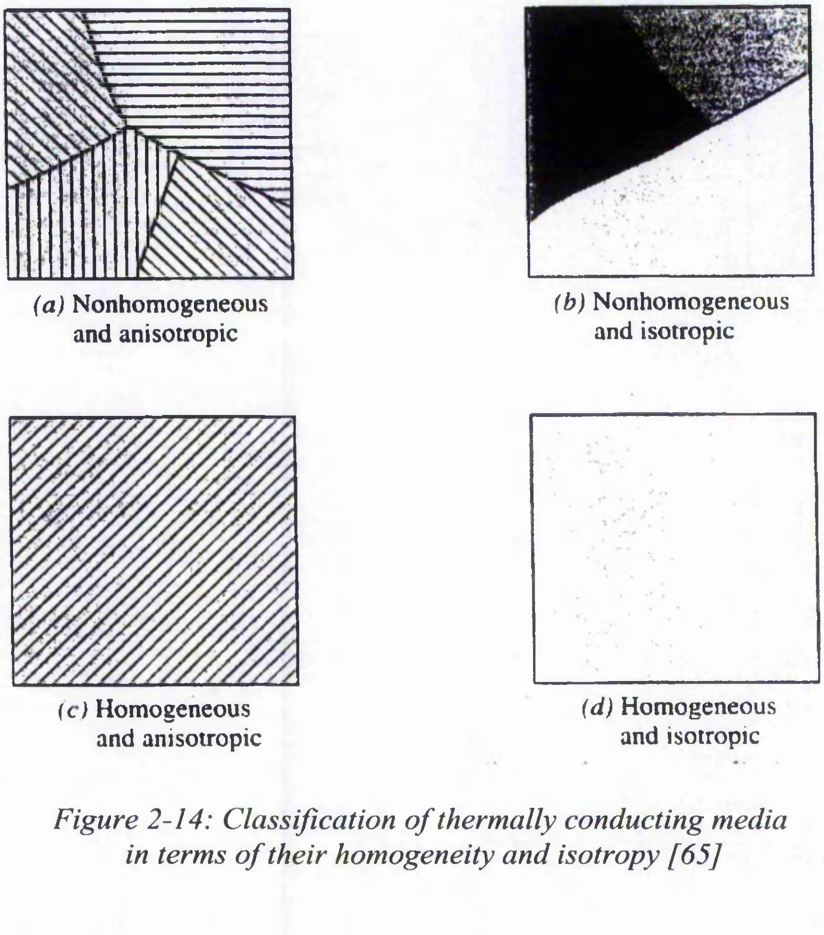
(a) Nonhomogeneous and anisotropic

(b) Nonhomogeneous and isotropic

(c) Homogeneous and anisotropic

(d) Homogeneous and isotropic

Figure 2-14: Classification of thermally conducting media in terms of their homogeneity and isotropy [65]

Figures 2-14 (a)–(d) illustrates the classifications of homogeneity and isotropy of thermally conducting media.

2.13.2 Density

The density of a substance is its weight or mass for a given volume. The density of a polymer is a function of temperature, pressure and cooling rate. Temperature is the most influential factor in density. The density of unfilled plastics is in a range of 0.9 to 2.3 g/cm^3. Generally, the *effective density* of a powder bed is an important parameter. It simplifies the treatment of heat transfer analysis in the two-phase powder system by implicitly taking into accounts the void fraction of the powder bed.

2.13.3 Specific Heat

Specific heat is the quantity of heat needed to increase the temperature of a unit mass of a body by a unit of temperature. It can be measured either at constant volume, c_V, or at constant pressure, c_P. Typically, the specific heat of amorphous thermoplastics increases almost linearly with temperature below and above the glass transition temperature, T_g, and with a step-like change at T_g. For pure crystalline polymers, mathematically, a very distinct maximum occurs and approaches infinity at the melting temperature, T_m, instead of the step-like change at T_g.

Crystalline polymers in general are all semi-crystalline. This is because they are impossible to form in completely crystalline phases as they all have amorphous parts. Therefore, the specific heat exhibits a non-isothermal melting peak in the temperature range of T_g to T_m. The higher the degree of crystallinity, the higher the specific heat.

The thermodynamic states of melting plastic for amorphous and semi-crystalline polymers are generally located at $T > T_g$ and $T > T_m$, respectively.

2.14 Mechanism of Heat Transfer

In any thermal analysis, conduction, convection (advection) and radiation are the three common heat transfer mechanisms. Conduction is the one that occurs most commonly in polymer processing. In a solid material, for example, heat is usually transferred by conduction. The mechanism of heat conduction is due to both vibration of atomic lattice and the motion of free electrons. The latter is the more powerful effect. Since the non-metals such as polymers have few free electrons, therefore, they are generally poor heat conductors [13,60].

Convective heat transfer is the transfer of heat from one point to another by a net fluid motion. Convection heat transfer only occurs in fluids. When a moving fluid encounters a solid surface, heat is convected either from it or to it, depending on the sign of the surface-to-fluid temperature difference. Principally, the convection process consists of natural and forced convections. For *natural convection*, there is no mechanism to force the flow. It occurs in the presence of a temperature difference that creates density variations to cause the movement of the fluid. *Forced convection* exists when the fluid is forced to move by some external means such as a fan or a pump.

The distinction between free and forced convection is the dependence of the *heat transfer coefficient* on the fluid-to-medium interface. In practice, the exact value of the convective heat transfer is difficult to measure as it varies with time and depends upon many factors. Generally speaking, a representative range of the values of the heat transfer coefficient for air is 6–30 W/m^2K for natural convection, and 10–200 W/m^2K for forced convection [60]. Radiation is the less common heat transfer mode in polymer powder processing especially in the rotational moulding process [22]. For this type of heat transfer mechanism, the heat is transferred in the form of electromagnetic waves [13].

2.14.1 Heat Conduction Equation: Conductive heat transfer

A general universal heat conduction equation can be written as Equation (2-16) [13]. The derivations of the conduction equations (2nd order partial differential equations) for different coordinate systems will not, however, be addressed here as they can be found elsewhere [60–63].

$$\begin{array}{ccccc}\text{Net of heat conduction} & & \text{Rate of heat} & & \text{Rate of sensible heat} \\ \text{inside control volume} & + & \text{generation inside} & = & \text{change (storage/release)} \\ & & \text{control volume} & & \text{inside control volume}\end{array}$$

$$\frac{\partial}{\partial l_1}\left(k\frac{\partial T}{\partial l_1}\right)+k\frac{\lambda}{l_1}\left(\frac{\partial T}{\partial l_1}\right)+\left(\frac{\delta}{l_1^2}+\gamma\right)\left[\frac{\partial}{\partial l_2}\left(k\frac{\partial T}{\partial l_2}\right)\right]+\dot{q}=\rho c\left(\frac{\partial T}{\partial t}\right) \qquad (2\text{-}16)$$

where T is the temperature, k is the thermal conductivity, ρ is the density, c is the specific heat, and $\dot{q}$ is the heat generation term. In Equation (2-16), three parameters are introduced; λ is defined as the shape parameter, which takes the value 0, 1, or 2 for planar, cylinder (annular) or spherical coordinate systems. The combinations of different λ, γ, and δ describe the above energy equation as:

(i) $\delta = 0$, $\gamma = 1$, $\lambda = 1$ for the 2-D process in cylindrical coordinates (l_1 for the r-coordinate, l_2 for the z-coordinate);

(ii) $\delta = 0$, $\gamma = 1$, $\lambda = 0$ for the 2-D process in rectangular coordinates (l_1 for the x or z coordinate, l_2 for the y-coordinate);

(iii) $\delta = 1$, $\gamma = 0$, $\lambda = 1$ for the 2-D process in cylindrical coordinates (l_1 for the r-coordinate, l_2 for the ϕ-coordinate);

(iv) $\delta = 0$, $\gamma = 0$, $\lambda = 0$ for the 1-D process in rectangular coordinates (l_1 for the x, y, or z coordinate);

(v) $\delta = 0$, $\gamma = 0$, $\lambda = 1$ for the 1-D process in cylindrical coordinates (l_1 for the r coordinate);

(vi) $\delta = 0$, $\gamma = 0$, $\lambda = 2$ for the 1-D process in spherical coordinates (l_1 for the r coordinate).

The term $\dot{q}$ of Equation (2-16) may represent one or more of the heat sources below:

(i) Heat generation through phase change, i.e. melting or solidification and crystallization of molten polymer.

(ii) Heat generation through heating sources, i.e. internal heating and cooling and other methods of enhancement if heat transfer.

(iii) Heat generation through chemical reaction, i.e. endothermic (negative term) or exothermic (positive term) reactions.

2.14.2 Boundary Conditions [60,65]

There are three types of linear boundary condition that are frequently used with the heat conduction equation above; prescribed temperature, prescribed heat flux and convective boundary condition. A linear boundary condition generally refers to the boundary condition, which is linear in relation to temperature.

(i) Prescribed temperature:

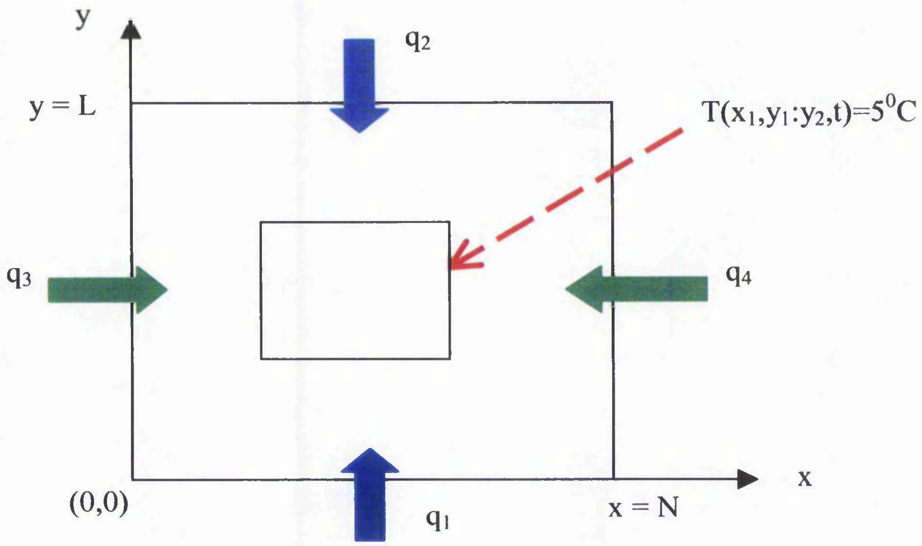

Figure 2-15: Boundary conditions of a rectangular model in rectangular coordinates

The temperature is defined on the boundary explicitly. As depicted in Figure 2-15, for example, $T(x_1, y_1 : y_2, t) = 5^0 C$.

(ii) Prescribed heat flux:

The temperature is implicitly defined through an explicit statement of the heat flux, for example,

$$q_1 = -k \frac{dT(0:N, y, t)}{dy}\bigg|_{y=0} = 30 \quad W/m^2$$

$$q_2 = -k \frac{dT(0:N, y, t)}{dy}\bigg|_{y=L} = -10 \quad W/m^2$$

The negative sign of $\frac{dT}{dy}$ is a consequence of the fact that heat is transferred in the direction of decreasing temperature. According to Figure 2-15, the heat conductive rate equation (*Fourier's Law*) $q_1 > 0$ means that the heat flow is in positive y-direction, and vice-versa for the case of $q_2 < 0$.

(iii) Convective boundary condition (Figure 2-15):

The overall heat transfer rate between the fluid and its contact surface is governing by *Newton's law of cooling*. By specifying the temperature gradient at the surface in terms of external heat transfer coefficients, h_3 and h_4, the unknown surface temperatures, T_3 and T_4, and the fluid reference temperature, T_∞, the heat fluxes are:

- $$q_3 = -k \left. \frac{dT(x,0:L,t)}{dx} \right|_{x=0} = h_3(T_3 - T_\infty) \qquad (2\text{-}17)$$

- $$q_4 = -k \left. \frac{dT(x,0:L,t)}{dx} \right|_{x=L} = h_4(T_4 - T_\infty) \qquad (2\text{-}18)$$

The convective heat fluxes in Equation (2-17) and Equation (2-18) are presumed to be positive if heat is transferred from the contact surface of the fluid and negative if heat is transferred to the surface. However, there is nothing to preclude *Newton's law of cooling* being expressed as [65]:

- $$q_3 = -k \left. \frac{dT(x,0:L,t)}{dx} \right|_{x=0} = h_3(T_\infty - T_3) \qquad (2\text{-}19)$$

- $$q_4 = -k \left. \frac{dT(x,0:L,t)}{dx} \right|_{x=L} = h_4(T_\infty - T_4) \qquad (2\text{-}20)$$

In this case, the heat transfer is positive when heat is transferred to the surface.

2.15 Research Objectives

In the rotational moulding industry, the traditional, commonly used trial-and-error methods for determining the heating and cooling cycles are inefficient, time-consuming and expensive. In this research, numerical studies on the rotational moulding process are carried out to provide better control and optimisation on the process as well as to thoroughly understand some key problems and phenomena of the process. To develop the first in-house software for the modelling of the rotational moulding process after considering:

1. The possible limitations or restrictions of available commercial software in handling the thermal complexities of the air inside a rotating mould during the heating cycle.
2. The methodology for overcoming the numerical difficulties of multi-dimensional thermal models of the rotational moulding.

The objectives of the numerical modelling in this research include:

1. To seek and devise a new two-dimensional model that:
    (i) Provides a simple numerical methodology for modelling.
    (ii) Deliver an alternative perspective of rotational moulding model.
2. To propose an appropriate, efficient and easily incorporated phase-change algorithm for the numerical treatment of phase change while maintaining a reasonable level of accuracy.
3. To carry out numerical studies on warpage under different degrees of solidification and process conditions, which are experimentally difficult to measure.
4. To numerically study the sensitivity of the process parameters on the cycle times via dimensionless groups.

CHAPTER 3

FINITE ELEMENT METHOD AND MODELLING OF PHASE CHANGE

3.1 Finite Element Method (FEM)

In thermal engineering analysis and design, heat transfer with energy conservation is commonly represented by the use of thermal circuit models, analytical or numerical methods in solving the energy conservation equation. In addition, the analysis of heat transfer can also be based on semi-empirical or empirical (based on experimental correlations) relations. This semi-empiricism allows for engineering analysis of some very complex and yet often encountered systems [62]. It may be too involved and expensive to study the optimisation of all the thermal parameters in the rotational moulding process. The present research will, however, only be devoted to a numerical study.

Various numerical techniques such as finite difference, finite volume, finite element and boundary element methods can be used for the purpose of modelling. Since the 1980's the utilization of the finite element method (FEM) in engineering applications has increased significantly. This is because of its flexibility in dealing with complex geometries and general problems, and its ease in implementing boundary conditions [71]. For general practical analysis, the use of conventional FEM appears to be the most promising [73]. In addition, the literature review of the novel *coincident node technique* of FEM '*family*' [67–69] and of the *lump-parameter systems* (discrete numerical systems) [70] has shown the feasibility of the techniques to couple with the conventional finite element method in describing the new proposed model for the rotational moulding. As a result, the FEM is adopted for this research. In fact, the choice of numerical techniques depends on the context of a problem as well as the technical expertise of an investigator. Thus, the merits of various numerical methods will not be dwelled on. Some background theories of lumped-parameter system and FEM will be described below.

In brief, the essence of a lumped-parameter system (discrete numerical system) is that the state of the system can be described with adequate precision by the magnitudes of a finite number of state variables. The approach is characterized by a set of algebraic equations involving a finite number of unknowns or degree of freedom [70,74]. In the analysis of a discrete system, the actual system response can be directly expressed by the solution of a finite number of state variables [70].

The purpose of FEM is to provide piecewise approximation to the differential equations numerically, which it is not possible to construct by any analytic solution. It is one of the discretization procedures used to generate systems of algebraic equations [74,77]. In the FEM, a given computational domain is actually subdivided into a number of finite elements that may vary in size and shape. The elements are interconnected by a discrete number of nodes. The general element types (i.e. triangular or rectangular) and families (i.e. serendipity or Lagrange) are described in details elsewhere [70,74,80,87]. In order to employ finite element discretization, a physical problem should first be characterized by a *variational (weak) principle* [74,80]. In the case of solid mechanics, for example, the functional could be the total potential energy of the mechanical system. This gives an integral formulation directly from the stationary property of the functional. Thus the *variation principle* is found useful since the total potential system is easier to formulate [74].

In most finite element approaches, however, the transformation of a differential formulation into an equivalent variational formulation is often performed by the *weighted residual methods* - alternative procedures. By this means, any set of partial differential equations is transformed into an integral expression. The transformation depends on the choice of weighting function, decided by the type of weighted residual methods [74]. A more distinct comparison of these two approaches is illustrated in Figure 3-1.

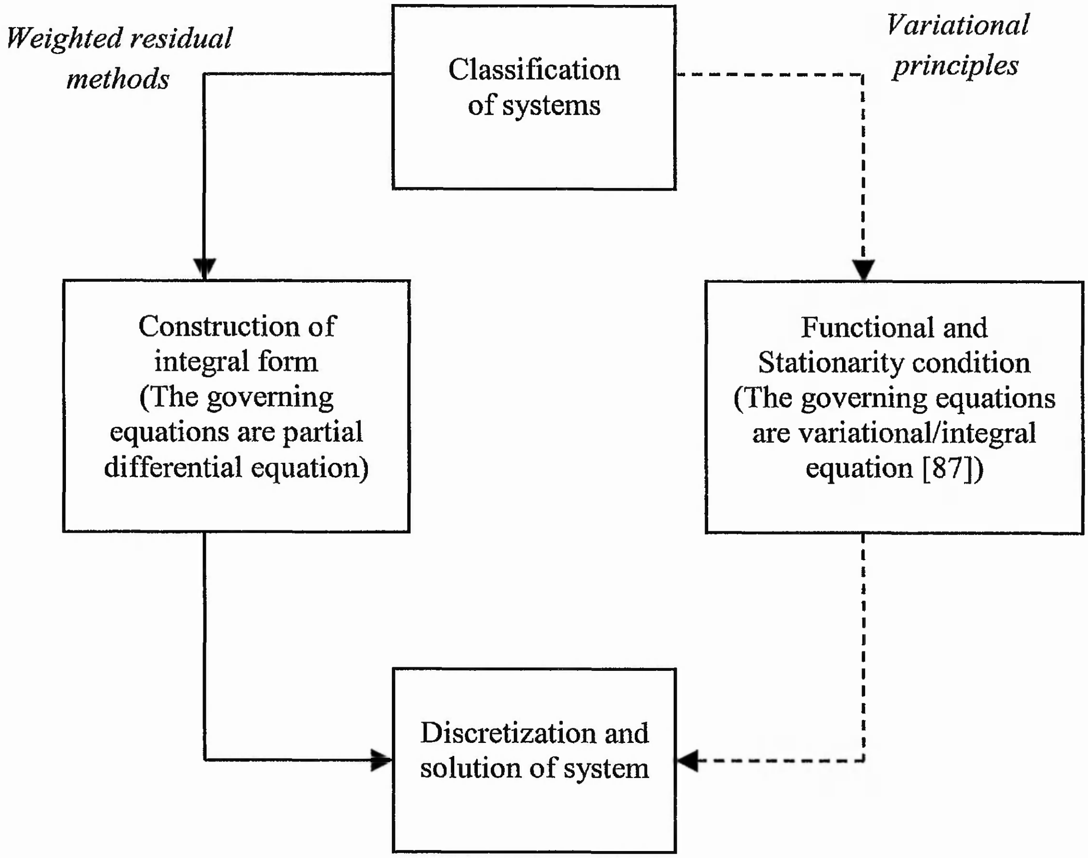

Figure 3-1: Comparison of weighted residual methods and variational principles [74,87]

3.1.1 Spatial and Temporal Discretizations

For a discretized *initial-boundary value problem*, such as Equation (3-1), a complete finite element discretization commonly consists of two steps [71,72,79,80,87]:

(i) Spatial discretization of a partial differential equation or PDE (continuous system), in which the weak integral form of the equation is determined using the weighted-residual procedures. From the widely used *weighted-residual methods* [80] (i.e. the Galerkin method, Least squares method, Subdomain method, Collocation method, and Petrov-Galerkin method), the Galerkin finite element method is adopted here. The method appears to be the most generally useful and easily understandable optimising criterion for finite element work in both teaching and practical applications [87].

(ii) Temporal discretization/approximation of an ordinary differential equation (ODE): The ODE is obtained from the previous spatial discretization. However, it can be further simplified to represent a physical system by a set of algebraic equations of a discrete system via a finite difference technique or other technique. The commonly used time-stepping schemes for the discretization are the two-time-level scheme (i.e. $\theta - method$) [87] and the three-time-level scheme (i.e. Dupont II and Lee schemes).

3.1.2 Galerkin Finite Element Method

A 2-D transient heat conduction model of an initial-boundary value problem is demonstrated here for the purpose of revealing the weak integral form of PDE by the Galerkin finite element method. However, there is no consideration of any internal heat generation involved.

$$\rho c\frac{\partial T(x,y,t)}{\partial t}=\nabla(k\nabla T(x,y,t)) \qquad \text{on}\,\Omega \qquad (3\text{-}1)$$

The equation is solved with the appropriate Dirichlet (Essential) boundary condition, Neuman (Natural) boundary condition and initial condition, given as [82]:

$$T(\partial\Gamma_T,t)=\hat{T} \qquad \text{on } \partial\Gamma_T \qquad (3\text{-}2)$$

$$-k\frac{\partial T(\partial\Gamma_q,t)}{\partial n}=-k\nabla T\cdot\hat{n}=q_a+q_c+q_r \qquad \text{on } \partial\Gamma_q \qquad (3\text{-}3)$$

$$T(x,y,t)=T_0(x,y,0) \qquad \text{on } \Omega \qquad (3\text{-}4)$$

Here, q_a, q_c, and q_r are the applied flux, the convective and the radioactive flux, respectively. T, k, ρ, c, and $\hat{n}$ are the temperature, thermal conductivity, density, specific heat, and the normal vector to the boundary surface, respectively.

In FEM, the variable, $T(x,y,t)$, is approximated within each element by a linear combination of interpolation/shape functions, N. Assuming that time dependence can be separated from the partial variation (typical element trial solution), hence:

$$T(x,y,t)\cong\sum_{j=1}^{n}T_j(t)N_j(x,y)=\tilde{T}(x,y,t;N) \qquad (3\text{-}5)$$

where the n is the total elemental degree of freedom for a variable. In this case, it is also equilibrium to the total number of elemental nodes. By introducing an approximate trial solution for Equation (3-5) into Equation (3-1), and by defining a *residual* for the equation (error of an equation), $\hat{R}(x,y,t;N)$, this gives a nonzero function of Equation (3-6) as:

$$\hat{R}(x,y,t;N)=\rho c\frac{\partial\tilde{T}}{\partial t}-\nabla(k\nabla\tilde{T})\neq 0 \qquad (3\text{-}6)$$

Applying the Galerkin weighted residual procedure, ψ, to Equation (3-6) will allow the selection of the weighting function $\psi = N$. This leads to the following integral identity:

$$\int_\Omega \psi_i \left\{\hat{R}(x,y,t;N)\right\} \partial\Omega = 0 \tag{3-7}$$

where the subscript $i = 1,2,...,w$. The w is the number of arbitrary shape function.

Equation (3-8), *integration by parts* (first form of Green's theorem) [76], is used to eliminate the higher-order derivatives in Equation (3-7).

$$\int_\Omega \psi_i \nabla^2 T d\Omega = -\int_\Omega \nabla T \nabla \psi_i d\Omega + \int_\Gamma \psi_i \nabla T \cdot \hat{n}\, d\Gamma \tag{3-8}$$

This transforms Equation (3-7) to a weak integral form *cf.* Equation (3-9), which results in derivatives of the weighting function.

$$\int_\Omega \psi_i \rho c \frac{\partial \tilde{T}}{\partial t} \partial\Omega + \int_\Omega k \nabla \tilde{T} \nabla \psi_i \partial\Omega - \int_\Gamma \psi_i \nabla T \cdot \hat{n}\, d\Gamma = 0 \tag{3-9}$$

where the boundary terms can be found in Equations (3-2) and (3-3). Further simplification and rearrangement of Equation (3-9) gives rise to a system of ordinary differential equation (ODE) as follows:

$$[C]\left\{\dot{T}\right\} + [K]\{T\} = \{F\} \tag{3-10}$$

where $[C]$ and $[K]$ are the typical capacitance and conductivity/stiffness matrices, and the $\{F\}$ is the force/load vector dependent on the boundary conditions involved. Since the details of FEM can be found elsewhere [74,80,82], no further steps will be described. In addition, the practical aspects of the FEM and formulation of Equation (3-10) will be described for the present situation in this thesis below (Chapter 5).

3.2 Mathematical Expressions for Modelling of Phase Change

Before a polymer powder is transformed into a final part, the semi-crystalline powder will undergo phase transformation during the heating and cooling cycles of the rotational moulding process. Therefore, it is important to accurately account for the latent heat released or absorbed in order to determine the predicted internal air profile, i.e.:

(i) Indicating an accurate heating and cooling cycle times

(ii) Symbolizing the six major stages of the rotational moulding process (powder heating, melting, further heating, liquid cooling, crystallizing and further solidifying stages)

Phase change phenomena are commonly categorized into two major groups -isothermal (distinct) and non-isothermal (binary) [71]. An isothermal phase change composes of two distinct solid and liquid phases. The phase change is indeed described by the thermal-physical properties of the liquid and solid phases and a continuous moving front. On the other hand, a non-isothermal phase change is a combination of solid, mushy and liquid phases. A mushy zone resembles a porous medium containing the partly solid and partly liquid materials that exists between the solid and liquid temperatures.

In casting research, detailed numerical algorithms and studies of phase change problems have been widely evaluated [67,71,75]. Such numerical studies, however, still have not generally been applied to the rotational moulding process. Although the incorporation of a phase change into a non-linear transient energy equation is not novel, it still presents problems in the terms of numerical implementation. The level of difficulty depends on the level of accuracy and the amount of information required (i.e. location of solidification front). Since finite element modelling is considered, herein the following literature review of numerical techniques for phase changes is more directly related to the finite element formulation. Of course, some of the elaborations are generally accepted and broadly applicable in other numerical methods.

Numerical techniques for phase change [71,76] can be divided into front tracking (classical Stefen's problem) and fixed-domain/fixed-mesh methods (weak formulation). The numerical implementation of phase change algorithm for the former technique is generally more difficult than the latter. In the classical Stefen's method, the interface of the phase change front is explicitly tracked by a moving boundary via some special boundary techniques, such as by adjusting the spatial discetization mesh (moving-mesh method) or by defining some suitable co-ordinate transformation (front-fixing method) [83]. Thus the front-tracking methods are also computationally expensive. In addition, they are more suitable for the 1-D isothermal problems of phase change rather than for the non-isothermal or multi-dimensional ones. As a whole, the front tracking techniques would involve:

(i) Grid deformation or alteration

(ii) Prediction of the location of the phase front

(iii) Transformation of variables or co-ordinates

(iv) Introduction of special algorithms near the phase change interface

3.2.1 Front-Tracking Techniques for Phase Changes

In the moving finite element methods, a solution to the phase change problem is obtained by solving two energy equations, *cf.* Equation (3-11), which represent the energy balance of liquid and solid phases, respectively.

$$\rho c\left(\frac{\partial T}{\partial t}\right) - \nabla\cdot(k\nabla T) = \dot{q} \qquad \text{on } \Omega \qquad (3\text{-}11)$$

To do this, the energy equations are compulsorily coupled by the boundary conditions of Equations (3-12) and (3-13). This is because the moving front must satisfy both boundary conditions.

$$T_s = T_l = T_f \qquad \text{on } x = s(t) \qquad (3\text{-}12)$$

$$k_s\left(\frac{\partial T}{\partial n}\right)\bigg|_{x=s(t)} + k_l\left(\frac{\partial T}{\partial n}\right)\bigg|_{x=s(t)} = \rho_s L\left(\frac{\partial s}{\partial t}\right) \qquad (3\text{-}13)$$

where convection is neglected. The subscripts s and l represent the solid and liquid phases, respectively. The $\dot{q}$ is the rate of internal heat generation, L is the latent heat, $s(t)$ is the position of the moving front, and T_f is the isothermal phase change temperature.

3.2.2 Fixed-Domain Techniques for Phase Changes

In fixed-domain techniques, the initial spatial discretization mesh remains fixed throughout the numerical calculation. A latent heat evolution is *implicitly* accounted for during the phase change of a material. Thus a single energy equation is sufficient to describe the latent heat evolution, which can be expressed in the energy equation either as a volumetric enthalpy, H, an apparent heat capacity, $\frac{\partial H}{\partial T}(= C_{app})$, an effective heat capacity, C_{eff}, or a heat source term, Q. This implies that only an energy equation is sufficient to represent the whole liquid and solid domains. During the computations for a phase change effect, the front of a latent heat transformation could be located at a node or alternatively pass through an element or control volume. The latter divides the control volume of an element into regions of two major phases - solid and liquid, as delineated in Figure 5-2 [81].

The attractive features of the fixed-domain techniques for phase change problems include [83]:

(i) Ease of implementation in existing program packages.

(ii) Ease of convergence to the weak solution of the differential equation.

(iii) Simple (implicit) representation of latent heat released at the interface, the position of which need not be specified a priori.

(iv) Capability of tackling phase change problems, which involve complicated-shaped models or multidimensional freezing fronts.

Therefore, in view of the above advantages, the non-isothermal phase change encountered in semi-crystalline polymer and the dynamic nature of the rotational moulding process, the fixed-domain techniques are chosen for the present application. Various fixed-mesh techniques have been studied in detail before choosing the most suitable phase change algorithm for the present finite element code development.

3.2.3 Categories of Fixed-Domain Techniques

In fixed-domain finite element techniques, the expression for the phase change in the energy equation can be generally categorized into three major groups [71–73,78,79,81,83–86]:

(i) Enthalpy-based approach,

(ii) Temperature-based approach,

(iii) Source-based approach.

3.2.3.1 Enthalpy-based Approach [75,76,78,81,84]

The volumetric enthalpy, H, is the key state variable in the enthalpy-based approach although Equation (3-14) seems to have two dependent variables, H and T. In fact, the volumetric enthalpies are first evaluated, and the temperatures at time level $n+1$ may then be directly determined from the enthalpy versus temperature relationship. However, this key variable does not appear very useful in the present studies.

$$\frac{\partial H}{\partial t} = \nabla(k\nabla T) \qquad \text{in } \Omega \tag{3-14}$$

3.2.3.2 Temperature-based Approach

The temperature-based approach is the most common numerical technique for the analysis of phase change problems. This approach can have computational difficulties when there is an abrupt change in the heat capacity, especially when the phase change occurs at a distinct temperature, or over a small temperature range (Dirac-δ-type behaviour) [75]. In this approach, the thermal properties of a polymer can either be represented by a set of discrete data or a set of continuous analytical equations. The following *capacitance methods* (i.e. apparent heat capacity method and effective heat capacity method) are the most common methods used to account for the latent heat of phase change in the temperature-based approach.

(i) Apparent Heat Capacity Method [71,75,76,88]:

This method requires the consideration of any phase change at each node and the evaluation of the heat capacity from the enthalpy gradients $\frac{\partial H}{\partial T}$ $\left(= C_{app}\right)$. The method can be use to evaluate the isothermal and non-isothermal problems for a phase change. For an isothermal problem, however, the C_{app} experiences an abrupt change at the phase change temperature, T_l (Figure 3-2). Therefore, an artificial Dirac-δ-type temperature interval is often required at T_l (i.e. Figure 3-3). This aims to avoid/minimize any node jumping across the phase change

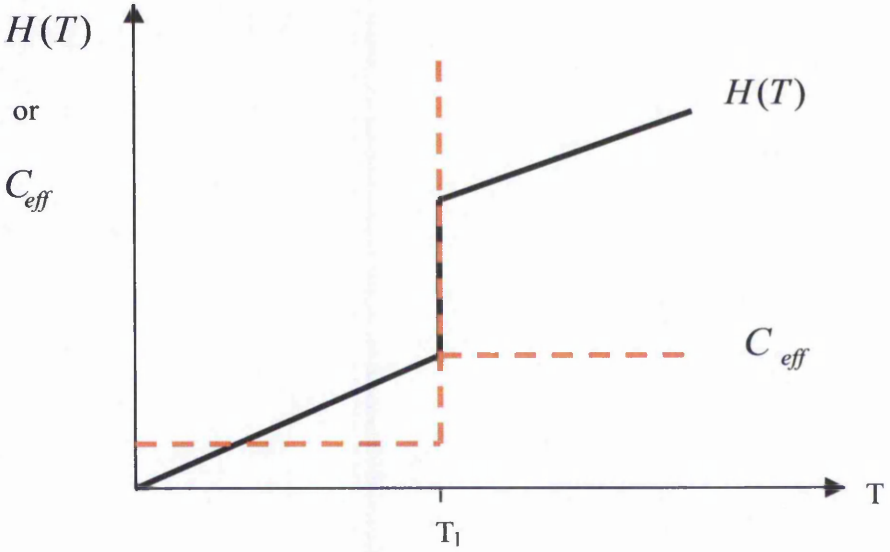

Figure 3-2: Variations of $H(T)$ and C_{eff} with temperature for isothermal phase change [72,75]

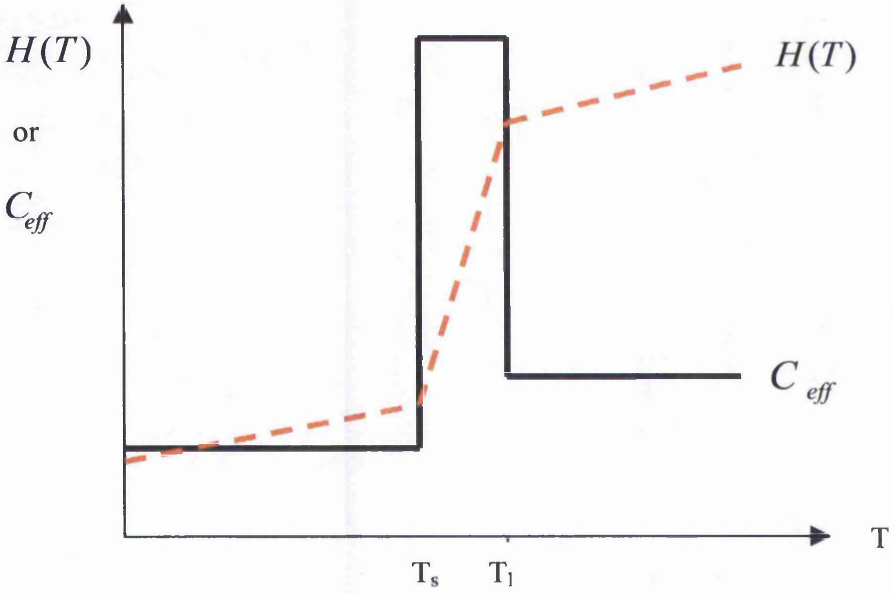

Figure 3-3: Variations of $H(T)$ and C_{eff} with temperature for non-isothermal phase change [72,75]

region, which causes the latent heat not to be taken into account.

The direct evaluation of C_{app} is often restricted by the size of the time step and the occurrence of any oscillation produced, especially at the Dirac-δ-type temperature interval [71,75]. The *averaging techniques* of Equations (3-22), (3-23) or (3-24) are usually adopted to avoid any possibility of missing peak values of the apparent heat capacity, C_{app}, in Equation (3-15). This is because these averaging techniques can help to preserve a correct heat balance [88].

$$\frac{\partial H}{\partial T}\frac{\partial T}{\partial t} = \nabla(k\nabla T) \qquad \text{in } \Omega \qquad (3\text{-}15)$$

As shown in Figure 3-3, the volumetric enthalpy, H, can be represented by smooth functions of temperature when the Dirac-δ-type temperature interval is imposed at the phase change region. This continuous expression allows the interpolation of the H in Equation (3-15) from the nodal values, which can be expressed as:

$$H = N_j(x,y)H_j(t) \qquad (3\text{-}16)$$

where N_j are the interpolation/shape functions within an element.

(ii) Effective Heat Capacity Method [75,76]:

This is an improved version of the apparent heat capacity method, in which the apparent heat capacity, C_{app}, is integrated over a control volume of an element. Typically, a linear variation of temperature is assumed between two computational nodes [76]. The solution from this method is relatively independent of the temperature interval at phase change (i.e. mushy zone), hence, the assumption of a large fictitious phase change temperature for a polymer is not required. This method is not straightforward to implement. In addition, an extra cost arises due to the numerical integration of the C_{app} over the elemental control volume, V_e, making the method computationally expensive [75,76].

$$C_{eff}^{e} = \frac{\int_{T_s}^{T_l} C(T)_{app} \, dV_e}{V_e} \tag{3-17}$$

The resultant energy equation from this formulation can be written as:

$$C_{eff} \frac{\partial T}{\partial t} = \nabla(k \nabla T) \qquad \text{in } \Omega \tag{3-18}$$

(iii) Modified Effective Capacitance Method [75]:

This is a modified version of the effective capacity method. It can account for the predicted temperature field that corresponds exactly to the heat loss. This method is even more complex to implement. Furthermore, this method might not be so suitable for high order finite elements due to the difficulty of integrating the element volume. Analytical integration of the temperature field can only be accomplished in a straightforward way for a linear tetrahedral finite element, for example.

(iv) Direct Approximation [71]:

This method allows a direct evaluation of C_{eff}, for example, using Equation (3-19) below which can be derived from Figure (3-13). This enthalpy relationship provides rather inaccurate results owing to the possibility that the temperature at a node ‘skips’ the temperature interval of phase change (ΔT_{ph}) in a single time step if the ΔT_{ph} is too small. Thus the method often leads to oscillations as a result of the step-like behaviour of the C_{eff}.

$$\begin{aligned} C_{eff} &= \rho c_s && ; \quad (T < T_s) \\ C_{eff} &= \rho c_f + \frac{L}{(T_l - T_s)} && ; \quad (T_s \le T \le T_l) \qquad (3\text{-}19) \\ C_{eff} &= \rho c_l && ; \quad (T > T_l) \end{aligned}$$

where the subscripts s, f, and l are solid, mushy, and liquid stages, respectively. Lastly, extra care must be taken when using this approach to deal with isothermal phase change problems. As shown in Figure 3-2, for instance, C_{eff} mathematically approaches infinity at T_l.

(v) Analytical/Experimental Formulation (i.e. continuous function of temperature):

The above-mentioned capacitance methods are commonly applied to handle the step-jump inputs of material properties such as specific heat and density during the phase change. Such techniques aim to minimize any possible overcounting or undercounting of the latent heat absorbed and released during the melting and solidification processes of semi-crystalline polymers, respectively. To minimize/exclude the step-like (discontinuous) behaviour of the material properties, their non-linear thermal correlations can be described by sets of equations constructed from experimental data; such as the thermal properties of polymers are written as a continuous function of temperature.

The analytical expression of material properties has been widely used in the modelling of rotational moulding. This is because the analytical formulation provides a more realistic and smoother change in the thermal properties of the polymers. Thus the use of any sophisticated phase change algorithms has often been overlooked; presumably, the realistic data could help to minimize the effect of over-estimating or under-estimating the latent heat. As a result, the non-linear thermal properties are just obtained via any straightforward numerical method such as a simple *averaging method*. The value of c_p, for example, can be computed from the average element temperature, T^e, through the analytical specific heat equation taken from [56].

$$c_p = \left[\frac{\delta(U+pV)}{\delta T}\right]_p = \left[\frac{\delta \tilde{h}}{\delta T}\right]_p = -3055 + 16.4 * T^e \tag{3-20}$$

where the c, U, $\tilde{h}$, T and subscript p are the specific heat, internal energy, enthalpy of a polymer, temperature and pressure, respectively. Lastly, the use of analytical equations such as Equation (3-20) does increase the computational non-linearity and resources required.

3.2.3.3 Source-based Approach

The latent heat can also be treated as a source term in the energy equation. Such an approach is found in the fictitious heat flow method and crystallization kinetics energy method.

(i) Fictitious heat flow method [71,73,76,78,85,90]:

Rolph and Bathe [73] developed and incorporated the technique into the finite element analysis for solving isothermal and non-isothermal problems; in which a heat-flow accumulation concept was employed to represent the liberated latent heat. The central idea of this method is to lump all the latent heat available at a node that may then release/absorb the latent heat as an internal heat at an appropriate temperature or over a range of temperatures. In this way, the latent heat content is directly coupled with the nodal temperature. However, an iterative scheme is inevitable.

At a given time step Δt, the force vector F_i of a node i undergoing a phase change is defined as [78]:

$$F_k = \frac{(T_m - T_i)\rho c\,\Omega_i}{\Delta t} \tag{3-21}$$

where F_k is an additional heat flow (source term), Ω_i is the area of node 'i' undergoing phase change, T_i is the nodal temperature, and T_m is melting/freezing temperature. This scheme was claimed effective for monitoring the location of the phase front [71]. Usmani *et.al.* [90] showed that the technique was relatively sensitive to the time-step size indeed. Unfortunately, the details of theoretical analyses on this method are still lacking.

(ii) Enthalpy/energy of the crystallization kinetics energy:

This is an alternative way to incorporate the latent heat as a source term in the energy equation, which in fact reflects the microscopic phase change. This type of data is generally not available and experimentally difficult to obtain.

3.2.4 Spatial and Temporal Averaging Techniques

As aforementioned in *Section 3.2.3.2*, the *apparent heat capacity method* is usually accompanied by the evaluation of apparent heat capacity with averaging/approximation approaches. The averaging approaches of $\frac{\partial H}{\partial T}$ $(= C_{app})$ can either be *spatial* or *temporal* *approximation*. Both approximations do require the enthalpy formulation for calculating the C_{app} as follows:

(i) Spatial Averaging Approximation [71,76]

- Del Giudice's method

$$C_{app} = \frac{dH}{dT} = \frac{(\partial H/\partial x)(\partial T/\partial x) + (\partial H/\partial y)(\partial T/\partial y)}{(\partial T/\partial x)^2 + (\partial T/\partial y)^2} \tag{3-22}$$

- Lemmon's method

$$C_{app} = \frac{dH}{dT} = \left[\frac{(\partial H/\partial x)^2 + (\partial H/\partial y)^2}{(\partial T/\partial x)^2 + (\partial T/\partial y)^2}\right]^{1/2} \tag{3-23}$$

(ii) Temporal Averaging Approximation: A simple backward difference method [76,81]

- $$C_{app} = \frac{dH}{dT} = \left[\frac{H^n - H^{n-1}}{T^n - T^{n-1}}\right] \tag{3-24}$$

The approach is explicitly computed for the C_{app}, where the superscripts n and $n-1$ represent the previous time steps. Compared to the spatial approximation, the temporal averaging approximation of Equation (3-24) is more widely used due to its simplicity and relatively smaller computational storage required.

CHAPTER 4

DEVELOPMENT OF NEW SLIP FLOW MODELS FOR ROTATIONAL MOULDING

4.1 Consideration of Slip Flow (Static-Bed Flow) Models

During the heating cycle of rotational moulding, the flow pattern of the tumbling powder might change gradually in tandem with its physical transformation from solid to molten, and thus its continuous mass fraction decreases inside the revolving mould. From the modelling viewpoint, this tumbling powder is regarded as a two-phase system, which consists of a continuous phase (air) and a discontinuous phase (powder particles). However, the powder can be treated as a continuous phase if it flows at a high rate [18]. Although a continuous powder does not appear likely in the rotomoulding system, which is a slow rotational process, it is still commonly used to model the process by other workers, and has also been used in this study. This is to simplify the numerical computations in the multivariable rotomoulding system. Based on the assumption of a continuous powder therefore, no consideration is required of such parameters as particle shape, particle size distributions and thermal-mechanical interaction of the tumbling powder particles [9].

In fact, it is still difficult to express the numerical descriptions of a heat transfer model exactly to the physical phenomenon of rotational moulding using a two-phase model. For instance, the powder flow was found to be not accurately represented either by the discontinuous form of *multibody elastic* or *viscoelastic impact models* when they were used to simulate slow powder flow [18].

Choosing one model over another requires a good deal of caution. Among the avalanche flow, circulating-bed flow and slip flow of tumbling powders, the first two probably give a more realistic enclosed flow motion of the powders. They may require some methods of tracking the upper boundary of the mixing bed and the locations of the powder pool inside the mould. Thus, their computational implementation can be are laborious. In contrast, the slip-stick flow characteristic of *Coulomb flow powder* is simpler and more suited to modelling using the continuum finite element procedure. This is because of the simplicity of the slip flow pattern and the ease and feasibility of the *coincident node technique* [67] to model such flow. In addition, the 1-D static models developed by Liang [11,56] and Sun *et al.* [42,43] have predicted relatively satisfactory results. For the extension of the numerical analyses from a 1-D model to a 2-D model, a static model may possess advantages in terms of the numerical simplicity, flexibility and accuracy especially for the modelling of the heating stage of the polymer powder.

The thermal behaviour of rotomoulding is dynamic, unsteady-state, non-isothermal and non-Newtonian. Apparently, an ideal form of the static models should begin with a mathematical model described by a set of partial difference equations such as the laws of conservation of mass, energy and momentum. These types of the mathematical models require more computational effort for solutions, and they do not seem to provide accurate descriptions. For example, the predictions of Attaran's model [45] do not correlate well with the engineering approximations of the rotomoulding process.

Two types of the slip flow model have been developed here - SDM and MDM models. The two models have differences in the thermal description for the internal air energy equation and the computational procedure for Development of New Slip Flow Models for Rotational Moulding Similarly, they are described in terms of diffusion processes without any fluid flow. As noted in many papers about rotational moulding [11,14,38,42,56], the energy equation is reasonably sufficient to describe the heat transfer problem for this non-newtonian, low-shear, pressure-free process. This is because the high viscosity of the molten polymer retards the melt from flowing along the mould surface under the process conditions, making the consideration of momentum transfer unnecessary [22,25]. Since the *Coulomb flow powder* that exhibits slip flow occurs only in a slow and smooth revolving mould [2], the surface friction between the polymer bed and the mould can be omitted. The re-contact time and residence time for the slip flow polymer are also neglected due to the lack of technical descriptions for the tumbling powder.

4.2 Description and Development of Slip Flow Models

In rotational moulding, the slow motion of the mould effectively separates the powder pool into two regions - *stagnant pool* and *mixing pool*, as depicted in Figure 4-1 [14].

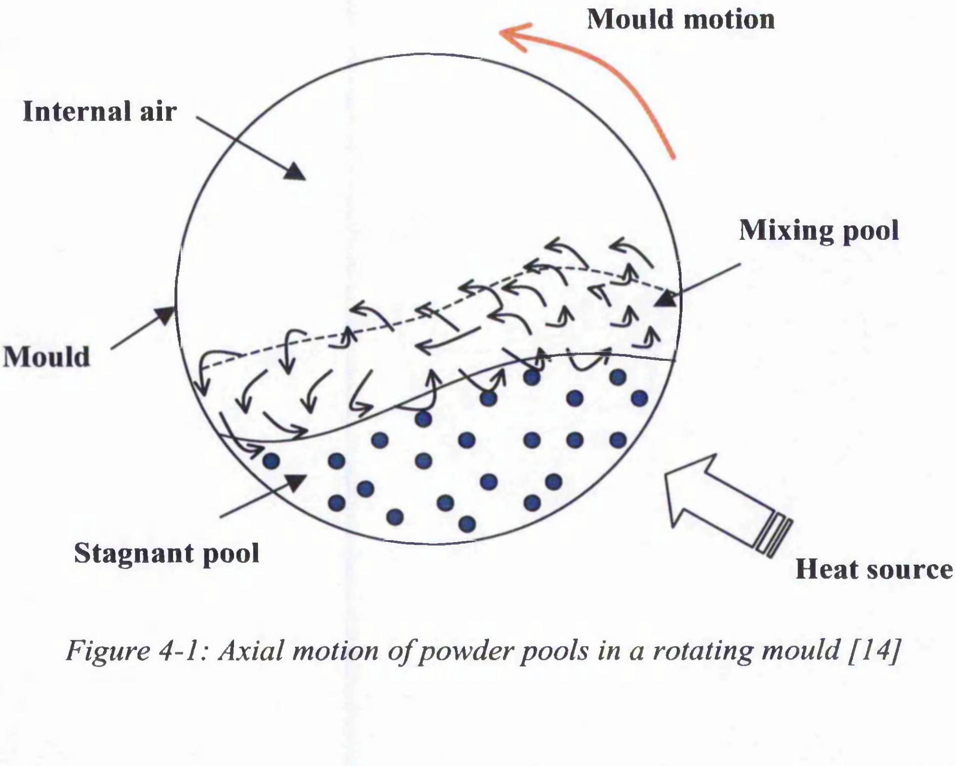

Figure 4-1: Axial motion of powder pools in a rotating mould [14]

This figure also illustrates that only the lower surface of the stagnant pool is in a perfect contact with the inner mould surface, while the outermost surface of the mixing pool is exposed to the internal air. The heat is transferred to the stagnant pool mainly via conduction. On the other hand, the heat exchange between the mixing pool and its surrounding media is commonly accepted as occurring by means of convection. This is because of the powder tumbling effect during the *induction time* in the rotomoulding.

As shown in Figure 4-2, the domain of the slip flow model has been categorized into a stagnant bed and a mixing bed, which represent the stagnant pool and mixing pool, respectively. The beds are readily formed into the mould shape from the onset of the heating cycle. They are treated as a monolithic structure sticking onto the inner mould surface, and thus no powder mixing is considered. Consequently, the predefined mesh of the models is used throughout the modelling, which has simplified greatly the computational requirements.

Although the mixing bed is computationally projected onto the inner mould surface, the convective heat transfer to the bed is still a dominant factor. It is achieved by abutting the outermost surface of the mixing bed with the *coincident node technique* [67]. The technique provides an 'invisible' internal air domain, which permits a thermal break between the mould and the mixing bed. Firstly, this is considered to be indirect heat transfer between the mixing bed and its outermost adjacent medium (mould or polymer). Secondly, it is explicitly used with the *lumped-parameter system* [70] to account for the thermal balance of the internal air, which is heated up by the mould or the molten polymer. Since the stagnant pool remains still at the bottom of the mould, the stagnant bed is easily represented by FEM.

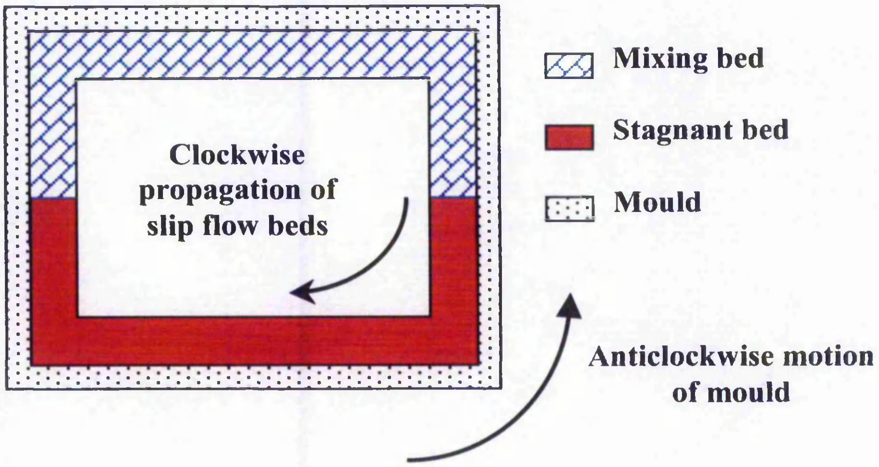

Figure 4-2: Geometrical domains of slip flow models

Before the slip flow beds reach the pre-assigned sticking temperature, their elemental domains in Figure 4-2 will change their status gradually either from the stagnant bed to mixing bed or vice-versa. This cyclic dislocation/alteration mimics the slip-stick flow of the powder inside the actual revolving mould. It also ensures that the plastic domains spend varying times against the inner mould surfaces. While the cyclic dislocation continues, the beds will revisit and reprise on the initial coordinates of the model. Numerically, this circumvents the need for finding the new interactive locations between the slave and master elements, and thus it avoids the reconstruction of the *Jacobian* matrices in the finite element procedures. During the dislocation, the observation points (nodes of data plotting) move along with the stagnant bed to assure that the polymer temperatures are consistently taken from the stagnant bed, for example.

4.2.1 Single-layer Deposition Method (SDM)

In this slip flow model, the 'macroscopic deposition' of the mixing bed is assumed to take place between the mould surface and the bed. When some portion of the mixing bed reaches the polymer melting temperature, it will deposit and stick onto the mould surface. This is accompanied by a decrease in the exposed inner mould surface. The process continues until all the mixing bed has been deposited onto the mould surface.

4.2.2 Multi-layer Deposition Method (MDM)

In practice there is some polymer still free flowing inside the mould during the first-third of the heating cycle [18]. A relatively good conductive mould would expedite the melting and coating processes of the polymer onto its surface, leaving the un-melted powder to tumble inside the coated plastic layers. Thus the direct heating of the remaining powder and the internal air is not dependent on the mould surface but the coated layers. To examine these effects, it would be sensible to 'macroscopically' consider the deposition of the mixing bed on layer-by-layer basis. The 'layer-based deposition' is presumed to be the result of *plastic layer segregation* from the mixing bed due to the density deviations of the polymer layers after phase change instead of the *particle segregation*. The deposited mixing layer is termed *deposited mixing bed*. The process is continuous until all the mixing bed has been deposited.

4.2.3 Semi-implicit Approach for Internal Air of a Rotational Mould

At a low speed of mould revolution, the tumbling polymer powder remains on the lower mould surface. The tumbling mechanism has created a dynamical moving boundary between the powder and the internal air, making the heating modelling difficult. When the powder melts, another moving boundary appears at the melt front. These simultaneous moving boundaries have made the process modelling difficult even by continuum-based techniques. As far as the accuracy of the predicted internal air temperature is concerned, an ideal thermal model should comprise these heat transfer mechanisms to some extent. The scope of the considerations will depend on the capabilities of the numerical model imposed.

A *semi-implicit approach* is developed and incorporated into the slip flow models in order to surpass the limitations of the FEM. In this methodology, the *lumped-parameter system* [70] and *coincident node technique* [68,69] have been incorporated with the *Galerkin Finite Element Method* [74,87] to compute the resultant internal air temperature, which is due to a multi-thermal interaction between the air, the polymer and/or the mould. In slip flow models, the possible heating interactions involved by the internal air can be:

1. External air → Mould → Internal air ←→ Mixing bed
2. External air → Mould → Stagnant bed → Internal air
3. External air → Mould → Deposited mixing bed →Internal air → Mixing bed

They are mathematically described by Equation (4-7) below.

4.3 Governing Equations of Rotational Moulding Process

The fundamental transport of thermal energy in and out the rotomoulding system dominates the process cycle. From the viewpoint of the rotomoulding process, which involves a slowly rotating mould, phase change, warpage, shrinkage, powder segregation, high molten polymer viscosity and complex tumbling heating powder, it is not possible to develop a simple mathematical model satisfying all the requirements. With the continuum powder assumption, the rotomoulding solution can be governed by partial differential equations with corresponding boundary conditions [74]. Here, the non-linear thermal problem of the rotational moulding is therefore modelled using the transient energy model.

4.3.1 Heat Transfer within Mould

A straightforward transient heat conduction equation is used to describe the heat transfer through the mould. The mould properties are kept at a constant value since they are relatively insensitive to the temperature changes of the mould.

$$\rho_m c_m \frac{\partial T}{\partial t} = \left[\frac{\partial}{\partial x}(k_m \frac{\partial T}{\partial x}) + \frac{\partial}{\partial y}(k_m \frac{\partial T}{\partial y}) \right] \tag{4-1}$$

The subscript m stands for mould. The variables T, t, c, ρ, and k are the temperature, time, effective specific heat, effective density and effective thermal conductivity, respectively.

4.3.2 Heat Transfer within Polymer

The thermal transfer of polymer is governed by non-linear transient conduction, Equation (4-2), in which the subscript p stands for polymer.

$$\rho_p c_p \frac{\partial T}{\partial t} = \left[\frac{\partial}{\partial x}(k_p \frac{\partial T}{\partial x}) + \frac{\partial}{\partial y}(k_p \frac{\partial T}{\partial y}) \right] \tag{4-2}$$

The discrete form of thermal parameters c_p, k_p and ρ_p are temperature dependent. The latent heat absorbed or released for phase change is directly incorporated into the effective heat capacity, *cf.* Chapter 5.

4.3.3 Initial Condition

The initial temperatures for the mould and polymer are assumed to be same.

$$T_o = T(x,y,t) = T(x,y,0) \tag{4-3}$$

4.3.4 Boundary Condition 1: Between external air and mould surface

Outside the mould a homogeneous temperature of the external/ambient forced air, T_{ex}, is assumed. The efficiency of external heating or cooling method can be directly represented by the value of external heat transfer coefficient, h_{ex}. The heat is transported due to convection at the external mould surface, S_{ex}, as:

$$-k_m \frac{\partial T}{\partial n} = h_{ex}(T - T_{ex}) \qquad \text{on } S_{ex} \qquad (4\text{-}4)$$

where n is the unit outward normal from each surface. The subscript ex is ov for the heating cycle and is oc for the cooling cycle, respectively.

4.3.5 Boundary Condition 2: Between mould and stagnant bed

The bulk flow of the stagnant pool is relatively still, where heat conduction is a dominant factor. A continuous heat flux, therefore, is imposed to the mould-stagnant bed interface, S_{mp}, of the model.

$$-k_m \frac{\partial T}{\partial n} = -k_p \frac{\partial T}{\partial n} \qquad \text{on } S_{mp} \qquad (4\text{-}5)$$

4.3.6 Boundary Condition 3: Between innermost surface of static bed and internal air

At the innermost surface, S_a, of the *static bed* (stagnant bed and mixing bed), the heat transports are treated with the convective heat term, as shown in Figure 4-3. It is described by:

$$-k_p \frac{\partial T}{\partial n} = h_{in}(T - T_a) \qquad \text{on } S_a \qquad (4\text{-}6)$$

where subscript a is internal air, and h_{in} is heat transfer coefficient at the interface of the static bed and internal air. The boundary condition can also apply to the modelling of the internal forced cooling.

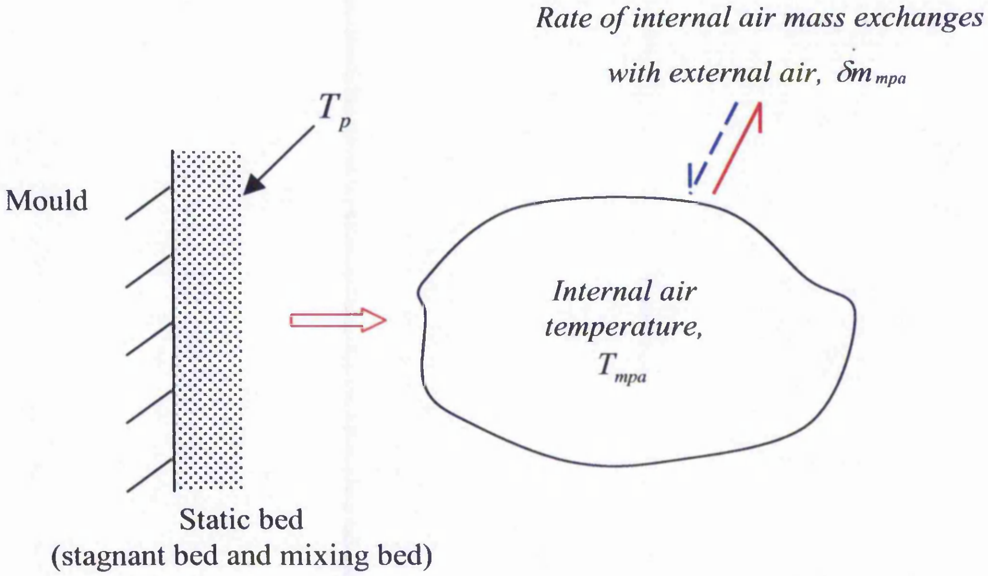

Figure 4-3: Thermal interaction of Mould/Static bed/Internal air (Mould → Static bed → Internal air, T_{mpa})

4.3.7 Boundary Condition 4: At outermost surface of mixing bed or warpage problem

In practice the heat is transferred from the mould or the portion of the sticking molten bed to the mixing pool by convection. Thus the mixing bed is introduced and formed by imposing a thermal break at its outermost surface using the *coincident node technique* [91]. The technique has been developed by Samonds [91] to deal with the air-gap problems. Thus it can incorporate easily into the Galerkin finite element method for the warpage problem. The computational detail of this boundary condition is thoroughly presented in Chapter 5.

4.3.8 Heat Transfer within Internal Air (Ideal Gas Assumption)

In the rotational moulding process, the heating and cooling times are commonly determined by the average internal air temperature inside the mould. Thus the fluid can be treated as a bulk air, which can be numerically represented by the *lumped-parameter approach* [70]. This approach assumes a uniform distribution of the air temperature within the control volume. Consequently, the heat transfer process within the bulk air is in quasi-equilibrium.

The energy equation of the bulk air inside the control volume of a mould can be written as:

Thermal energy balance for the internal air = *Heat exchange between the external air and the internal air* + *Heat exchange between the inner mould surface and the internal air* + *Heat exchange between the internal air and the mixing bed*

\+ *Heat exchange between the deposited mixing bed and the internal air* + *Heat exchange between the static bed and the internal air*

$$(m+\delta m_\gamma)c_{a,v}\frac{\partial T_\gamma}{\partial t} = \dot{\delta} m_\gamma\, c_{a,p}(T_{ex}-T_\gamma) + \int\limits_{S_{am}} h_{am}(T_{am}-T_\gamma)\partial S_{am} + \int\limits_{S_{ap}} h_{in}(T_{ap}-T_\gamma)\partial S_{ap}$$
$$+ \int\limits_{S_{pa}} h_{in}(T_{pa}-T_\gamma)\partial S_{pa} + \int\limits_{S_a} h_{in}(T_p-T_\gamma)\partial S_a \qquad (4\text{-}7)$$

The net inner air mass exchanges with the external air, δm, is considered by the implicit case only. The subscript γ can be either map or mpa (refer to Figures 4-3 to 4-5). The subscripts: am describes the interface of mould/internal air, ap describes the interface of internal air/outermost mixing bed, and pa describes the interface of deposited mixing bed/internal air. h is the heat transfer coefficient, m is the mass of the air inside the mould, δt is the time step and S is the heat transfer surface. The constant $c_{a,p}$ and

$c_{a,v}$ are the specific heat of air at constant pressure and volume, respectively [56]. Equation (4-7) indicates that the lumped-parameter analysis has neglected the internal resistance of the medium in comparison with the external resistance, mainly due to the poor thermal conductivity of air.

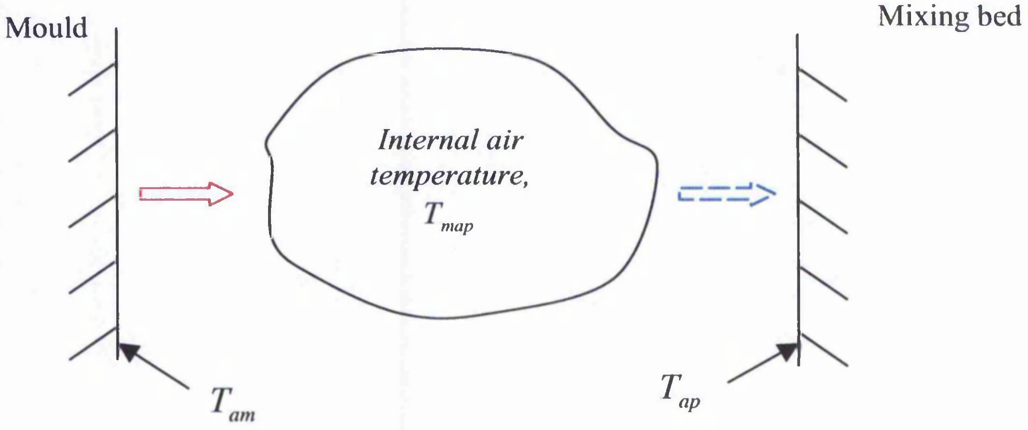

Figure 4-4: Thermal interaction of Mould/Internal air/Mixing bed (Mould → Internal air, T_{map} → Mixing bed)

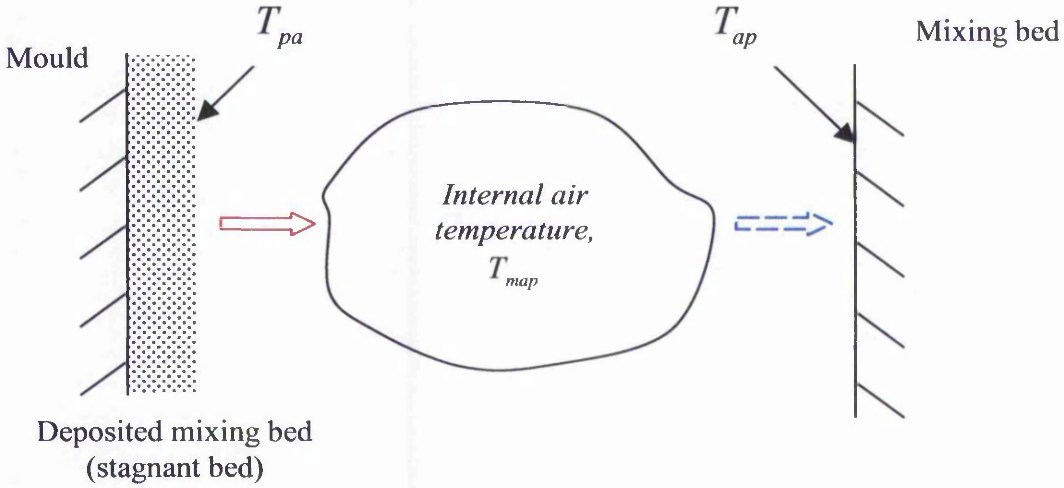

Figure 4-5: Thermal interaction of Deposited mixing bed/Internal air/Mixing bed (Deposited mixing bed → Internal air, T_{map} → Mixing bed)

During the heating cycle the second addend at the right-hand-side of Equation (4-7) contributes to the direct heating of the internal air by the mould. The absence of this term implies:

1 SDM model: The deposition of the entire mixing bed has completed. The polymer, as depicted in Figure 4-3, solely heats up the internal air. The overall internal air temperature, T_a, in Equation (4-8) is equal to T_{mpa}.

2 MDM model: The first layer of the mixing bed has deposited onto the mould after reaching its sticking temperature. The thermal interaction of the 'deposited mixing bed/air/mixing bed' begins (Figure 4-5) and proceeds across the mixing bed.

As shown in Figures 4-3 to 4-5, the consequence of utilizing the above semi-implicit approach on Equation (4-7) yields T_{map} and T_{mpa}. They appear due to the explicit and implicit computations for the interaction of the 'mould/air/mixing bed' or 'deposited mixing bed/air/mixing bed', and the interaction of 'mould/static bed/air', respectively. Thermodynamic equilibrium between the two resultant fluids is assumed after the computations, which generates the final quasi-equilibrium internal air temperature, T_a, as:

$$T_a = \nu T_{mpa} + (1-\nu)T_{map} \tag{4-8}$$

$$\nu = \nu(\delta_p, \widetilde{T}_p) \tag{4-9}$$

The thermal interactive fraction of internal air ν is in the range of $0 \leq \nu < 1$. It is a function of plastic part thickness, δ_p, and mean temperature of the mixing bed, $\widetilde{T}_p$. Here, the ending of 'mould/air/mixing bed' interaction is associated with the onset of the 'deposited mixing bed/air/mixing bed' interaction. However, they are sharing the same mathematical term. The latter is also represented by T_{map} for the ease of mathematical expression in Equation (4-8).

At this stage the percentages of energy exchanges between the mould, powder and internal air are ambiguous due to their complex thermal interactions inside a rotating mould, and the continuously decreasing powder mass during the actual heating cycle. There is no well-established function ν available at present for rotational moulding. Thus the experimental results of Liang [11], up to $12\,mm$ part thickness, and Nugent [14] have been used for studying the predicted results, the feasibility of the numerical methodology and the correlation of ν to the process.

4.4 External Heat Transfer Coefficients for Rotational Heating Processes

In rotational moulding, the external heat transfer coefficient, h_{ov}, is commonly used to represent the method of forced heating (as well as the cooling process). The parameter is strongly dependent on the flow velocity, flow region, presence of turbulence, surface geometry and fluid properties such as dynamic viscosity, density, and thermal conductivity [60]. h_{ov} can be assigned to a constant value or to vary with locations and time [38]. The latter reflects a more realistic process condition, especially when a highly non-symmetric forced convection exists. However, this approach renders the computation more tedious. Generally, a constant h_{ov} is successfully applied to most rotational moulding models [37,52,53]. By 'calibrating' the computer predicted results to fit with the experimental data, alternatively, the variation of h_{ov} can be obtained and applied to the rotational moulding models [11]. The fundamental formulation of the approach is described in Long [60], and hence it will not be discussed further herein.

In the dynamical rotomoulding condition, it is not possible to measure and to select the value for h_{ov} without any bias since h_{ov} varies with the mould surfaces. The variation of h_{ov} within a reasonable margin, with respect to different weights of powder used, is proposed here. The following reasoning supports the suggestion:

1. The main intention is to compensate the pre-arranged slip flow beds at the onset of the heating simulation, which is not similar to the physical heating state of the rotational moulding.

2. The arms of the rotomoulding machine and the mould carrier (spider) also act as a shield causing fluctuations in h_{ov} during the moulding process. In addition, the experimental values of h_{ov} were indeed found to be within a range of 8–13 W/m^2K in [14].

3. The experimental values of h_{ov} are determined by the positions of the thermocouples placed on the mould surface facing the external source, as sketched in Figure 4-1. Since the mixing rate of the powder might vary with the compactibility of the mould, therefore, the thermocouples should be placed and biased towards the mould surface frequently retaining the powder. This is because the heat transfer towards the surface plays a relatively significant role in heating up and melting the powder. For example, the 'overall' tumbling powder in a less-packed mould (little powder mass or thin part) will expect to have more frequent contacts with the hotter inner mould surface due to a relatively fast

mixing rate. From the perspective of the above interpretation, the mean h_{ov} of a thin part might be slightly higher. Therefore, it can be set at the highest value in the range for the experimental h_{ov}, and vice-versa.

Finally, the variations in h_{ov} are treated by how frequently the overall powder spends against the hot surfaces inside the mould (i.e. Figure 4-1), which is as a result of the variation of the mixing intensity for different powders inside the fixed volumetric mould. Of course the closer the mould surface to the external heat source, the higher the mean value of h_{ov}. With this methodology, the fast, medium and slow mixing rates (with respect to fixed volume of mould) arise. These refer to the cases describing thin, medium and thick parts, respectively, and are categorized by different average h_{ov}.

Based on the above statements, it is sensible to categorize the heating coefficients within a reasonably narrow margin for different ranges of part thickness, *cf.* Chapter 6. For any rotomoulding modelling, of course, a single value of h_{ov} is the most desirable in order not to be restricted by the thickness of the parts.

CHAPTER 5

IMPLEMENTATION OF FINITE ELEMENT METHOD FOR ROTATIONAL MOULDING FORMULATIONS, PHASE CHANGE AND WARPAGE

5.1 Galerkin Finite Element Approximation

The Galerkin-weighted-residual finite element method is used to discretize the partial differential equation (PDE) in the rotational moulding system. In the Galerkin method, the weighted residual, ψ_i, is chosen to be equal to the shape function, N_i. Here, $T = \tilde{T}(x,y,t,N)$ is used for the convenience in the following mathematical expressions. By introducing the residual, *cf.* Equation (3-6), into Equations (4-1), (4-2), and (4-7), these become:

$$\hat{R}_m(x,y,t;N) = \rho_m c_m \frac{\partial T}{\partial t} - \frac{\partial}{\partial x}(k_m \frac{\partial T}{\partial x}) - \frac{\partial}{\partial y}(k_m \frac{\partial T}{\partial y}) \tag{5-1}$$

$$\hat{R}_p(x,y,t;N) = \rho_p c_p \frac{\partial T}{\partial t} - \frac{\partial}{\partial x}(k_p \frac{\partial T}{\partial x}) - \frac{\partial}{\partial y}(k_p \frac{\partial T}{\partial y}) \tag{5-2}$$

$$\begin{aligned}\hat{R}_a(x,y,t;N) = {} & \rho_a c_{a,v} \frac{\partial T_\gamma}{\partial t} - \delta \dot{m}_\gamma\, c_{a,p}(T_{ex} - T_\gamma) \\ & - \left[\int_{S_{am}} h_{am}(T_{am} - T_\gamma)\partial S_{am} + \int_{S_{ap}} h_{in}(T_{ap} - T_\gamma)\partial S_{ap} + \int_{S_{pa}} h_{in}(T_{pa} - T_\gamma)\partial S_{pa} + \int_{S_a} h_{in}(T_p - T_\gamma)\partial S_a \right]\end{aligned} \tag{5-3}$$

5.1.1 Spatial Discretized Governing Equations

Equations (5-1) and (5-2) above are further simplified by employing the previous mentioned Galerkin weighted residual procedure, the integration by parts method and the appropriate boundary conditions from Equations (4-4)–(4-6). After some rearrangement, Equations (5-1), (5-2) and (5-3), yield the desired residual equations, *cf.* Equations (5-4), (5-5), and (5-6), respectively.

Spatially discretized governing equation of mould

$$\int_{\Omega^e} \rho_m c_m N_i N_j dxdy \frac{\partial T_j}{\partial t} + \left[\int_{\Omega^e} \left(k_m \frac{\partial N_i}{\partial x}\frac{\partial N_j}{\partial x} + k_m \frac{\partial N_i}{\partial y}\frac{\partial N_j}{\partial y} \right) dxdy + \int_{\Gamma^e} h_{ex} N_i N_j \partial S_{ex} \right] \{T_j\}$$
$$= \int_{\Gamma^e} h_{ex} T_{ex} N_i \partial S_{ex}$$

(5-4)

where subscripts $i, j = 1,2,...,n$ stand for the element nodes of an element, e, and n is the total number of nodes per element.

Spatially discretized governing equation of polymer

$$\int_{\Omega^e} \rho_p c_p N_i N_j dxdy \frac{\partial T_j}{\partial t} + \left[\int_{\Omega^e} \left(k_p \frac{\partial N_i}{\partial x}\frac{\partial N_j}{\partial x} + k_p \frac{\partial N_i}{\partial y}\frac{\partial N_j}{\partial y} \right) dxdy + \int_{\Gamma^e} h_{ap} N_i N_j \partial S_a \right] \{T_j\}$$
$$- \int_{\Gamma^e} h_{ap} N_i N_{mpa} \partial S_a T_{mpa} = 0$$

(5-5)

The last term at the left hand side (L.H.S) of Equation (5-5) will appear as a load term if internal forced cooling is utilized.

Rearrangement of governing equation of internal air (no spatial discretization)

$$(m + \delta m_\gamma) c_{a,v} \frac{\partial T_\gamma}{\partial t} + \left(\delta \dot{m}_\gamma\, c_{a,p} + \int_{S_{am}} h_{am} \partial S_{am} + \int_{S_{ap}} h_{in} \partial S_{ap} + \int_{S_{pa}} h_{in} \partial S_{pa} + \int_{S_a} h_{in} \partial S_a \right) \{T_\gamma\}$$
$$- \left(\int_{S_a} h_{in} N_j \partial S_a \right) \{T^e_{j,p}\} = \delta \dot{m}_\gamma\, c_{a,p} T_{ex} + \int_{S_{am}} h_{am} T_{am} \partial S_{am} + \int_{S_{pa}} h_{in} T_{pa} \partial S_{pa} + \int_{S_{ap}} h_{in} T_{ap} \partial S_{ap}$$

(5-6)

There is no spatial discretization needed for Equation (5-6) as the internal air model is treated as a bulk node; a zero-dimensional model. This implies the bulk node is arbitrary located within the domain, and is characterized by a single temperature $T_\gamma(t)$. Consequently, Equation (5-6) will be subjected to temporal discretization only.

When the bulk air (bulk node) temperature is *explicitly* considered in Equation (5-6), the mean value of temperatures is assumed for its corresponding surrounding media. Generally, the average approximations are sufficient to satisfy the explicit solutions. Under these circumstances, the bulk node equation is decoupled from the finite element equation. On the other hand, when the implicit formulation is imposed on the bulk air, then Equation (5-6) will have two unknowns; the additional last term on the L.H.S of Equation (5-6) is generated to relate the bulk node to the surface nodes. Lastly, a full implicit approach will be utilized after the entire polymer is deposited. This allows the approximate solution of the internal air to converge with respect to the finite element system, which is particularly useful for the warpage problem.

The completed spatial discretization for Equations (5-4)–(5-6) can be expressed in elemental matrix notation as:

$$[\underline{C}^e]\left\{\dot{T}^e\right\}+[\underline{K}^e]\{T^e\}=\{\underline{F}^e\} \qquad (5\text{-}7)$$

where a superposed dot on T denotes a derivative with time, $[\underline{C}^e]$ is the capacitance matrix, $[\underline{K}^e]$ is the stiffness matrix, and $\left\{\underline{F}^e\right\}$ is the load vector.

5.1.2 Eularian-Lagrangian Coordinate Transformation and Area Integration

The global Cartesian framework in Equations (5-4)~~-~~(5-6) is not a convenient coordinate system for the generation of function approximations, especially over elements with a different mesh size. The element shape functions in global nodal coordinates will not remain invariant and will appear as polynomial of similar degree having different coefficients at each element [96]. To overcome this problem, the global coordinate system is transformed into the local/master/non-orthogonal coordinate system to standardize the shape functions. The approach is termed the *Eularian-Lagrangian Coordinate Transformation*. As shown in Figure 5-1, the relationship between the global and local coordinate systems can be mathematically expressed as:

$$\xi = \xi(x, y, t) \quad , \quad \eta = \eta(x, y, t) \tag{5-8}$$

The local coordinates are transformed back to the global coordinate system at a later stage giving:

$$x = x(\xi, \eta, t) \quad , \quad y = y(\xi, \eta, t) \tag{5-9}$$

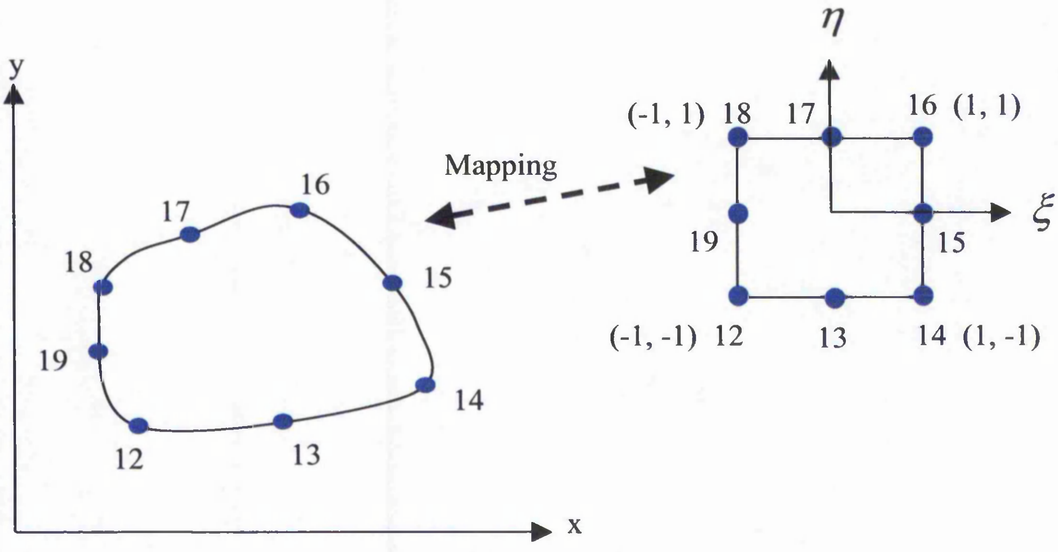

Figure 5-1: Eularian-Lagragian coordinate transformation

To achieve the coordinate transformation, one-to-one transformation between the global and the local coordinate systems is established via the *isoparametric mapping (isoparametric transformation)*. This gives [87,96]:

$$x=\sum_{j=1}^{n}N_j(\xi,\eta)x_j \quad , \quad y=\sum_{j=1}^{n}N_j(\xi,\eta)y_j \tag{5-10}$$

Thus the total node number of an element, n, becomes equal to the degree of freedom of the element. The *Jacobian matrix* of the coordinate transformation, $J(\xi,\eta)$, is:

$$J(\xi,\eta)=\begin{bmatrix} J_{11} & J_{12} \\ J_{21} & J_{22} \end{bmatrix}=\begin{bmatrix} x_\xi & y_\xi \\ x_\eta & y_\eta \end{bmatrix} \tag{5-11}$$

where

$$\begin{aligned} x_\xi &= \frac{\partial x}{\partial \xi}=\sum_{j=1}^{n}x_j\frac{\partial N_j(\xi,\eta)}{\partial \xi} \quad , \quad y_\xi = \frac{\partial y}{\partial \xi}=\sum_{j=1}^{n}y_j\frac{\partial N_j(\xi,\eta)}{\partial \xi} \\ x_\eta &= \frac{\partial x}{\partial \eta}=\sum_{j=1}^{n}x_j\frac{\partial N_j(\xi,\eta)}{\partial \eta} \quad , \quad y_\eta = \frac{\partial y}{\partial \eta}=\sum_{j=1}^{n}y_j\frac{\partial N_j(\xi,\eta)}{\partial \eta} \end{aligned} \tag{5-12}$$

and the determinant of the Jacobian matrix is:

$$|J(\xi,\eta)|=|x_\xi y_\eta - x_\eta y_\xi|>0 \tag{5-13}$$

The *inverse Jacobian* matrix is:

$$\hat{J}(\xi,\eta)=\begin{bmatrix} \xi_x & \eta_x \\ \xi_y & \eta_y \end{bmatrix}=\begin{bmatrix} \hat{J}_{11} & \hat{J}_{12} \\ \hat{J}_{21} & \hat{J}_{22} \end{bmatrix}=\frac{1}{|J|}\begin{bmatrix} y_\eta & -y_\xi \\ -x_\eta & x_\xi \end{bmatrix} \tag{5-14}$$

Using the chain rule, the derivatives of the node functions $\frac{\partial N(\xi,\eta)}{\partial x}$ and $\frac{\partial N(\xi,\eta)}{\partial y}$ can be expressed as:

$$\frac{\partial N(\xi,\eta)}{\partial x}=\hat{J}_{11}\frac{\partial N(\xi,\eta)}{\partial \xi}+\hat{J}_{12}\frac{\partial N(\xi,\eta)}{\partial \eta} \tag{5-15}$$

$$\frac{\partial N(\xi,\eta)}{\partial y}=\hat{J}_{21}\frac{\partial N(\xi,\eta)}{\partial \xi}+\hat{J}_{22}\frac{\partial N(\xi,\eta)}{\partial \eta} \tag{5-16}$$

In addition, the element area and boundary surface can also be written in terms of normalized curvilinear coordinates as:

$$\int_{\Omega} dxdy = \int_{-1}^{1}\int_{-1}^{1} |J| d\xi d\eta \tag{5-17}$$

and

$$\int_{s} dS = \int_{-1}^{1} |J_{\Gamma}| d\xi \tag{5-18}$$

where

$$|J_{\Gamma}| = \sqrt{\left(\frac{\partial x}{\partial \xi}\right)^2 + \left(\frac{\partial y}{\partial \xi}\right)^2} = \sqrt{\left(\sum_{j=1}^{s} \frac{\partial N}{\partial \xi} x_j\right)^2 + \left(\sum_{j=1}^{s} \frac{\partial N}{\partial \xi} y_j\right)^2} \tag{5-19}$$

where the subscript s is the total boundary node. Together with Equations (5-10)–(5-19), therefore, the integrals of Equations (5-4)–(5-6) could be transformed into a form appropriate for numerical evaluation. As a result, the representative matrix equation in Equation (5-7) is now constructed with respect to the (ξ,η) coordinate system.

Generally, the finite element matrices and vectors are computed with the aid of numerical integration rules, especially for those with high order finite elements. The integration rules may be Gauss rules, based on carefully chosen points within an element. Alternatively, for a simple linear element, *Newton-cotes rules* (i.e. the trapezoidal rule and Simpson's rule) based on the nodes of the elements can also be applied [71]. In this case the sampling points are spaced at equal distances [70]. The former has been adopted for area integration, because it has no additional difficulties arising when non-equally spaced sampling points are used. This approach seems to improve the accuracy [70]. With the two-dimensional 3x3 *Gauss-Legendre rule*, the area integrals of Equations (5-4)–(5-6) over the parent element can be evaluated as follows:

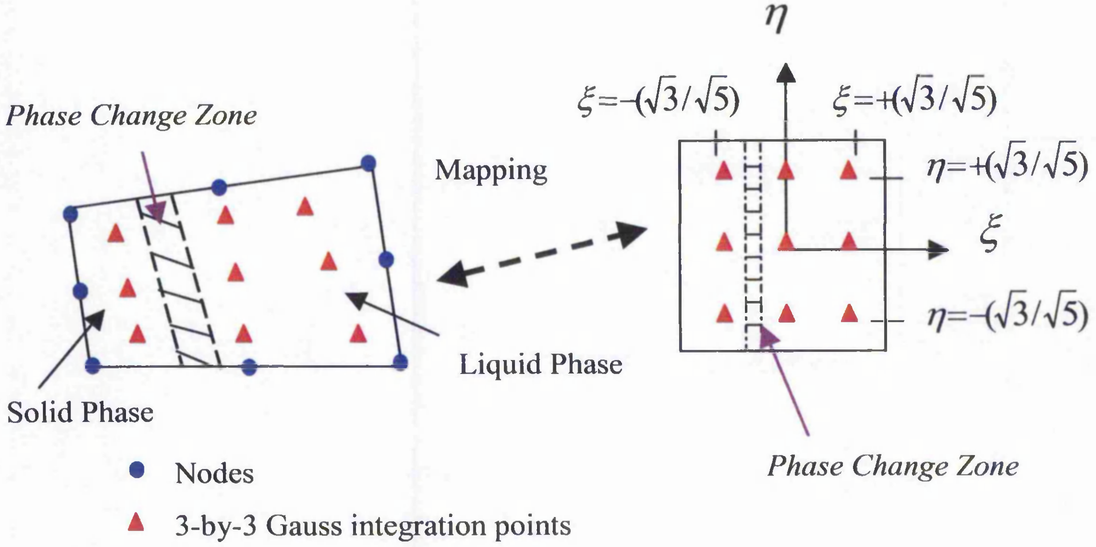

Figure 5-2: Relationship between Gauss integration points and possible phase change regions within an element

$$\int_{-1}^{1}\int_{-1}^{1} I(\xi,\eta)d\xi d\eta = \sum_{k=1}^{3}\sum_{l=1}^{3} w_k w_l I(\xi_k,\eta_l) \tag{5-20}$$

$$\int_{-1}^{1} I(\xi)d\xi = \sum_{k=1}^{3} w_k I(\xi_k) \tag{5-21}$$

where $I(\xi)$, $I(\xi,\eta)$ represent the integrands, and w_k, w_l are the Gauss quadrature weightings for the 3x3 point system (Figure 5-2).

5.1.3 Temporal Discretized Governing Equations

After the spatial discretization and coordinate transformation, Equation (5-7) can be further simplified by integrating in time either by direct/time-integration methods (using the finite element or finite difference technique) or by more formal ordinary differential equation (ODE) formulations such as linear multistep methods [82]. Here, the unconditional stable *Dupont II scheme* (with $a = 1/4$), a two-step method (three-time-level scheme), is adopted for solving the global partially discretized non-linear equations. With the coefficient $a = 1/4$, the Dupont II scheme was found to be unconditionally stable and to work very well for the non-linear energy equation [71]. It gives no oscillation and is not sensitive to the value of time step, compared with the *two-step Lees scheme*. Unfortunately, the other Dupont II schemes give less satisfactory results. Another two-step method - Lees algorithm, however, it tends to produce large errors when it is used with a larger time step.

Although the Dupont II scheme is a non-iterative scheme, the iteration is applied here due to the existence of the slip flow beds and the warpage problem. With the Dupont II scheme ($a = 1/4$), therefore, the global algebraic Equation (5-7) becomes:

$$\left[\underline{C}+\frac{3}{4}\Delta t\underline{K}\right]\left\{T^{n+1}\right\}=\left[\underline{C}\right]\left\{T^{n}\right\}-\frac{1}{4}\Delta t\left[\underline{K}\right]\left\{T^{n-1}\right\}+\Delta t\left\{\underline{F}\right\} \tag{5-22}$$

During the explicit treatment of the internal air, the *Crank-Nicolson method* ($\theta = 1/2$) is utilized, which results in the following formulation:

$$\left[\underline{C}+\frac{1}{2}\Delta t\underline{K}\right]\left\{T^{n+1}\right\}=\left[\underline{C}-\frac{1}{2}\Delta t\underline{K}\right]\left\{T^{n}\right\}+\frac{1}{2}\Delta t\left\{\underline{F}^{n+1}+\underline{F}^{n}\right\} \tag{5-23}$$

5.2 Numerical Implementation of Phase Change Algorithm

The dynamic nature of rotational moulding and the non-isothermal phase change for the semi-crystalline polymers would suggest that using the fixed domain techniques for phase changes as the most suitable option. After some consideration of the different phase change modelling techniques discussed in Chapter 3, an alternative equivalent heat capacity model incorporating an *efficient algorithm*, as developed by Hsiao and Chung [92], is adopted. This temperature-based method is relatively ease to implement, and it allows the thermal data of rotational moulding to be incorporated in a straightforward manner into the numerical model. Importantly, it can overcome the numerical deficiencies of the *direct approximation* approach *cf.* Chapter 3. In addition, the use of the *spatial* or *temporal averaging technique* for phase change optimisation can be avoided.

Any undercounting of the latent heat will lead to an underestimation of the phase change, and vice-verse. The imposed *efficient algorithm* could minimize this overcounting or undercounting of the latent heat to maintain an overall correct heat balance. This is because the central basis of the scheme is based on the contributions of all the element nodes from all the phases towards the phase change element. In addition, it also helps to avoid any possible oscillation in an iterative solution that might be attribute to the step-like behaviour of C_{eff} around the phase transition zone [71]. As shown in Figure 5-2, for example, the missing peak occurs due to the fact that the phase change region falls between the integration points [81]. If without using a special phase change algorithm, the value of some nodes might not be accounted for by the phase change within the element. This is because the corresponding nodes just reflect either solid or liquid phases (nodes sit outside the phase-change range).

In Hsiao and Chung's approach [92], the phase change had been divided into three major stages (solid, molten and liquid). In the present formulation, however, the phase transformation is further divided into four distinct phases; solid, tacky, molten and liquid. The thermal properties of these phases are represented by the subscripts s, tc, mu and l, respectively. The additional tacky zone has been incorporated to provide a smooth transition in the non-linear thermal properties during the phase change modelling.

The advantage of the *efficient algorithm* is that it takes into account the mass fraction, $\hat{m}$, of the phase change element, obtained through a linear interpolation procedure. The use of the mass fraction is appropriate to allow for the mathematical modelling difficulties arising from the discrete thermal properties of the polymer; the properties experience a step-change during the phase transition period, meaning that a direct interpolation from the parameter is not possible. With the algorithm, the $\hat{m}$ can be obtained by a linear interpolation between the nodal temperature, T_j, and the average element temperature, T_{ave}^{e}. For example, the temperature of node j located at the solid phase, which is a different phase from the average volumetric temperature of an element (i.e. liquid phase). In that case, there are four different phases existing and the mass fractions at the node are:

$$\hat{m}_{j,s} = \left| \frac{\max(T_s) - T_j}{T_{ave}^{e} - T_j} \right| \quad , \quad \hat{m}_{j,tc} = \left| \frac{\Delta T_{tc}}{T_{ave}^{e} - T_j} \right|$$
$$\hat{m}_{j,mu} = \left| \frac{\Delta T_{mu}}{T_{ave}^{e} - T_j} \right| \quad , \quad \hat{m}_{j,l} = \left| \frac{T_{ave}^{e} - \min(T_l)}{T_{ave}^{e} - T_j} \right| \tag{5-24}$$

By summing up each contribution from all the n element nodes, with the use of shape function as a weighting factor gives:

$$\hat{m}_s = \sum_{j=1}^{n} N_j \hat{m}_{j,s} \quad , \quad \hat{m}_{tc} = \sum_{j=1}^{n} N_j \hat{m}_{j,tc}$$
$$\hat{m}_{mu} = \sum_{j=1}^{n} N_j \hat{m}_{j,mu} \quad , \quad \hat{m}_l = \sum_{j=1}^{n} N_j \hat{m}_{j,l} \tag{5-25}$$

Eventually, the effective heat capacity, C_{eff}, and the effective thermal conductivity, k_{eff}, can be obtained via Equation (5-26) and Equation (5-27), respectively.

$$C_{eff}^{e} = C_s \hat{m}_s + C_{tc} \hat{m}_{tc} + C_{mu} \hat{m}_{mu} + C_l \hat{m}_l \tag{5-26}$$

$$k_{eff}^{e} = k_s \hat{m}_s + k_{tc} \hat{m}_{tc} + k_{mu} \hat{m}_{mu} + k_l \hat{m}_l \tag{5-27}$$

where C is the heat capacity and k is the thermal capacity, and the superscript e stands for an element in the finite element domain.

5.3 Coincident Node Technique [92-95]

The coincident node technique was first presented by Samonds [69] to account for the thermal break/resistance of continuum between the metal and mould in the casting process. The technique shown in Figure 5-3 is an alternative to the thin element method. Presuming that the dimensional ratio aspect of the thin element area was $\frac{\Delta y}{\Delta x}=100$, the *thin element technique* was found at most to be 0.02% different from the results of the *coincident node technique* [69]. With a higher aspect ratio for the thin element ($\frac{\Delta y}{\Delta x}=350$), Samands *et al.* [91] pointed out a maximum difference of only 1.9% occurred between the values of the two methods. This further implies that there should be very little difference in numerical behaviour.

As depicted in Figure 5-3, the coincident node elements formed by two nodes coincide

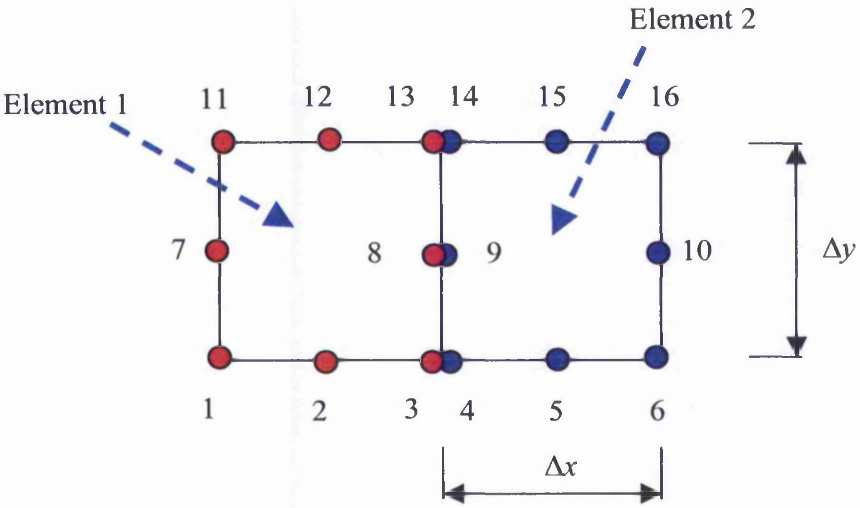

Figure 5-3: Structure of coincident node elements

at the same position; one from each interface of the two adjacent elements. According to the figure, the coincident node topology for these coincident elements can be presented as:

Coincident Element	Nodes
1	1 3 13 11 2 8 12 7 4 14 9
2	4 6 16 14 5 10 15 9 3 13 8

The relationship between the interface elements can be described by [69]

$$\left[\underline{K}_{\text{int}}^{e}\right]=\sum_{i,j=1}^{cn_I}\int_{\Gamma_{\text{int}}}\left[h_{\text{int}}N_j(N_i-\frac{1}{2}N_g)\right]d\Gamma_{\text{int}}^{e} \tag{5-28}$$

where i, j = 1, 2, ..., cn_I. The cn_I represent the total node on the coincident interface (Γ_{int}). The subscript g is the number of the node coincident with i, and the superscript e stands for an element. This integration is performed for the elements on both sides of the interface. Since the N_jN_g cross-term appears twice during the integration, this term has a factor $\frac{1}{2}$ in Equation (5-28). The final elemental conductivity matrix, $\left[\underline{K}^{e}\right]$, becomes:

$$\left[\underline{K}^{e}\right]=\left[\underline{K}^{e}\right]+\left[\underline{K}_{\text{int}}^{e}\right] \tag{5-29}$$

Conveniently, the interface condition of the coincident elements may be imposed after the mesh has been designed, i.e. simply by adding coincident nodes along the internal surface. On the other hand, the thin element approaches requires less programming effort but the additional elements will result in significant computational effects, especially for non-linear problems in which the matrix terms have to be re-integrated after each iteration. The thin element technique, therefore, is more suitable for 'one-off' applications [69], so it might not be suitable for the *slip flow model*. In addition, the terms of the thin element appear in both the $[C]$ and $[K]$ matrices, but a term only appears in the $[K]$ matrix for the coincident node technique after finite element discretization [91]. Importantly, the coincident node element does not have to be applied or be present at the entire interface boundary at all times in the slip flow model. In the worst case, the global matrices of the thin elements might be invariably ill conditioned, i.e. spurious numerical results occur, unless an extremely fine mesh is used for the solution [68].

The following demonstration is presented to exemplify some components of the conductivity matrix for an element 'abutting' a coincident node interface such as at the element nodes 3, 8 and 13 in Figure 5-3. Equation (5-30) represents the shape functions for a two-dimensional 8-noded rectangular element (serendipity family), used in this research.

$$\begin{aligned}
N_1^e &= -\frac{1}{4}(1-\xi)(1-\eta)(1+\xi+\eta) \quad ; \quad & N_5^e &= \frac{1}{2}(1-\xi^2)(1-\eta) \\
N_2^e &= -\frac{1}{4}(1+\xi)(1-\eta)(1-\xi+\eta) \quad ; \quad & N_6^e &= \frac{1}{2}(1+\xi)(1-\eta^2) \\
N_3^e &= -\frac{1}{4}(1+\xi)(1+\eta)(1-\xi-\eta) \quad ; \quad & N_7^e &= \frac{1}{2}(1-\xi^2)(1+\eta) \\
N_4^e &= -\frac{1}{4}(1-\xi)(1+\eta)(1+\xi-\eta) \quad ; \quad & N_8^e &= \frac{1}{2}(1-\xi)(1-\eta^2)
\end{aligned} \tag{5-30}$$

From Equation (5-28), the relationships of the coincident elements in Figure 5-3 are:

$$\begin{aligned}
N_3 = N_4 &= -\frac{1}{2}(1-\eta)(\eta) \\
N_8 = N_9 &= (1-\eta^2) \\
N_{13} = N_{14} &= \frac{1}{2}(1+\eta)(\eta)
\end{aligned} \tag{5-31}$$

The coincident boundary Jacobian, J_Γ, formed by node numbers 3, 8 and 13 is:

$$\begin{aligned} J_\Gamma(1,\eta) &= \sqrt{\left[J_{3,3}(1,\eta)\right]^2 + \left[J_{3,13}(1,\eta)\right]^2} \\ &= \sqrt{\left|\left(\sum_{j=3,8,13} \frac{\partial N_j}{\partial \eta} x_j\right)^2 + \left(\sum_{j=3,8,13} \frac{\partial N_j}{\partial \eta} y_j\right)^2\right|} \\ &= \left|J_{\text{int}}\right| \end{aligned} \tag{5-32}$$

Solving Equation (5-28) gives:

$$\begin{aligned} K^e_{3-3,\text{int}} &= \int_{-1}^{1} h_{\text{int}} N_3 N_3 \left|J_{\text{int}}\right| d\eta = \frac{4h_{\text{int}}\left|J_{\text{int}}\right|}{15} \\ K^e_{3-4,\text{int}} &= -\int_{-1}^{1} h_{\text{int}} N_3 \frac{1}{2} N_4 \left|J_{\text{int}}\right| d\eta - \int_{-1}^{1} h_{\text{int}} N_4 \frac{1}{2} N_3 \left|J_{\text{int}}\right| d\eta = -K^e_{3-3,\text{int}} \end{aligned} \tag{5-33}$$

During warpage formation, the thermal break at the mould interface and polymer interface will induce natural convection. The temperature gradient between the two interfaces forces the interface heat transfer coefficient, h_{int}, to change with time. Generally, the interface thermal resistance can be developed via the free convection relationship [60]:

$$h_{\text{int}} = \frac{k}{L_o} Nu_{av,L_o} \tag{5-34}$$

where:

Nusselt number, $Nu_{av,L_o} = 0.54(Gr * \text{Pr})^{1/4}$ (5-35)

Prandtl number of air, $\text{Pr} = 0.72 \frac{\mu c}{k}$ (5-36)

Grashof number, $Gr = \frac{\rho^2 g \beta \Delta T L_o{}^3}{\mu^2}$ (5-37)

where [61]:

$\frac{gL_0^3}{\mu^2}$: Characterize the importance of the buoyant forces relative to the viscous forces.

$\beta\Delta T$: Characterize the thermal expansion of the fluid.

The parameters k, c, ρ, g, μ, L_o, β, and ΔT are the thermal conductivity, specific heat, density, acceleration due to gravity, dynamic viscosity of fluid, characteristic length, volumetric coefficient of thermal expansion, and temperature difference between two media, respectively. In brief, h_{int} is dependent on the temperature difference and also the buoyancy forces relative to viscous forces (gL^3/v^3) within a warpage undergoing natural convective heat transfer as stated in Equation (5-36).

CHAPTER 6

RESULTS AND DISCUSSION

The Galerkin finite element program for rotational moulding modelling has been written in MATLAB. The available finite element data from Taylor and Hughes [97] and a heat transfer problem from Kwon and Bang [99] have been used to verify the present finite element program. The comparison for the thermal problem [99] is presented in *Appendix A*. MATLAB is chosen because of its ability to manipulate matrices and vectors with ease. The software is also well known for its built-in graphic features, which help visualisation of numerical results in graphs. The program structures of the in-house rotational moulding software, RotoFEM, are explained and diagrammatically shown in *Appendix B*.

6.1 Geometry of Slip Flow Models

A $315\,mm$ x $315\,mm$ square model is constructed for the slip flow models (SDM and MDM), as shown in Figure 6-1. This square model is developed to simplify the mesh generation and to minimize the mesh distortion. Only half of the heating model is used for the cooling modelling due to the assumption of symmetrical cooling. In fact, the geometry has an equal volume but slightly different dimension to the experimental cubical moulds given in Liang [11] and Nugent [14]. These steel-cubical moulds with $1.6\,mm$ thicknesses have a dimension of $330\,mm$ x $300\,mm$ x $300\,mm$ and a draft angle of 2.8^0.

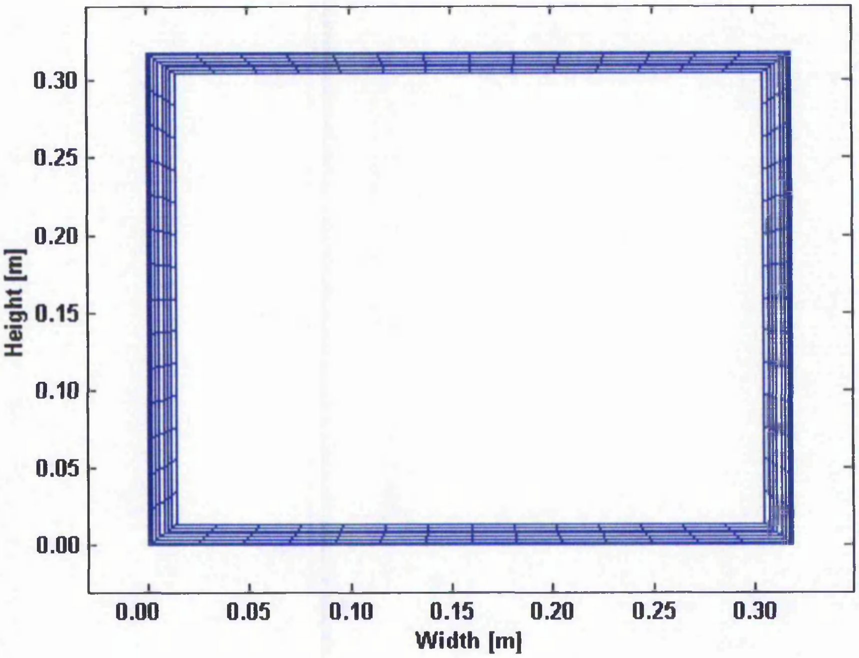

Figure 6-1: Mesh generation for a 315 mm x 315 mm square model

6.2 Determination of Average External and Internal Heat Transfer Coefficients

In the rotational moulding process, the external heat transfer coefficient due to the forced convection varies with the mould surface. In this study, the average heat transfer coefficients are numerically determined by identifying the best-fit thermal correlations between the heat transfer coefficients and the experimental temperatures for the empty mould surface. As shown in Figure 6-2, the best h_{ov} representing the experimental oven condition lies in a narrow range between $15-17\ W/m^2K$. Using the methodology of varying h_{ov} proposed in Section 4.4, therefore, the experimental oven condition still hold when the upper or the lower limit of h_{ov} is used for the modelling, as given in Table 6-1.

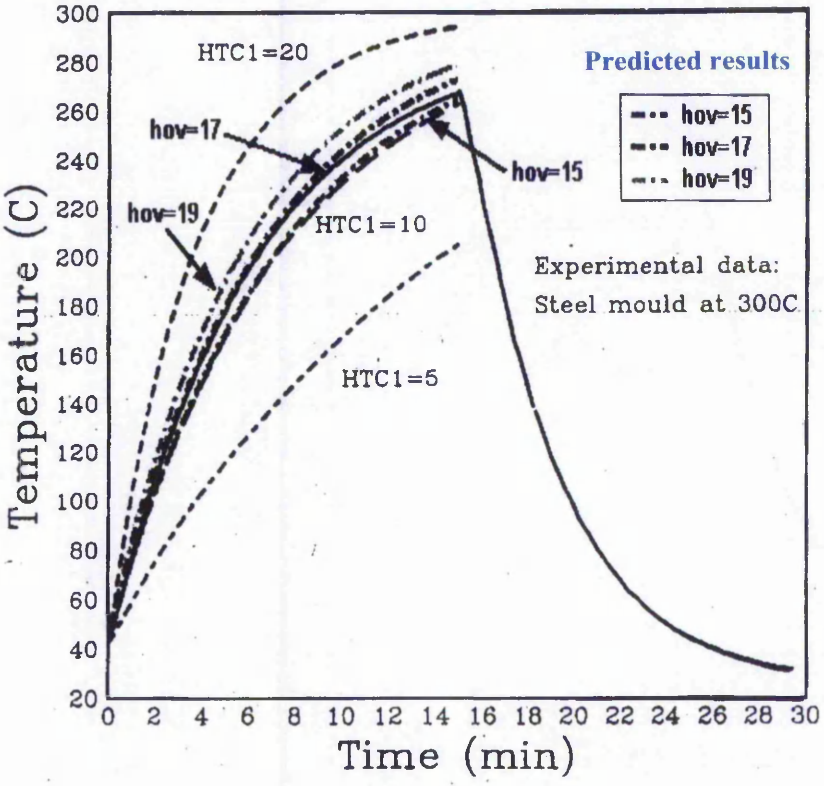

Figure 6-2: Effects of external heat transfer coefficients on the temperature of an empty mould surface during a rotomoulding heating cycle

	Thin Part	**Medium Part**	**Thick Part**	**Remarks**
Part Margin, δ_p (mm)	$0\leq \delta_p \leq 5$	$5< \delta_p \leq 9$	$9< \delta_p \leq 12$	-
h_{ov} (W/m^2K)	17	16	15	Heating
h_{ov} (W/m^2K)	8–13			Heating (Experiment - [14])
h_{oc} (W/m^2K)	22	22	22	Cooling

Table 6-1: Heat transfer coefficients for a range of rotomoulded parts of different thickness

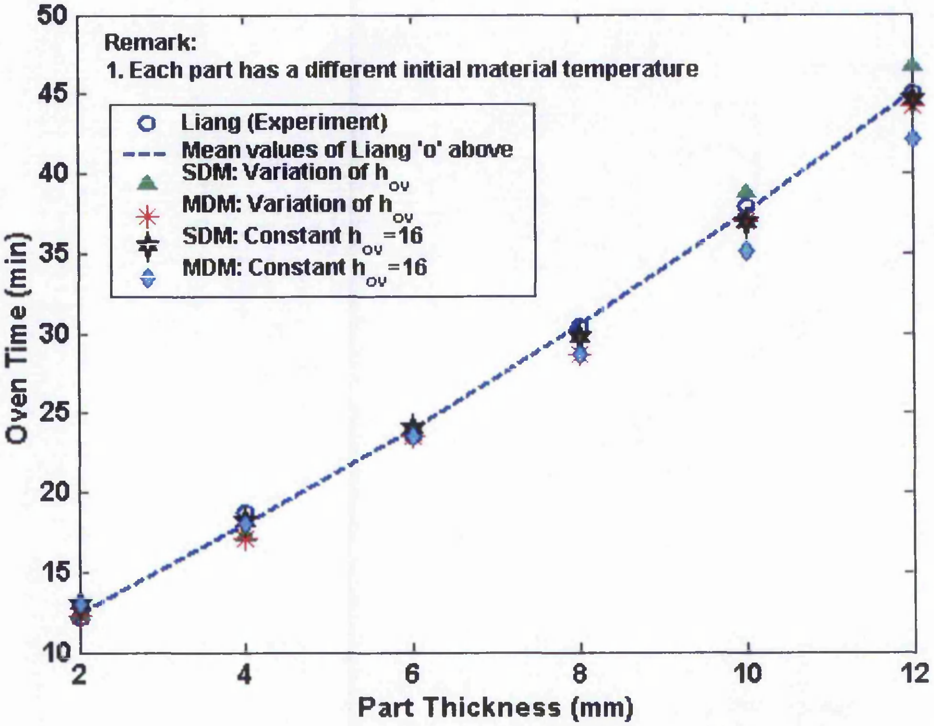

Figure 6-3: Comparisons between the experimental [11] and predicted oven times for parts with different initial and deheating temperatures

The selected h_{ov}, Table 6-1, are acceptable for the modelling since the experimental heat transfer coefficients [14] were in the wider range of 8–13 W/m^2K. The dissimilarity of h_{ov} between the present study and the experimental results could be due to the different approaches involved. To categorise parts as thin, medium and thick for different h_{ov}, *cf.* Section 4.4, the part thickness, δ_p, in Table 6-1 are assigned after testing their influences on the oven (heating) time for part thicknesses up to $12\,mm$, as shown in Figure 6-3. Table 6-1 indicates that the thicker the part the smaller the value of h_{ov}, which has satisfied the methodology of h_{ov} advanced in Section 4.4. The details of the SDM and MDM models will be discussed below.

A similar procedure has been utilized to determine the external heat transfer

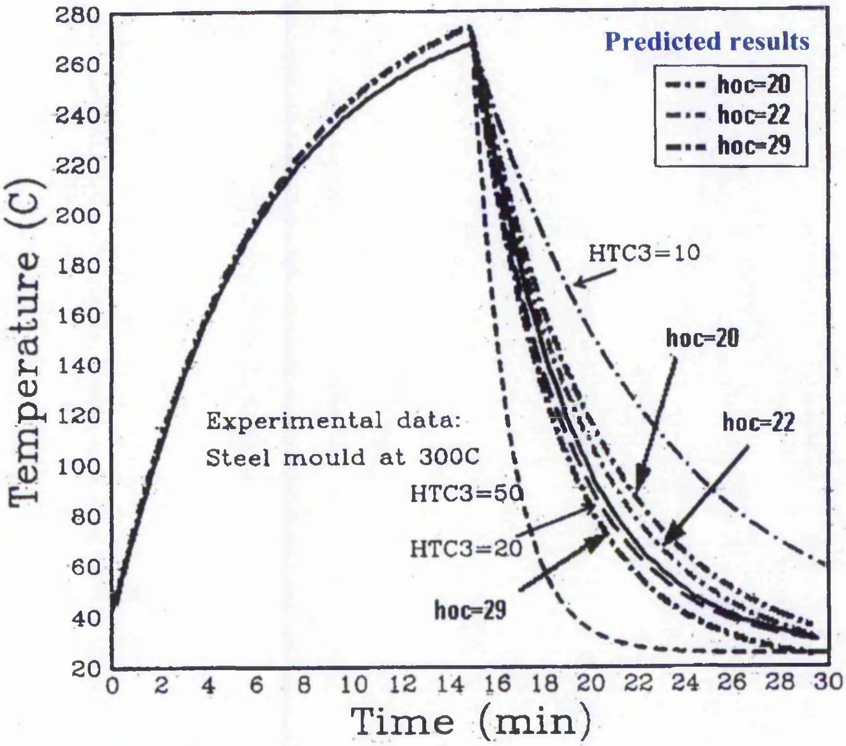

Figure 6-4: Effects of external heat transfer coefficients on the temperature of an empty mould surface during a rotomoulding cooling cycle

coefficient for the cooling process, h_{oc}. A constant mean value of h_{oc} is chosen because of the geometric similarity between the numerical and physical models during the cooling process. According to Figure 6-4, the best h_{oc} for modelling is 22 W/m^2K, which is close to the experimental value given by Nugent, 20 W/m^2K [14].

6.2.1 Perspective of Varying External Heat Transfer Coefficient for Slip Flow Models

By analysing the effects of part thickness on the predicted heating (oven) times, the perspective of varying h_{ov} for the SDM and MDM types of the slip flow model is studied. Figures 6-3 and 6-5 show that the heating time predictions by using the MDM model with varying h_{ov} between $15-17\ W/m^2K$, are close to those employing the SDM model with a constant h_{ov} of 16 W/m^2K. In addition, both methods give close agreement with the experimental data [11], as shown in Figure 6-3.

According to Figures 6-3 and 6-5, the SDM model, where h_{ov} is varied, causes overestimation of the heating times particularly in thick parts. This model tends to retard the heat transfer across the mould to the mixing bed during the initial heating period. The MDM model with constant h_{ov} underestimates the heating times. The variation of h_{ov}, within a reasonable margin, is needed for the model to 'compensate' for the assumptions of no powder mixing and pre-arranged slip flow bed. From these studies

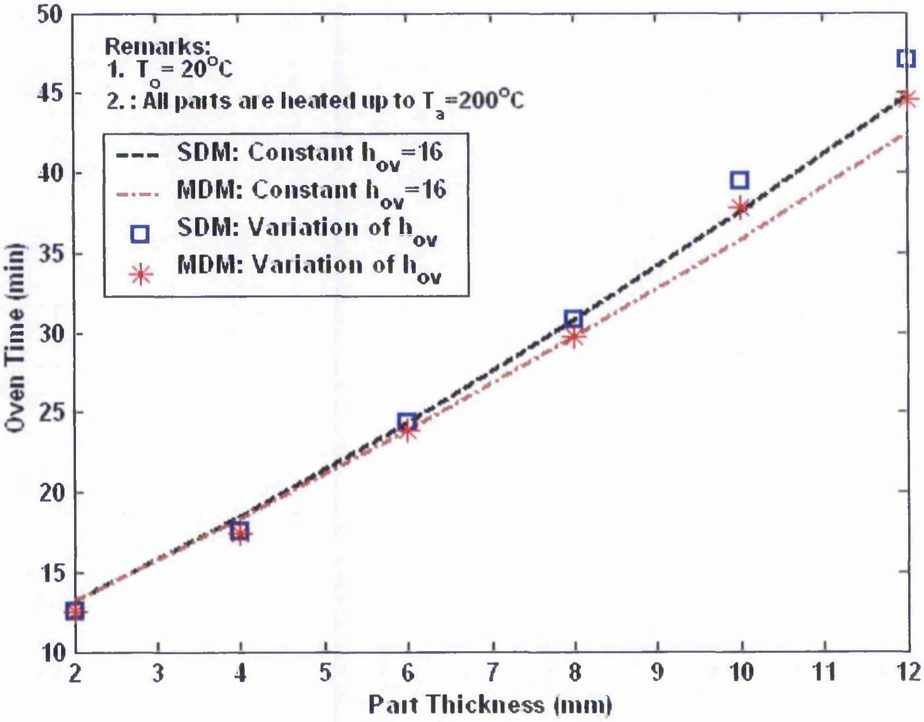

Figure 6-5: Comparisons of external heat coefficients on predicted oven times for similar parts with the same initial and deheating temperatures

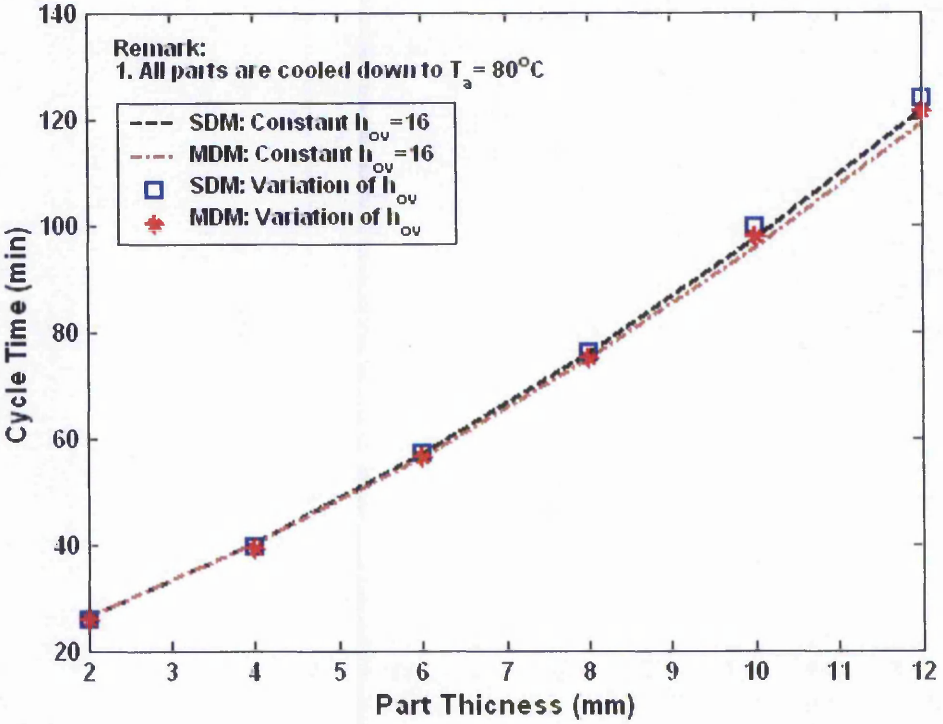

Figure 6-6: Comparisons of external heat coefficients on predicted cycle times for similar parts with the same initial and demoulding temperatures

the SDM model with h_{ov}, 16 W/m^2K, and the MDM model with varying h_{ov}, 15–17 W/m^2K, are found to provide the best predictions. Thus they are chosen for further simulations. The optimal demoulding temperature for most polymers is 80^0C or lower [14]. The cycle times (heating time plus cooling time) at this demoulding temperature of 80^0C are found to be less affected by the heating methods, as shown in Figure 6-6. Thus a 'slight/mild' inaccuracy in the predicted heating times might not decrease the accuracy of the cooling predictions.

6.3 Reliability of the Proposed Phase Change Algorithm

Figures 6.7–6.13 illustrate the different representations for the thermal properties of polymer RP246H between Liang [56] and present approach. The former is formulated by using an analytical variation with temperature, whereas the latter is defined in discrete form. In the RotoFEM program, the numerical phase changes are divided into four distinct phases; solid, tacky, molten and liquid. This allows the thermal properties to be represented in a discrete form. As tabulated in Table 6-2, each of the discrete pieces of data for the polymer RP246H is selected, over an appropriate temperature

Material	Process	Thermal Properties		
		Specific Heat, c (J/kgK)	Density, ρ (kg/m^3)	Thermal Conductivity, k (W/mK))
Mould (Thickness, $\delta_m = 1.6mm$)	Heating or Cooling	531	7817	45
Polymer (Solid)	Heating	2377.9	336.0	0.1012
Polymer (Tacky)	Heating	3981.9	343.3	0.1012
Polymer (Mushy)	Heating	9973.4	564.9	0.1893
Polymer (Liquid)	Heating	2491.7	860.3	0.2774
Polymer (Solid)	Cooling	2377.9	937.2	0.1012
Polymer (Tacky)	Cooling	3981.9	908.9	0.1012
Polymer (Mushy)	Cooling	9973.4	873.4	0.1893
Polymer (Liquid)	Cooling	2491.7	860.4	0.2774
Air (constant volume)	Heating or Cooling	728	1.1	0.027
Air (constant pressure)	Heating or Cooling	1014		

Table 6-2: Discrete thermal properties of air, mould and polymer RP246H (Abstracted or transformed from [11,14])

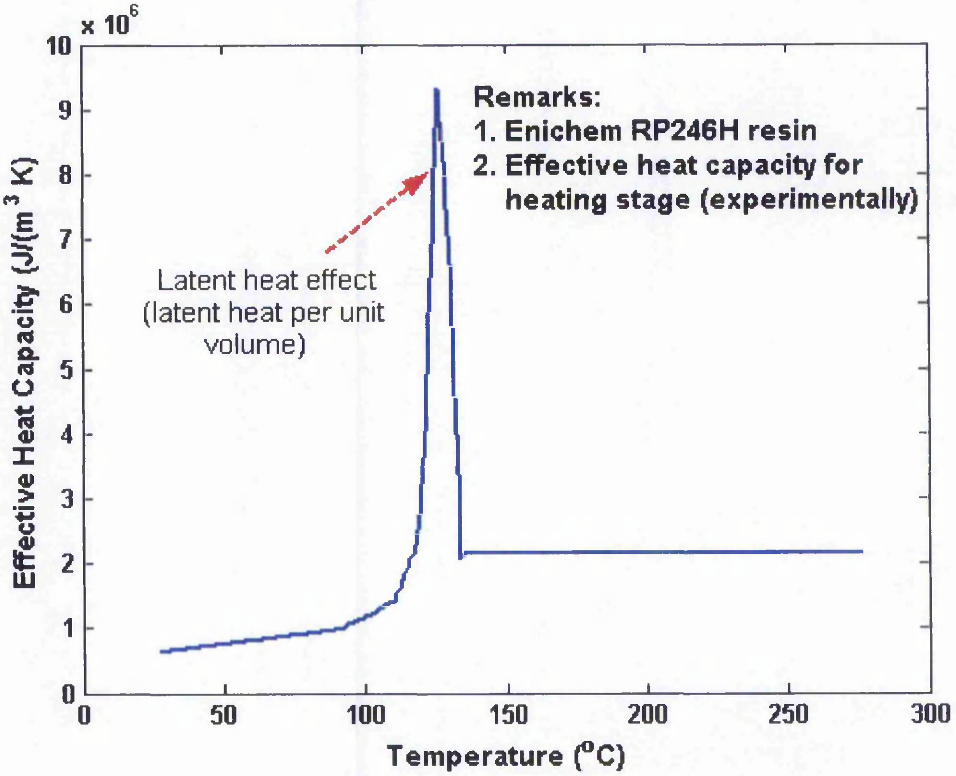

Figure 6-7: Experimental/Analytical type of effective polymer heat capacity for heating process [56]

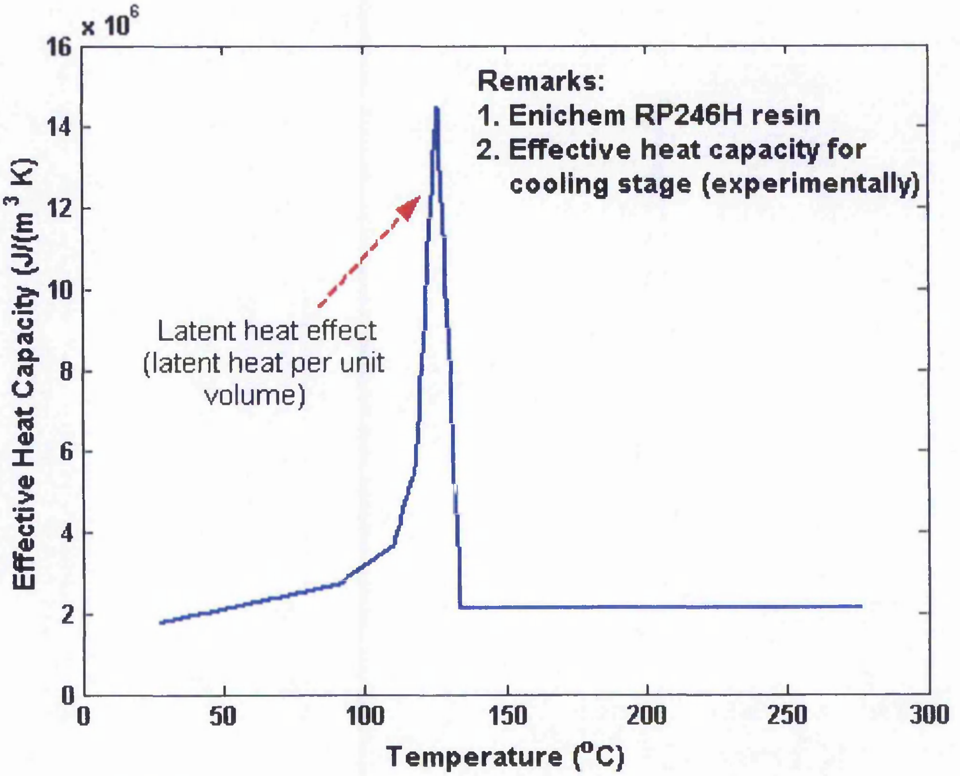

Figure 6-8: Experimental/Analytical type of effective polymer heat capacity for cooling process [56]

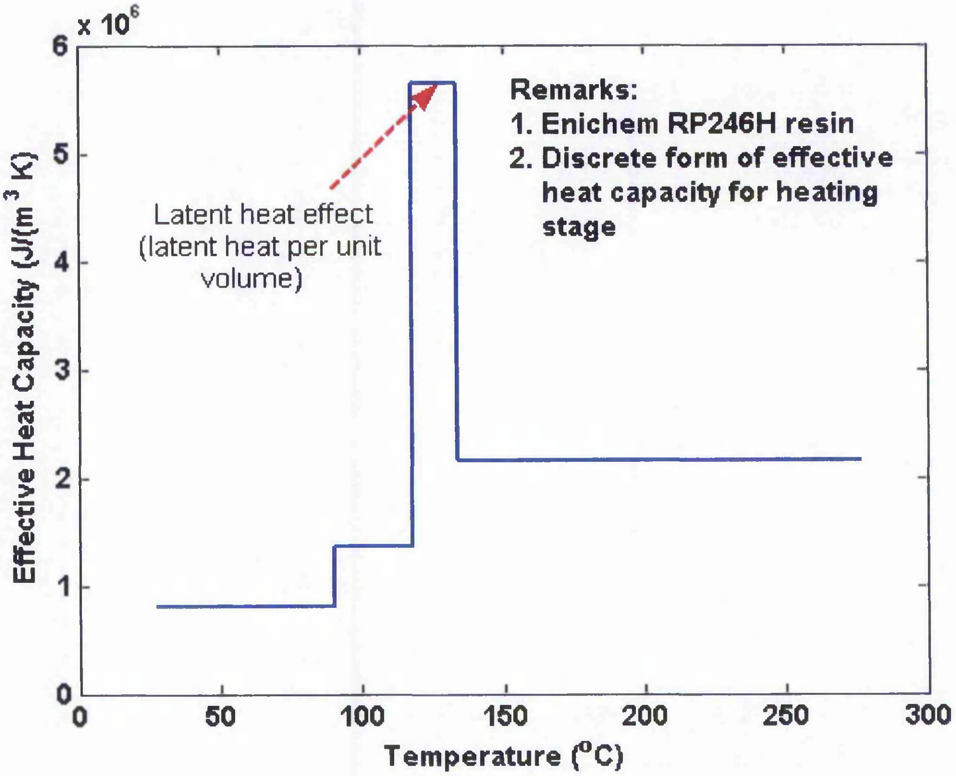

Figure 6-9: Discrete type of effective polymer heat capacity for heating process

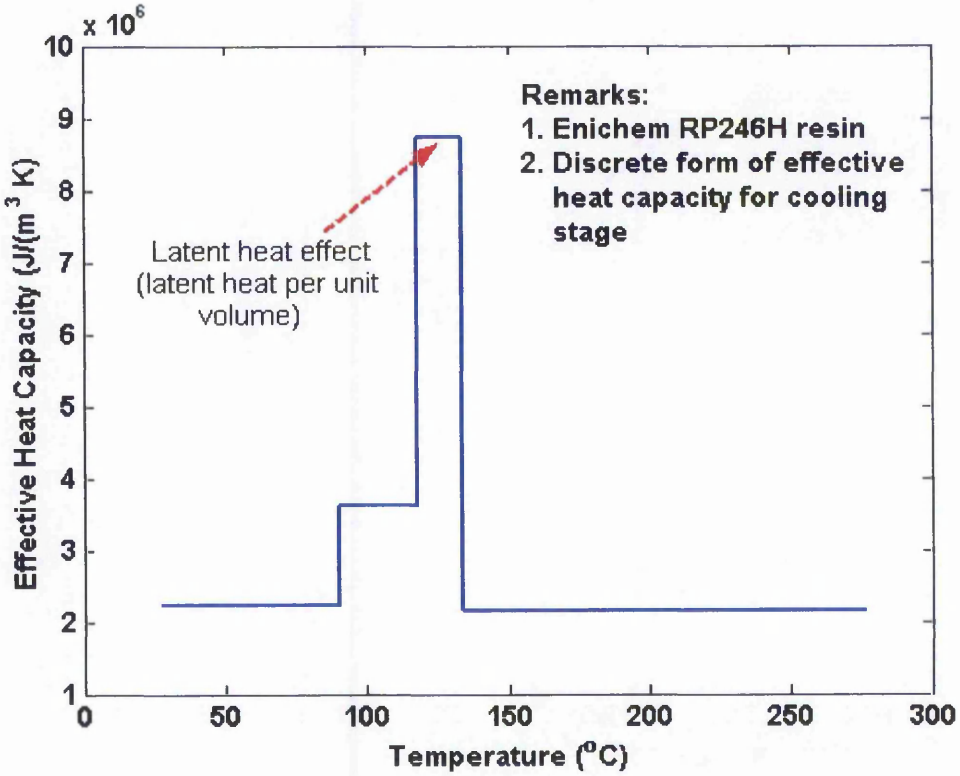

Figure 6-10: Discrete type of effective polymer heat capacity for cooling process

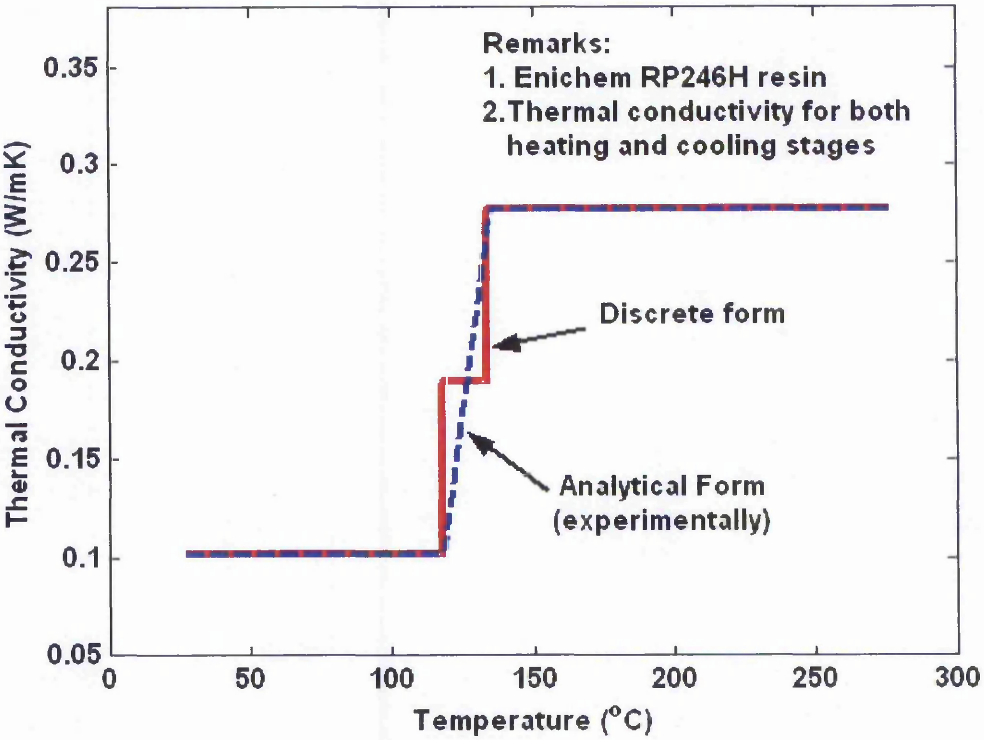

Figure 6-11: Experimental [56] and discrete types of effective polymer thermal conductivity for heating and cooling processes

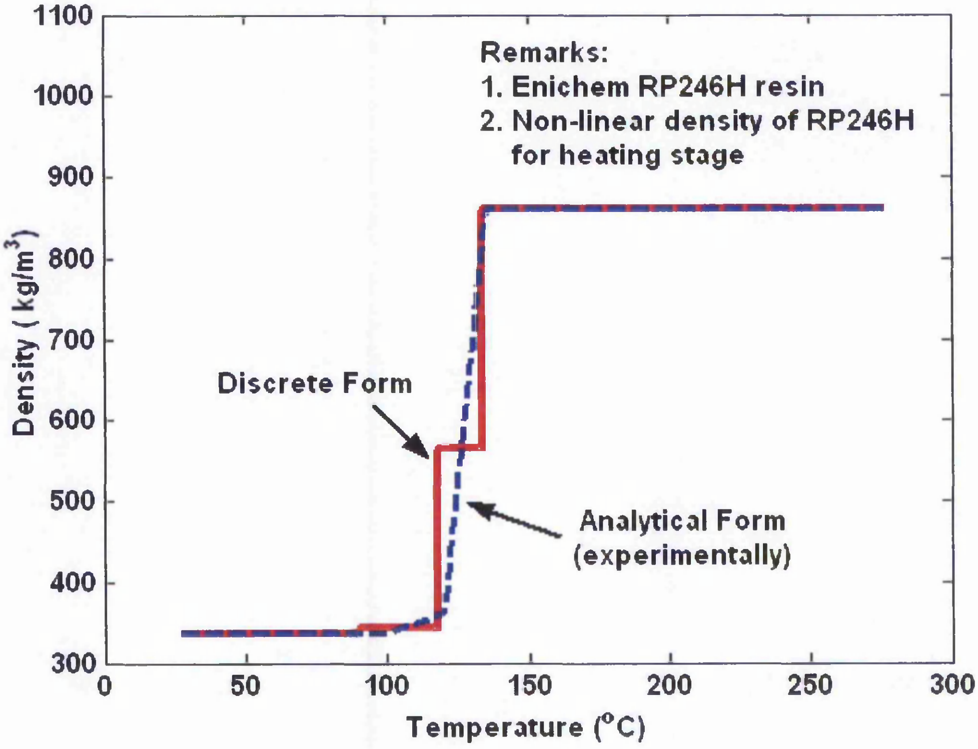

Figure 6-12: Experimental [56] and discrete types of effective polymer density for heating process

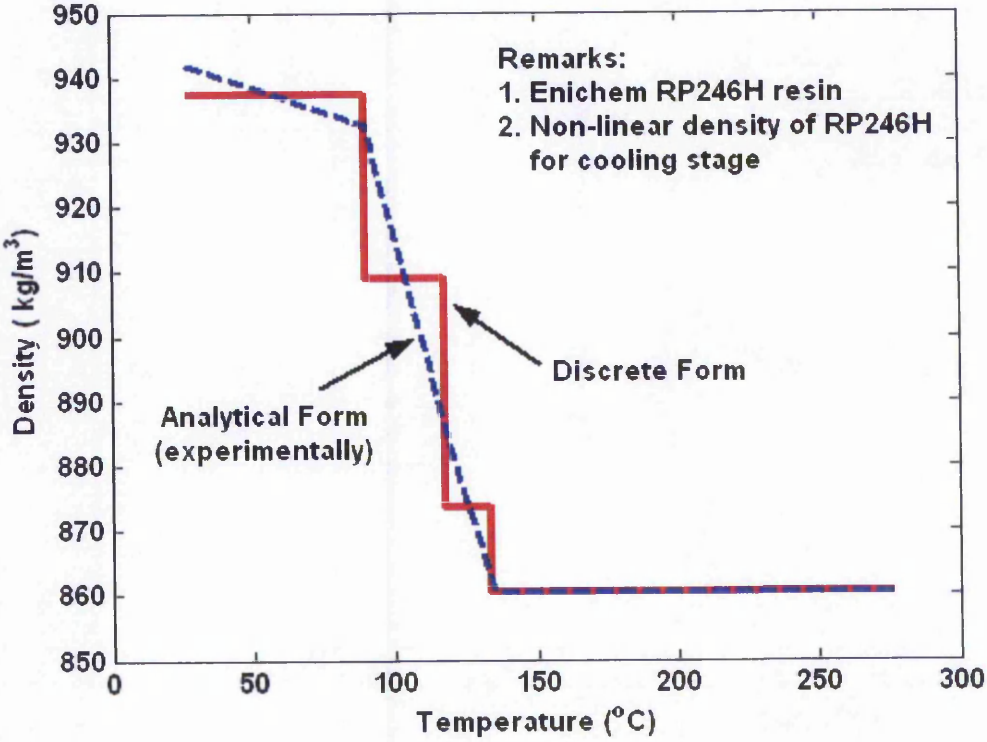

Figure 6-13: Experimental [56] and discrete types of effective polymer density for cooling process

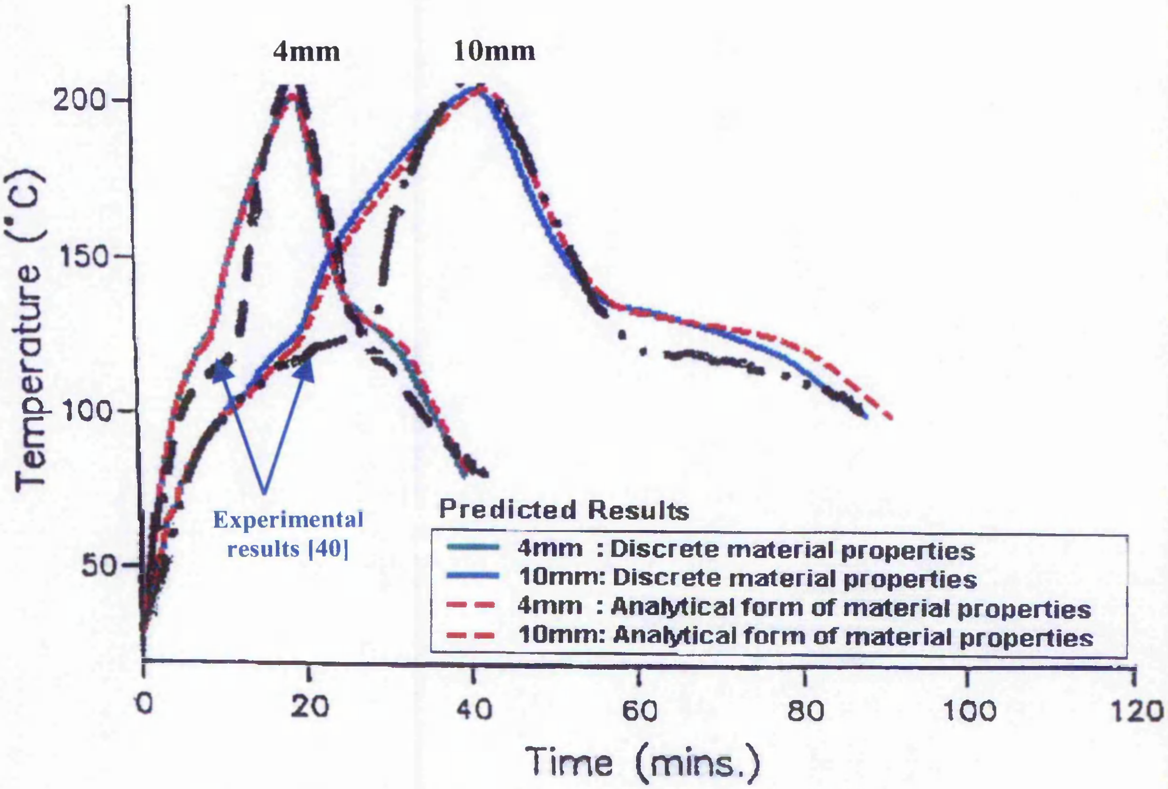

Figure 6-14: Comparisons of phase change algorithms

range, to obtain the latent heat of fusion from the area underneath its corresponding analytical functions given in Liang [56] such as Figure 6-7. Thus the overall latent heat is still preserved by these discrete data, and the accuracy of the proposed *efficient algorithm* (Hsiao's method) for the phase change, *cf.* Chapter 5, can be justified.

Figure 6-14 compares the results of the time-temperature profiles of simulations using either the *efficient algorithm* or a simple *averaging method* (refer to Section 3.2.3.2 (v)) for the phase change with the measured values. Here, the analytical form of the polymer thermal properties is used for the averaging method. For a $4\,mm$ thin part, both methods have similar predicted air temperatures, which are close to the experimental plot. A small deviation between the predictions of the methods is apparent during the cooling cycle for a $10\,mm$ thick part. This discrepancy arises from the averaging method overestimating the liberation of latent heat in the solidifying zone. The efficient algorithm gives better phase change predictions as well as simplifying the input data and decreasing the computational non-linearity. Thus the iterative solutions are confined only to the phase change regions. Furthermore, the satisfactory predictions by the efficient algorithm have confirmed the validity of the discrete data in Table 6-2, to represent its analytical functions [56]. As a whole, the reliability of the proposed phase change algorithm has been verified.

A study to achieve a high degree of computational optimisation for the modelling is outside the scope of this research. However, the efficient algorithm manages to reduce the computational cost by roughly 18–23% in the heating cycle and 15–20% in the cooling cycle. The total computational saving would be significant when parametric simulations are performed. The results of the above studies have led to the *efficient* *algorithm* being implemented for the reminder of the research.

6.4 Internal Air Temperature: Model Verification and Indication of the Six Major Processing Stages

Nugent experimentally found that the internal air temperature could be used to identify the heating and cooling times and the six major stages in a complete rotational moulding cycle; powder heating, melting, further heating, liquid cooling, crystallizing and further solidifying [14]. From the modelling viewpoint, the practicability of a rotomoulding model must be judged from these two conditions. Here, the differences between the physical and numerical representations of six major stages for semi-crystalline polymers inside a rotomoulded cavity are shown in Table 6-3.

Process	Temperature profile of internal air					
	Heating			Cooling		
Rotational moulding process	Stage 1	Stage 2	Stage 3	Stage 4	Stage 5	Stage 6
Physical stages of polymer	Free powder	Free powder + Molten polymer	Melted polymer	Melted polymer	Molten polymer + Solid polymer	Solid polymer
Numerical stages of polymer (Slip flow model)	Mixing bed + Stagnant bed	Mixing bed + Stagnant bed	Stagnant bed	Stagnant bed	Stagnant bed	Stagnant bed
Figure 6-24	Curve A-B	Curve B-C	Curve C-D	Curves D-E & E-F	Curve F-G	Curve G-H

Table 6-3: Physical and numerical representations of semi-crystalline polymers in rotational moulding process

For a 2.7 *mm* plastic part, Figure 6-15 and Figure 6-16 show the comparisons of the mould surface temperatures and the internal air temperatures, respectively. As shown in Figure 6-15, the satisfactory prediction of the mould surface temperature has verified the RotoFEM program. In addition, the capability of the predicted internal air temperature identifies the two important conditions mentioned above is also being demonstrated in Figure 6-16. For example, the experimental internal air temperature

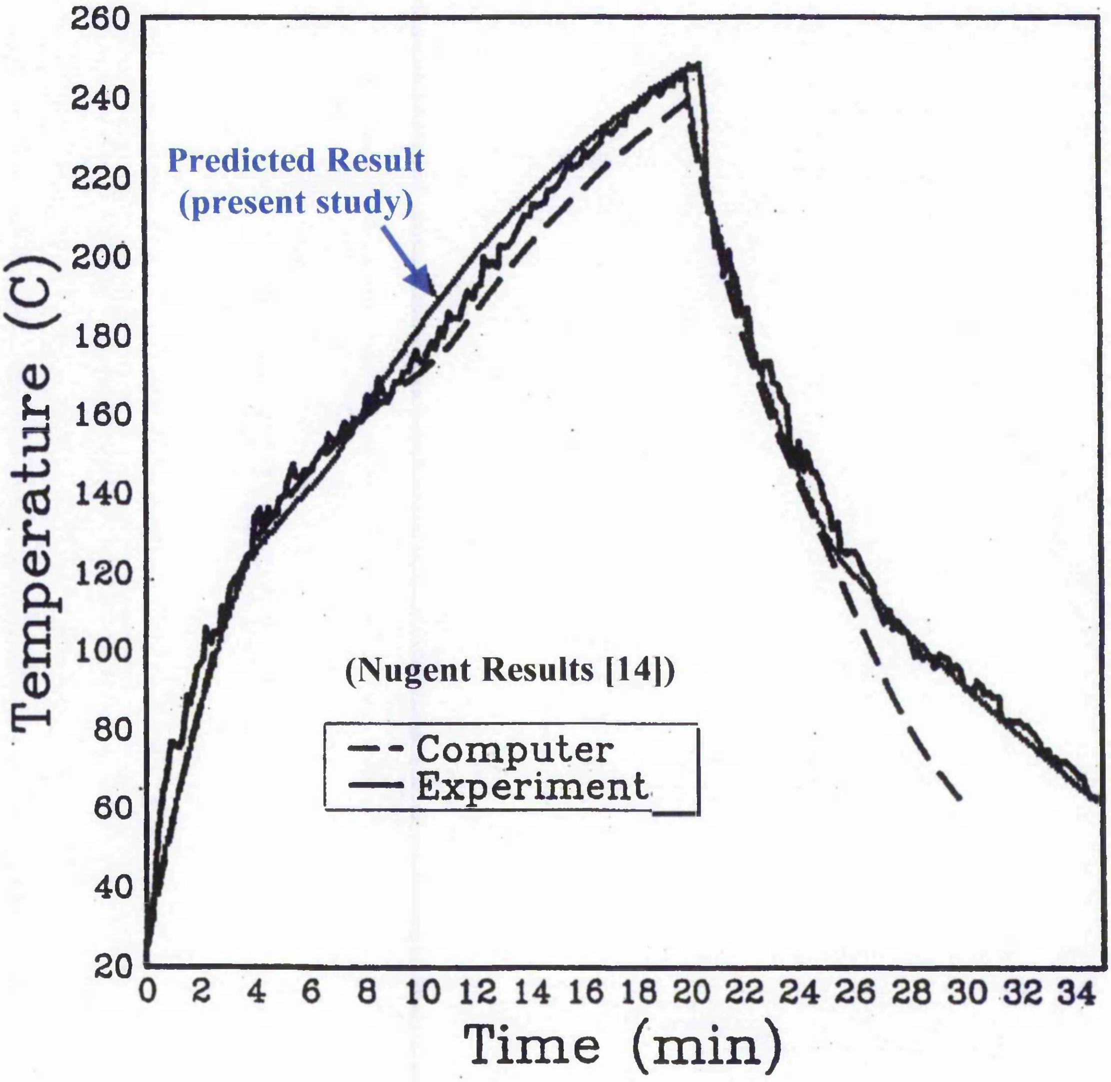

Figure 6-15: Comparison between experimental and predicted external wall temperatures (RP246H – 2.7 mm plastic part – steel mould – 300 ^0C oven)

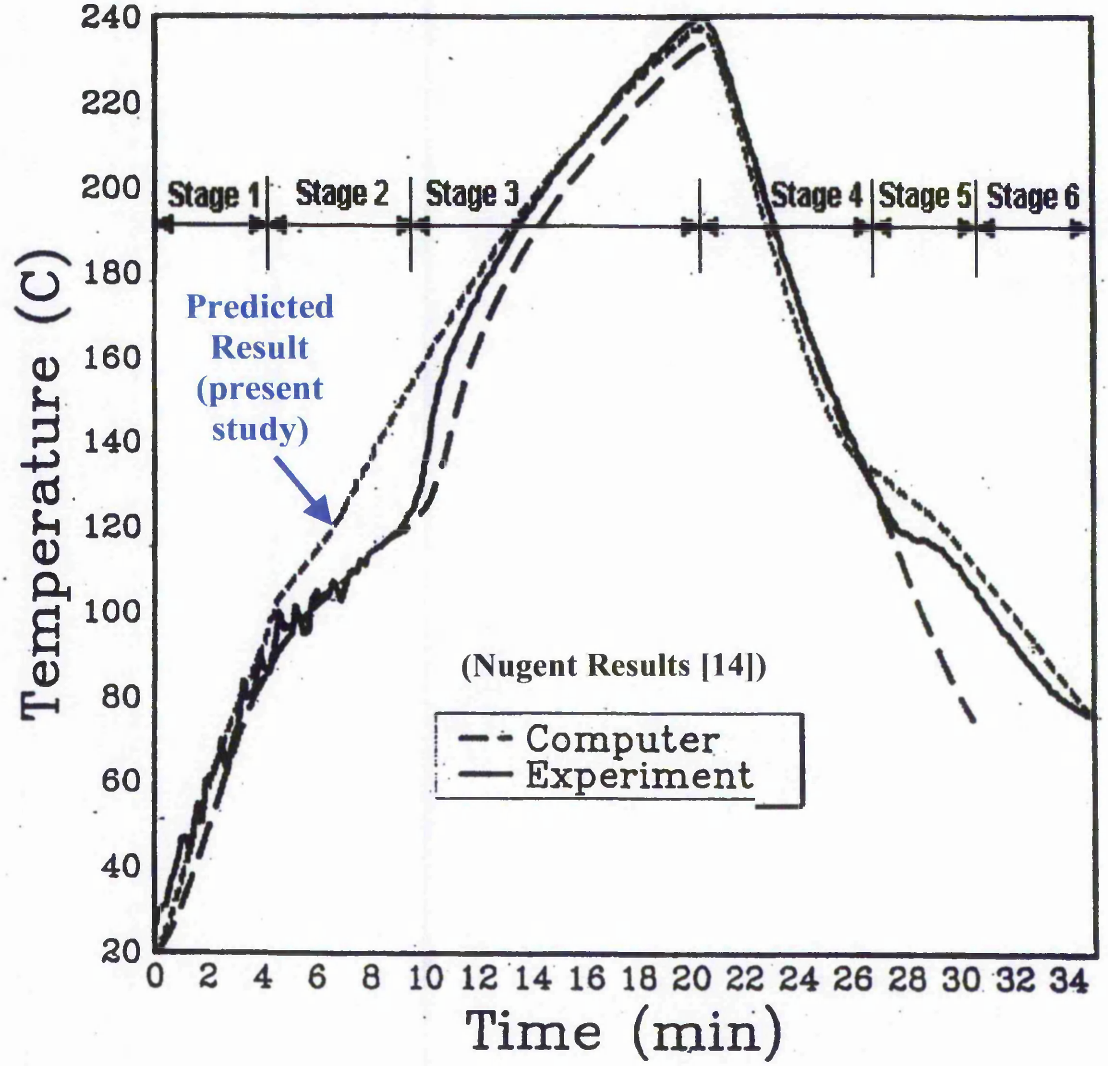

Figure 6-16: Comparison between experimental and predicted internal air temperatures (RP246H – 2.7 mm plastic part – steel mould – 300 ^0C oven)

from Nugent [14] is generally well predicted except in *Stage 2* and *Stage 5*. Based on the satisfactory results in Figure 6-15, the deviations of the internal air temperature in Figure 6-16 are clearly due to the complexity of the rotational moulding process.

6.5 Numerical Simulations of Slip Flow Models

The capability and accuracy of many rotational moulding models are often limited by the part thickness due to the complex heating cycle. To find the modelling limitations for these slip flow models, the square plastic parts are modelled and compared with the available experimental results for parts up to 12 mm thick [11]. The essential plastic information and processing conditions for the modelling are abstracted from Liang [11], as displayed in Table 6-4 herein. The oven temperature used by Liang was not clear. An oven temperature of 290 ^{o}C has been selected since it is the approximate mean value for most the experiments in Liang's thesis [11]. The external heat transfer coefficients are assumed to be similar to those in Table 6-1 (both sources for comparisons were from Queen's University, Belfast – i.e. the same moulding machine). The compared data taken from Liang's thesis [11] was scanned electronically prior to poor printing, which

Material	Polymer RP246H (From *Table 5-7* in Liang [11])					
Thickness (mm)	2	4	6	8	10	12
Shot weight (kg)	1.07	2.11	3.12	4.10	5.06	5.99
Initial internal air temperature (^{o}C)	27.48	28.06	26.89	36.83	30.40	23.97
Time to powder end (mins)	7.80	12.60	16.80	24.00	29.33	34.73
Time to 200 ^{o}C (mins.)	12.20	18.01	23.52	30.37	37.95	45.03
Oven time (mins.)	12.53	18.66	25.26	32.06	38.40	49.26
Cycle time (mins.)	26.53	41.93	66.93	89.93	87.20	117.13
Approximate mean oven temperature (^{o}C)	290	290	290	290	290	290
	Remark: Approximate mean value of oven temperature for most experiments in [11]					

Table 6-4: Experimental process conditions and results for various rotomoulded parts [11] (Enichem RP246H polymer)

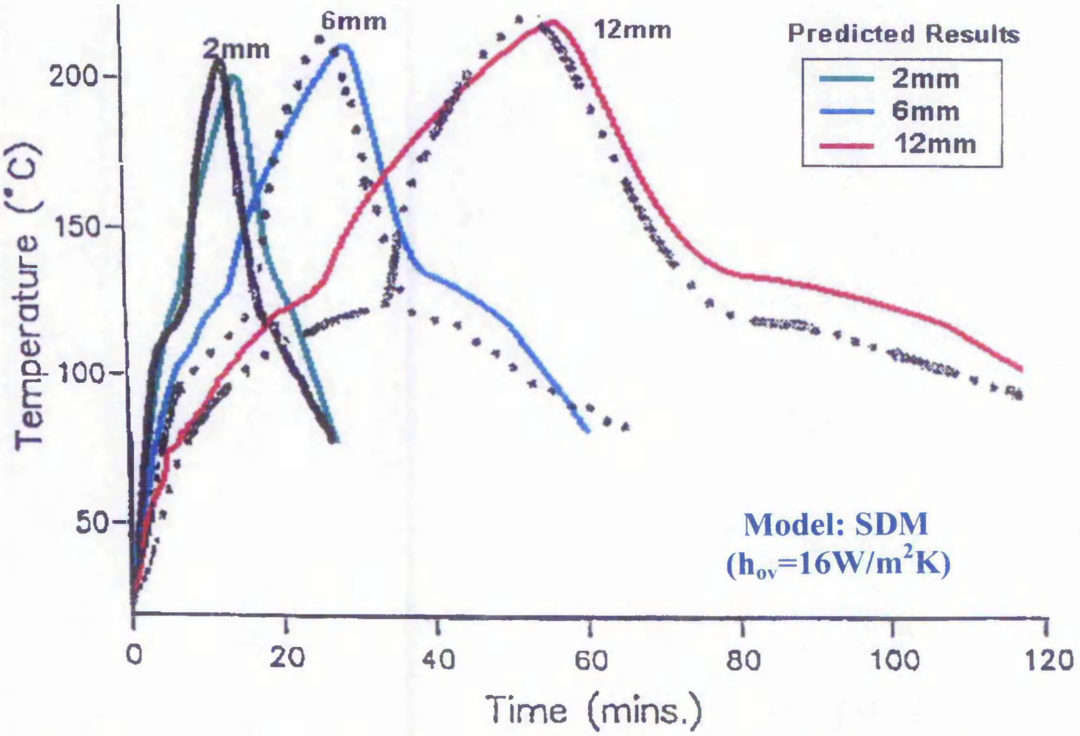

Figure 6-17: Comparisons between experimental [11] and predicted internal air temperatures of 2, 6 and 12 mm parts using SDM model (constant h_{ov})

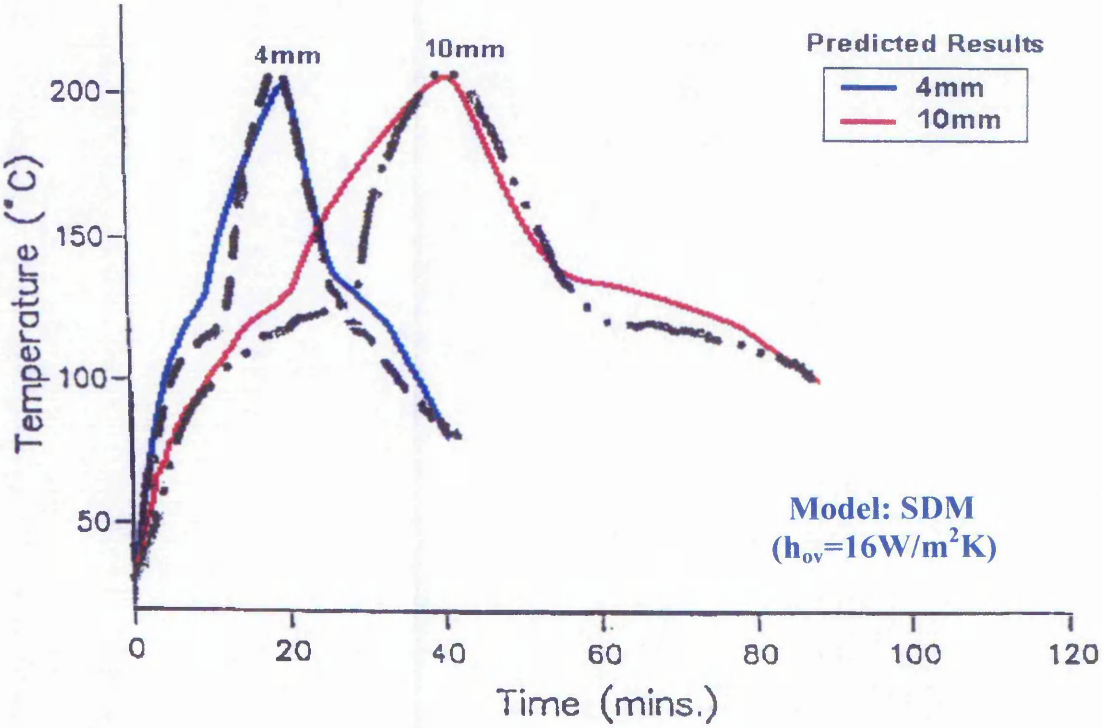

Figure 6-18: Comparisons between experimental [11] and predicted internal air temperatures of 4 and 10 mm parts using SDM model (constant h_{ov})

resulted in a slightly distortion and tilt (a deviation of 2.5^0–3.0^0). Instead of shifting and adjusting the plots, the best-fit x-axis of the figure is chosen as a datum line to standardize the comparisons. This will directly affect the assessments. For example, a relatively thin $2\,mm$ part in Figure 6-17 shows a poorly predicted temperature profile of the internal air compared to the $2.7\,mm$ part in Figure 6-16.

6.5.1 Results of Single-layer Deposition Method (SDM)

A constant value of h_{ov} ($16\,W/m^2K$) is used for this SDM modelling. Figures 6-17 and 6-18 show that the internal air temperatures resemble the experimental results in Liang [11]. However, poor predictions for the melting phase of *Stage 2* of the internal air temperature profiles are generally observed from Figures 6-17 and 6-18. According to the figures, the SDM model predicts a relatively earlier, shorter and less obvious phase change plateau at *Stage 2* compared to the experimental results. It is suspected that this is due to the simple thermal description of the internal air modelling in the SDM model. This is because the assumption of the 'single-layer deposition' considers that the process of plastic deposition takes place between the mixing bed and inner mould surface only. Thus the internal air heated up by the molten plastic will not be considered. At *Stage 3*, better predictions of the internal air temperatures are observed in particular when the air temperature approaches $200\,^0C$. This is because of the similarity between the experimental and numerical models.

6.5.2 Results of Multi-layer Deposition Method (MDM)

A MDM model is proposed to allow additional thermal interactions between the internal air and its surrounding media. Figure 6-19 and Figure 6-20 show the comparisons

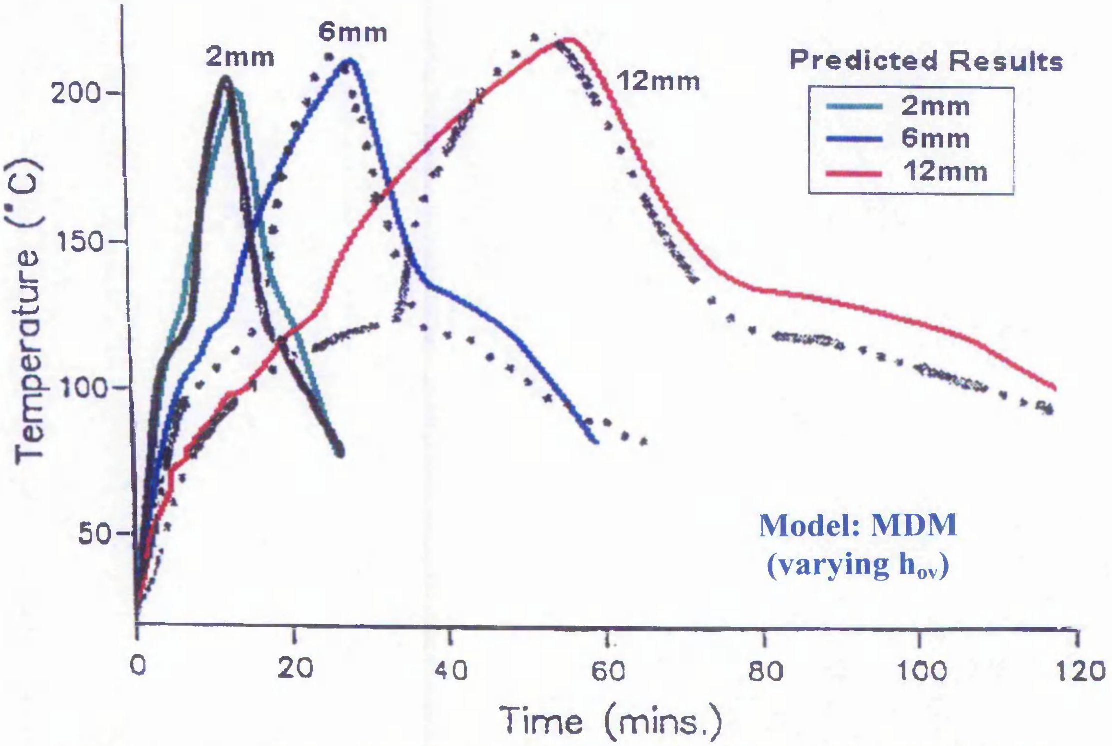

Figure 6-19: Comparisons between experimental [11] and predicted internal air temperatures of 2, 6 and 12 mm parts using MDM model (varying h_{ov})

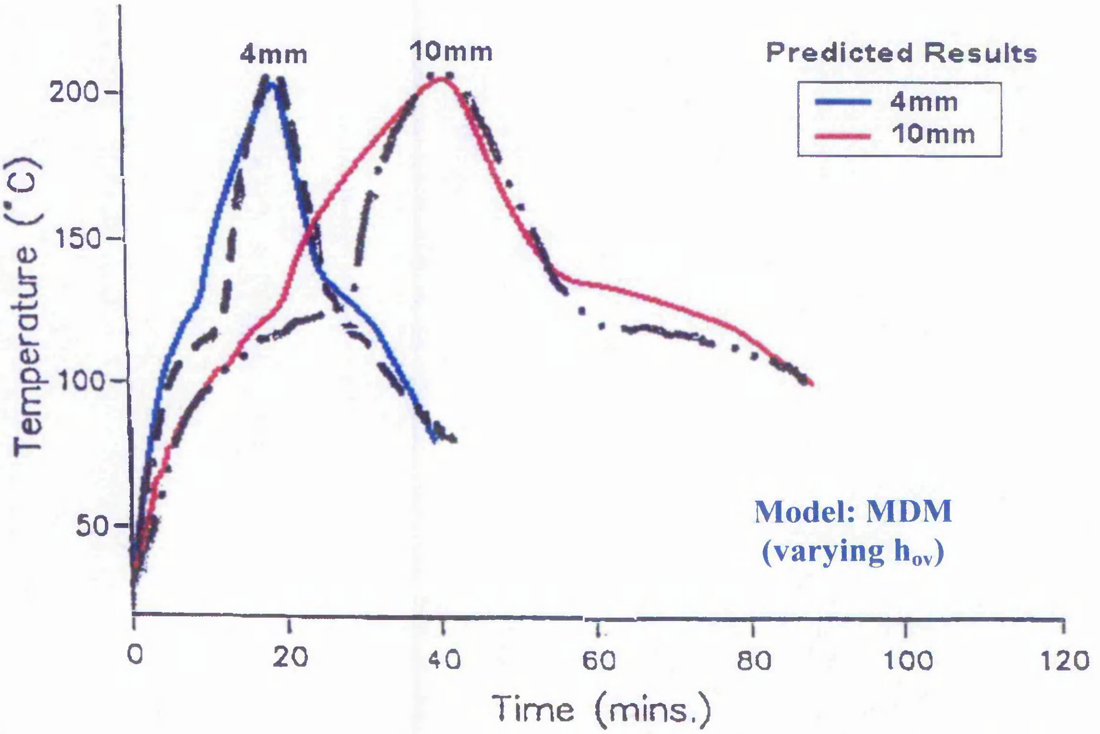

Figure 6-20: Comparisons between experimental [11] and predicted internal air temperatures of 4 and 10 mm parts using MDM model (varying h_{ov})

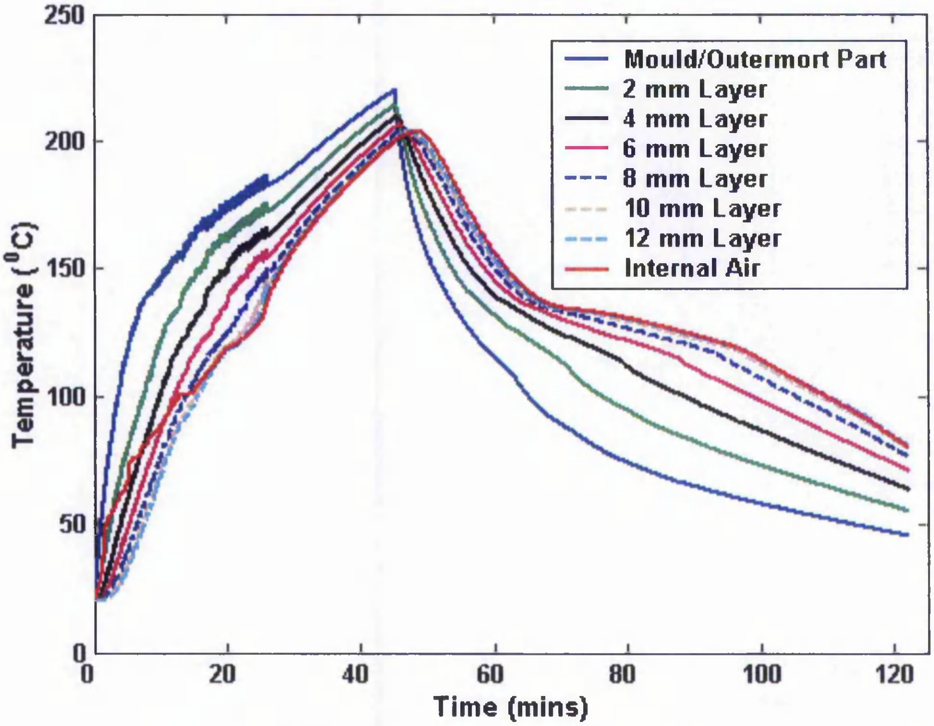

Figure 6-21: Predicted temperature profiles of the internal air and various points across a $12\,mm$ plastic bed using MDM model

between the predicted and experimental temperature profiles of the internal air across a range of part thicknesses. Compared with the SDM model, the results demonstrate that the MDM model is better at predicting the temperature profiles of internal air, which are closer to Liang experimental results [11]. However, the predicted air temperatures still fail to match the melting phase of *Stage 2*. This indicates that this MDM model still does not effectively block the 'additional' energy transfer from the mould to the mixing bed and consequently to the internal air.

By studying the correlation curves of a $12\,mm$ part, as shown in Figure 6-19, Figure 6-21 shows that this slip flow model begins to be less stable. In fact, a similar problem is found for the SDM model. The less smooth predicted air profile shows few 'kinks' at

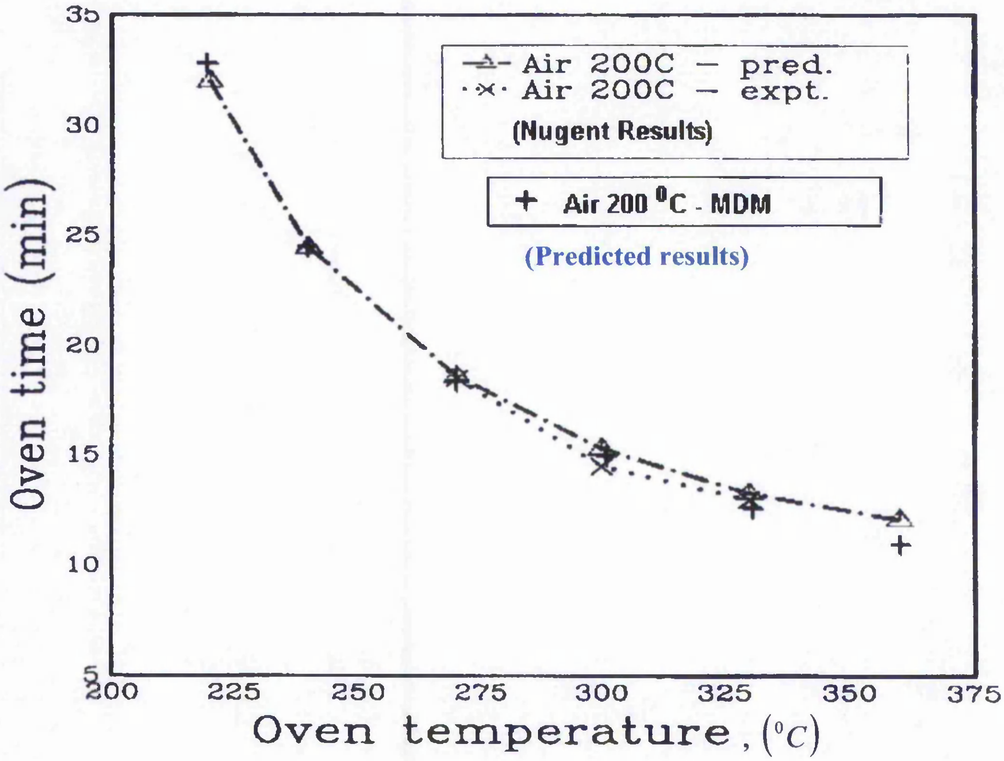

Figure 6-22: Comparisons of oven times over a range of oven temperatures for 2.7 mm part using MDM model [14]

Stage 1 and *Stage 2*. This does not happen in the 8 mm part in Figure 6-24. Thus the existing slip flow methodology could predict good results for a part thickness up to 12 mm. Further studies on the relation between the slave and master elements of the FEM for the mixing bed and the thermal interactive fraction of the internal air, ν, are still required.

The ranges of h_{ov} in Table 6-1 used in the MDM model could possibly be tightened if a better comparison were carried out. The proposed methodology of varying h_{ov} is applicable in the dynamic rotomoulding system in particular when a high degree of accuracy is required and a narrow range of h_{ov} is used. Figure 6-22 shows the influence of the oven temperatures on the oven (heating) times. The predictions correlate well with the experimental data [14].

6.6 Achievements of Slip Flow Models

6.6.1 Model Simplifications for Rotational Moulding Modelling

The SDM and MDM types of the 2-D slip flow model describe *Stage 1* and *Stage 2* of rotational moulding process without the need to track the powder pool location and to consider the powder mass inside the mould. Both models can predict a satisfactory internal air temperature during the heating of tumbling powder in *Stage 1*. In fact, *Stage 1* is the most difficult stage to model particularly in multi-dimensional models. This is because the numerical consideration of complex thermal interaction between the internal air and surrounding media is required. In fact, the success or failure of the predicted internal air temperature profile depends on the thermal interaction being accounted for in *Stage 1*. In the case of a $12\,mm$ thick part in Figure 6-19, *Stage 1* is well predicted for approximately the first 20 minutes of the rotational moulding cycle. This implies that the slip flow methodology can simulate the heat transfer inside the mould even without the involvement of the changeable powder mass and the powder motion. These simplifications have significantly reduced the numerical procedures and efforts for the modelling of the rotational moulding process.

The predicted results of a $8\,mm$ thick part for the SDM model and MDM model, respectively, are given in Figures 6-23 and 6-24. Figure 6-23 shows a relatively obvious ‘kink’ at the mould temperature profile during the onset of *Stage 3*. This ‘kink’ does not appear in the MDM prediction (Figure 6-24). The potentially improvable MDM model has been selected for the rest of the study on the basis of the above results.

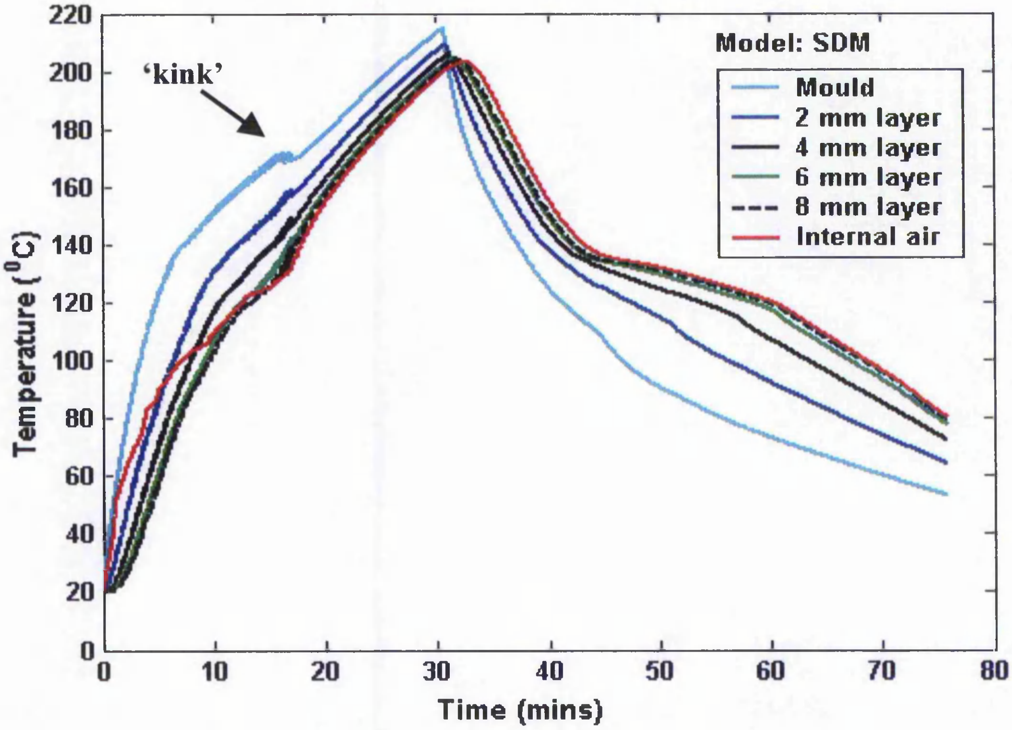

Figure 6-23: Predicted temperature profiles of the internal air and the 8 mm plastic bed at various points using SDM model

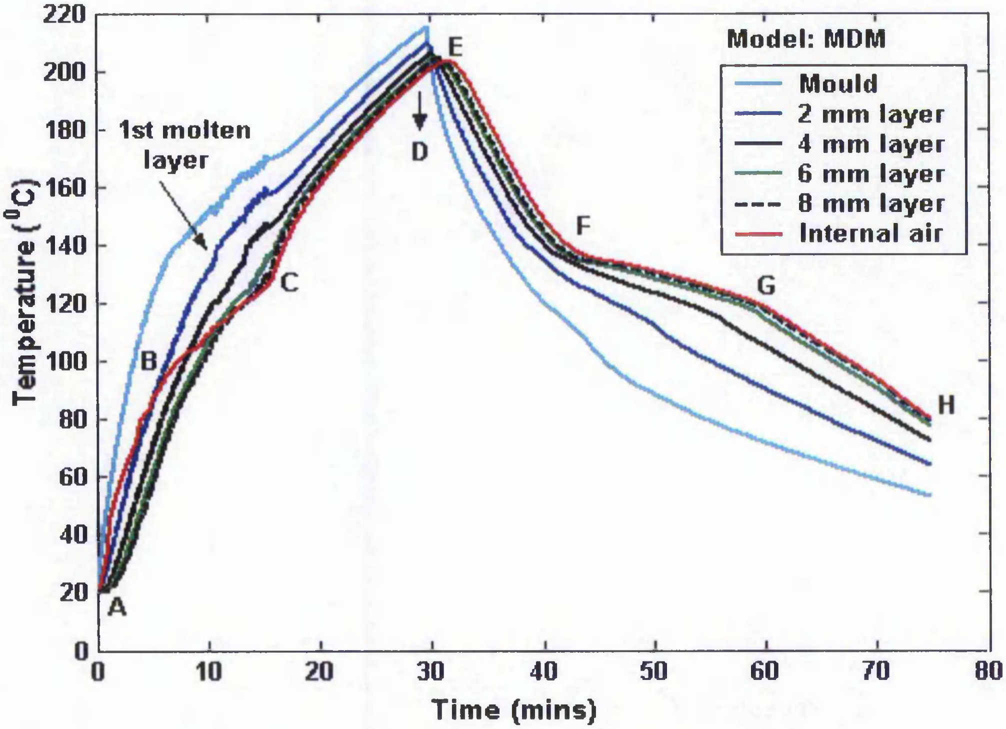

Figure 6-24: Predicted temperature profiles of the internal air and the 8 mm plastic bed at various points using MDM model

6.6.2 Prediction of Six Major Stages in a Rotational Moulding Cycle

The graphs of Figure 6-24 show the predicted temperature profiles of the mould, powder pool and internal air during a complete rotomoulding processing cycle. Generally, the internal air temperature profile does indicate the six major processing stages of the rotational moulding process (also refer to Table 6-3). The curve A-B shows that the internal air temperature is higher than most of the powder layers but lower than the mould temperature during the earliest period of the heating cycle. This is because the internal air is mostly heated up by the mould rather than by the plastic. The plastic temperatures gradually exceed the internal air after a short time the melting plateau of the air profile occurs. The prediction demonstrates the actual internal air profile of rotational moulding process such as Figure 2-2.

The temperature of the internal air profile (Figure 6-24) reaches a plateau before the first molten plastic layer fully covers the inner mould surface. This implies that the onset of the air plateau contributes to the latent heat absorbed by the polymer during the melting process, instead of signifying the appearance of the first molten layer (i.e. heat-up rate of internal air slows down). The plateau ends at point C when the melting process is complete, which will be accompanied by the formation of a monolithic plastic bed. A rapid raise of the internal air temperature is observed along the curve C-D to the *deheating temperature* of $200\ ^0C$. The temperature indicates that the optimum impact strength of most rotomoulded polymers, for example polyethylene, has been achieved. It is indeed at the internal air temperature between $200 \pm 5\ ^0C$ [14,93]. *Stage 3* helps to consolidate and to dissolve the trapped gas bubbles inside the molten part [11]. In the slip flow model, the polymer is assumed to achieve its melting temperature before the polymer 'deposition' onto the mould begins. This is a compensation balance to the pre-arranged slip flow beds as earlier mentioned. In practice, the polymer becomes sticking before the melting temperature, in which an intermittent or a permanent layer of the molten polymer may exist.

As shown in curve D-E, some plastic layers and the internal air inside the mould undergo further heating at the outset of the cooling cycle. This is as a result of the remaining residual heat inside the system. The further heating helps to consolidate the plastic part by removing inherent bubbles inside the part [37]. As delineated in Figure 6-24, a more effective cooling rate occurs between points E to F before reaching the solidifying region F-G. The cooling continues until the molten plastic is fully solidified at point H or the *demoulding temperature.*

6.7 Modelling of Warpage and Internal Cooling Processes

The commonly found types of warpage are concave and convex warpages. In this study, they are modelled as the centre and corner warpages, respectively. The centre warpage is represented by the mould-polymer separations confined at the centre vicinities of the inner mould surfaces and leaving the corner mould surfaces in perfect contact with the polymer. On the other hand, the corner warpage has mould-polymer separations at the corners of the mould. The heat transfer coefficient at the warpage interface, h_{int}, is used to describe the efficiency of heat transfer to and from the air gap by natural convection. After a number of the warpage simulations, this temperature dependent h_{int} was found to have a negligible contribution to the cycle time and internal air temperature profile of the rotational moulding. Consequently, h_{int} is set to a constant for minimizing the computational effort.

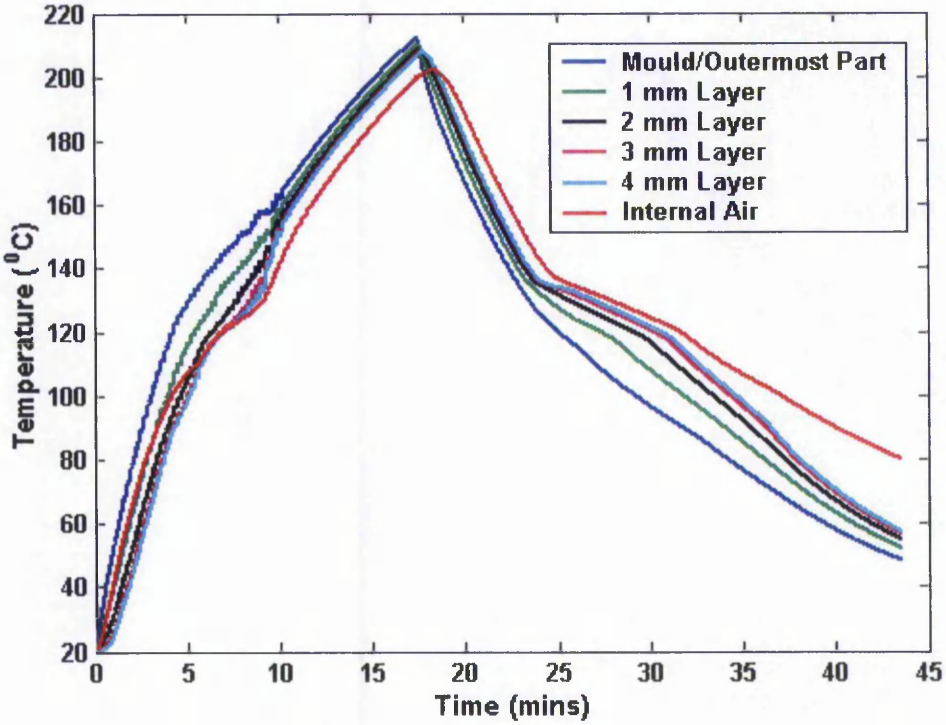

Figure 6-25 (a): Centre warpage - predicted temperature profiles across a 4 mm un-warped region during external cooling process

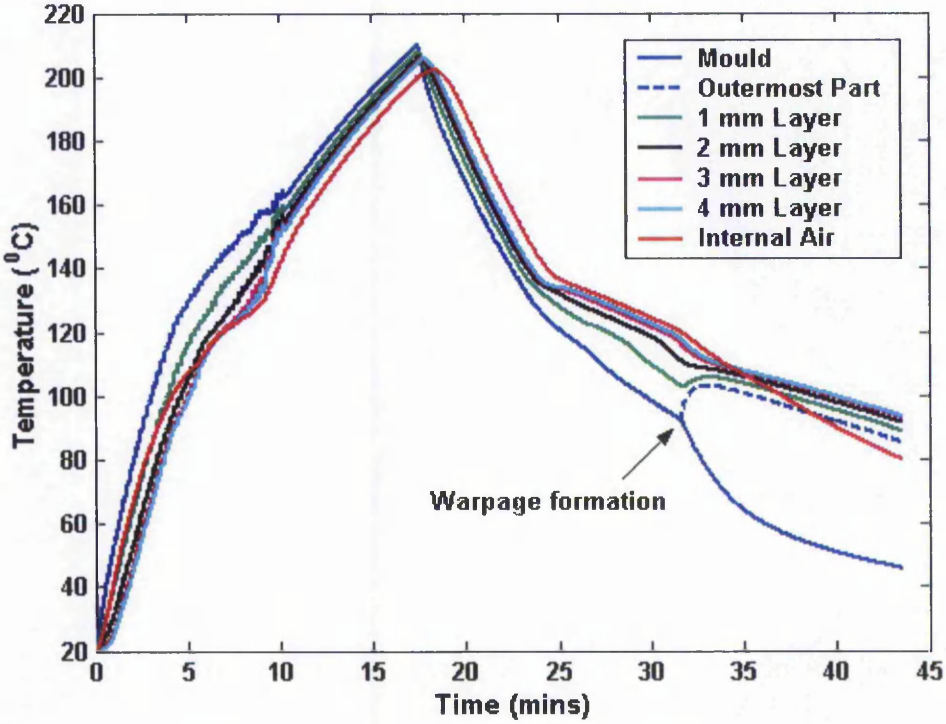

Figure 6-25 (b): Centre warpage - predicted temperature profiles across a 4 mm warped region during external cooling process

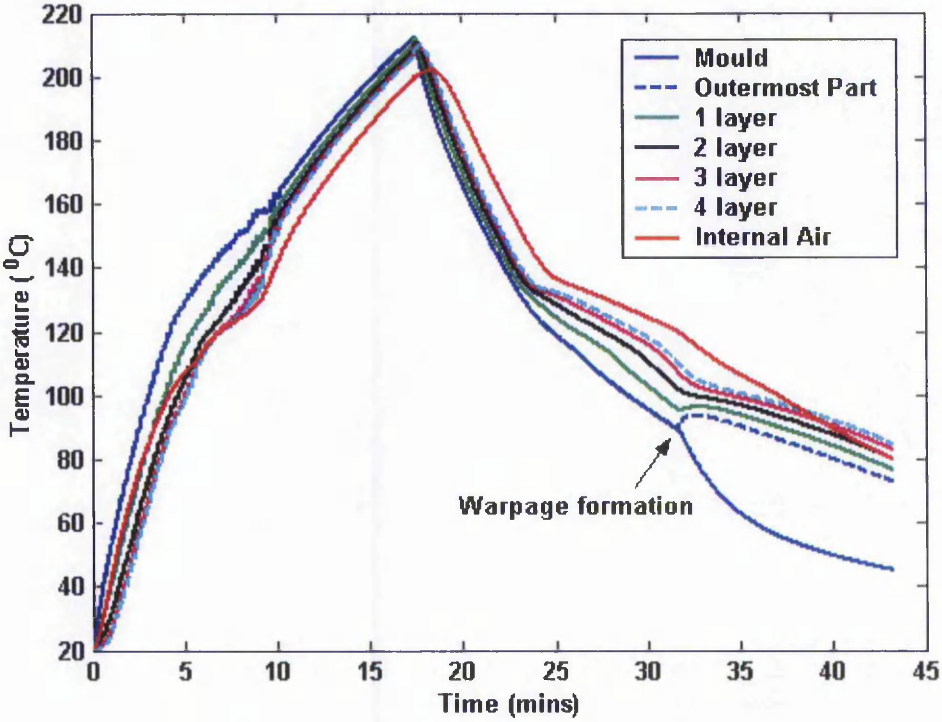

Figure 6-25 (c): Corner warpage - predicted temperature profiles across a 4 mm warped region during external cooling process

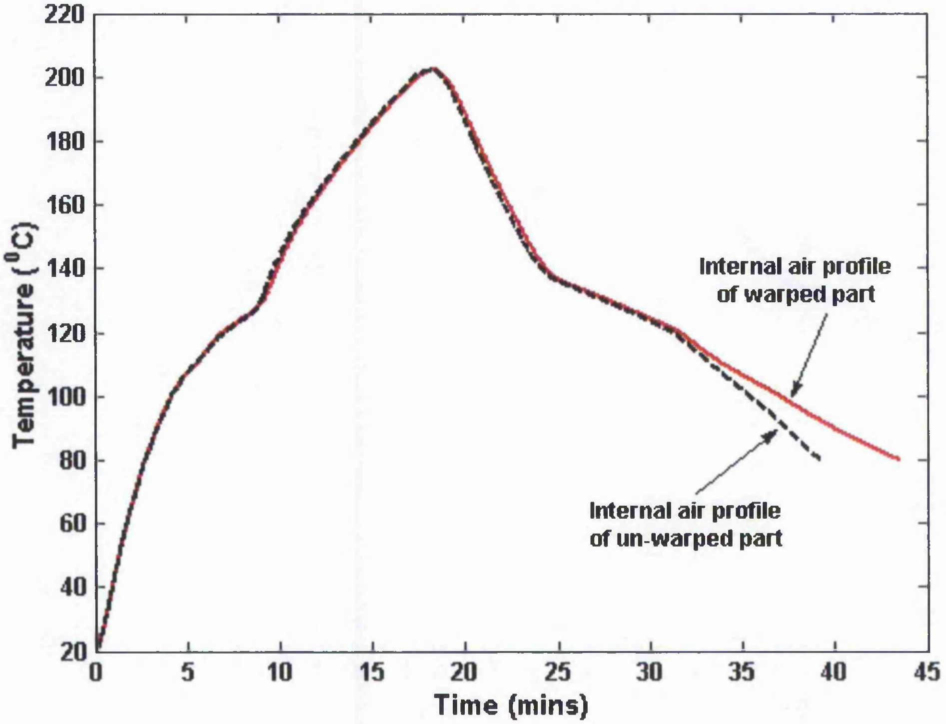

Figure 6-26: Comparison of the internal air temperatures between warped and un-warped 4 mm parts

Figures 6-25 (a) and (b) depict the predicted temperature profiles of a 4 *mm* centre-warped part across the thickness in the un-warped and warped regions, respectively, during the external cooling simulations. The results imply that warpage only modifies locally the shape of the temperature profiles, where the polymer is detached from the mould surface. The warped portions still possess higher temperatures than the internal air, even at the 'common-practice' demoulding air temperature of $80\,^0C$. This means that the warped portions are not fully solidified. This suggests that the internal air temperature of a warped part does not provide an accurate or optimum guideline for the demoulding time, which the part needs to achieve the optimum mechanical properties for the moulding. A simple measure against this is to decrease the demoulding temperature to ensure that the final part is completely solidified. This will, however, add an additional cost to the process, which is undesirable. An alternative option is to apply internal cooling to the mould to reduce the cycle time.

Figure 6-25 (b) or (c) shows that some of the plastic layers close to the mould surface are reheated when warpage occurs. The temperature inversions are because of the air gap (warpage), a poor thermal conductor, has retarded the heat transfer from inside the hot part to the mould through a slow natural convection mechanism. The mould surface does not receive the heat rapidly during the cooling process. The consequence of this is that the mould surface temperature drops relatively faster in cooling. The phenomenon results in a large thermal gradient between the mould and the plastic. In practice, a rapid drop of the mould temperature, Figure 6-25 (b), may not be observed after the moulding has warpage. One of the main reasons is because of the continuous rotating motion of the mould inside an asymmetric cooling environment.

Figure 6-26 shows that the crystallization-induced plateau in the internal air temperature profile is less obvious for the warped part than the un-warped part. This due to the fact that mould-polymer detachment has slowed down the overall cooling rate of the internal air during the one-side external cooling. As a result, there is no dramatic change in the internal air profile even after crystallization is finished. Since warpage is a very common problem in the rotational moulding, the results would suggest that this is a contributing reason why most of the experimental temperature profiles of the internal air usually fail to show a clear cooling plateau, such as Figure 6-19; even though the energy release in the polymer RP246H is greater than the energy absorbed. This adds to the main factors contributing to this phenomenon, they are high cooling rate, over-heated part or deterioration (lower solidification temperature) [49] and the size of a mould.

Detachment of polymer from mould is undesirable since it results in relatively large amounts of shrinkage and low impact strength [59]. As earlier mentioned, the internal cooling is an effective measure to keep cooling times short and reduce the degree of warpage. Figure 6-27 has quantitatively shown that external-internal cooling significantly reduced the cycle times particularly for the moulding of thick products.

Figures 6-28 to 6-33 (not to scale) demonstrate the predicted temperature distributions on the demoulding $12\,mm$ of thick parts under different processing conditions. Generally, the thermal contour plots of the parts help to determine behaviour of the final part and to verify the global errors of the RotoFEM program. Analysing the temperature symmetrization of the final results, for example, does the latter. Figure 6-28 shows that the final product from the external cooling process is hot inside and relatively cool outside. The temperature distribution along each layer in the circumferential direction is

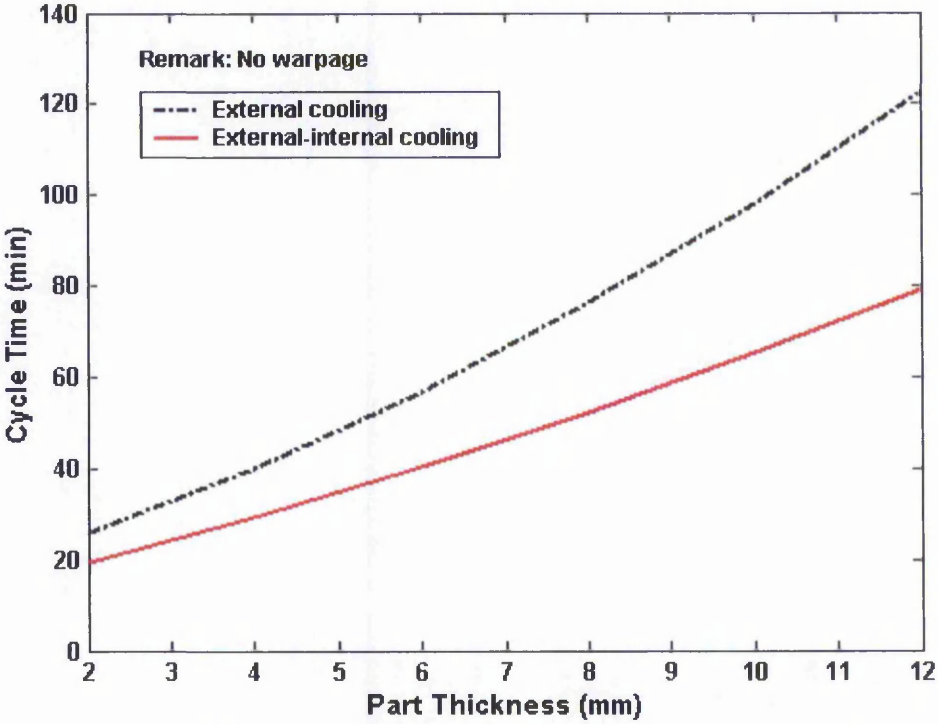

Figure 6-27: Comparisons of cycle times between external cooling and external-internal cooling processes

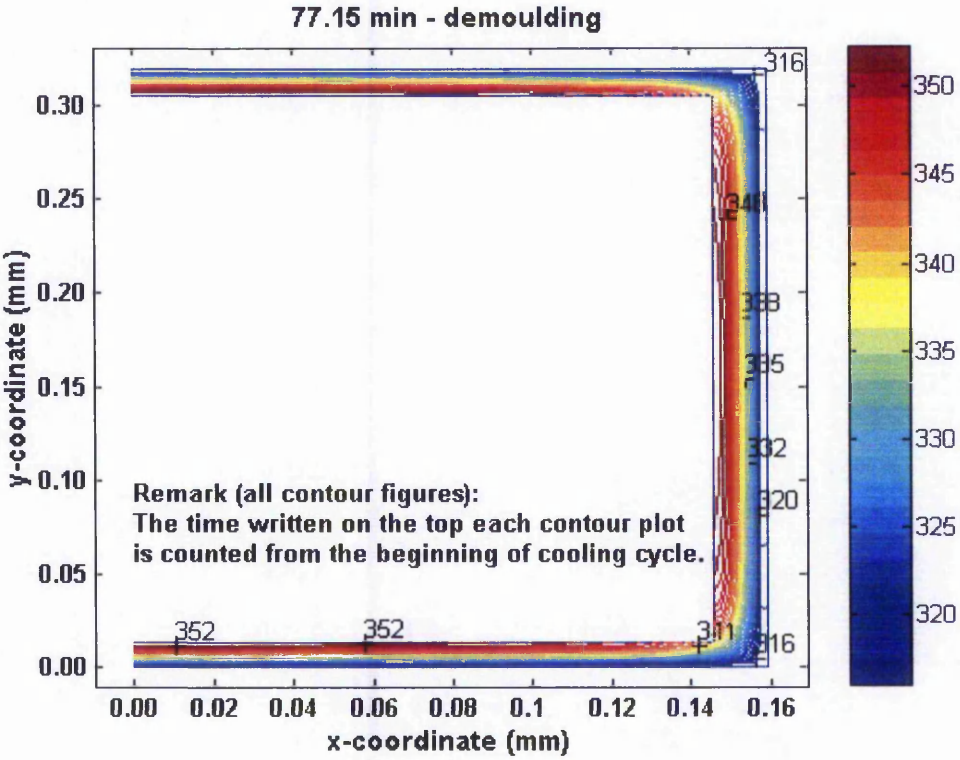
77.15 min - demoulding

Remark (all contour figures):
The time written on the top each contour plot is counted from the beginning of cooling cycle.

Figure 6-28: Demoulding temperatures inside a 12 mm un-warped part for external cooling process almost constant. According to the definitions in Figure 2-14, the external cooling method is expected to produce homogeneous layers inside the final product. However, the contour plot will not identify any anisotropy in the part since the isotropic thermal properties of the polymer are used for the modelling.

Figures 6-29 and 6-30 illustrate the temperature distributions of the final warped parts. The temperatures are clearly varying along the circumferential layer and in the cross-sectional thickness directions in each part. Compared with Figure 6-28, these results indicate that warpage disturbs the heat transfer process and modifies the temperature distribution inside the warped parts significantly. The effect of 2-D heat flow is strong particularly near to the edges of the warped regions. Figures 6-29 and 6-30 also depict that the warpage causes the formation of heterogeneous structural layers. These observations imply that the heat transfer across the detached regions has a magnifying effect on the thermal-dependent properties of the final part. Consequently, the heterogeneity changes the mechanical properties and the behaviour of the end products. In addition, warpage also generates residual stresses inside the warped parts [26]. In practice, the formation of a heterogeneous part is likely to be supported by the facts that warpage generally appears on one side, which causes significant asymmetric cooling in the warped part.

In view of the unsymmetrical nature of the external cooling method and the difficulty in cooling the inside-outside surfaces of the rotomoulded parts at the same rate for the external-internal cooling, there is no cooling method of producing a part without warpage by rotational moulding. An appropriate external-internal forced cooling, is still a diagnostic tool to improve the cooling rate and minimize warpage. Figures 6-31 to

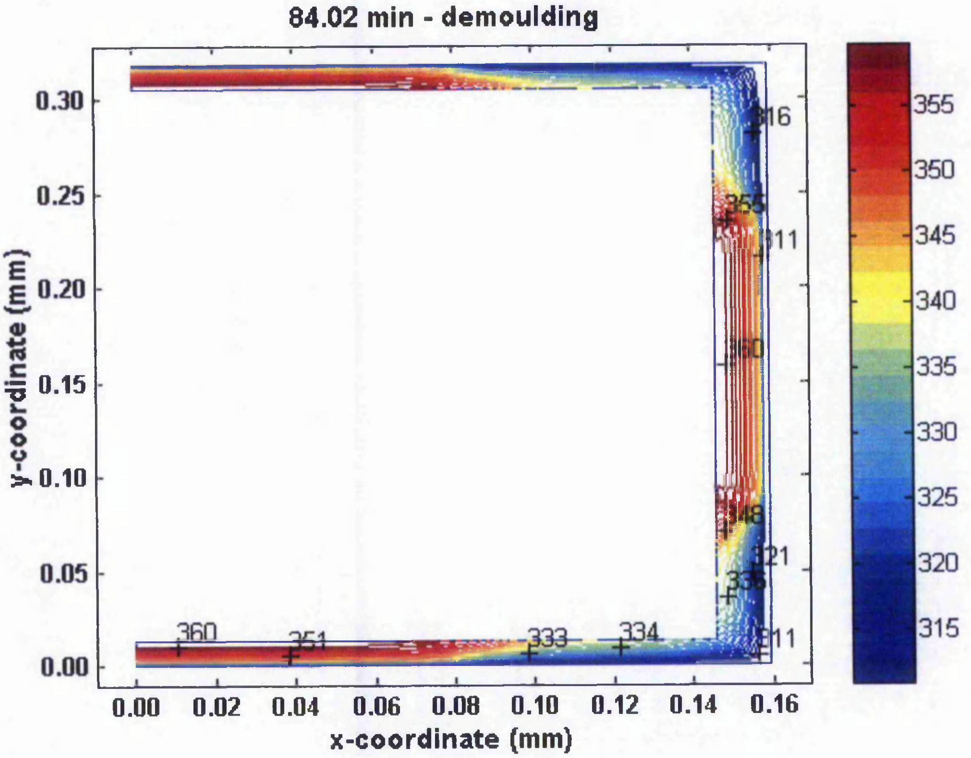

Figure 6-29: Demoulding temperatures inside a 12 mm centre-warped part for external cooling process

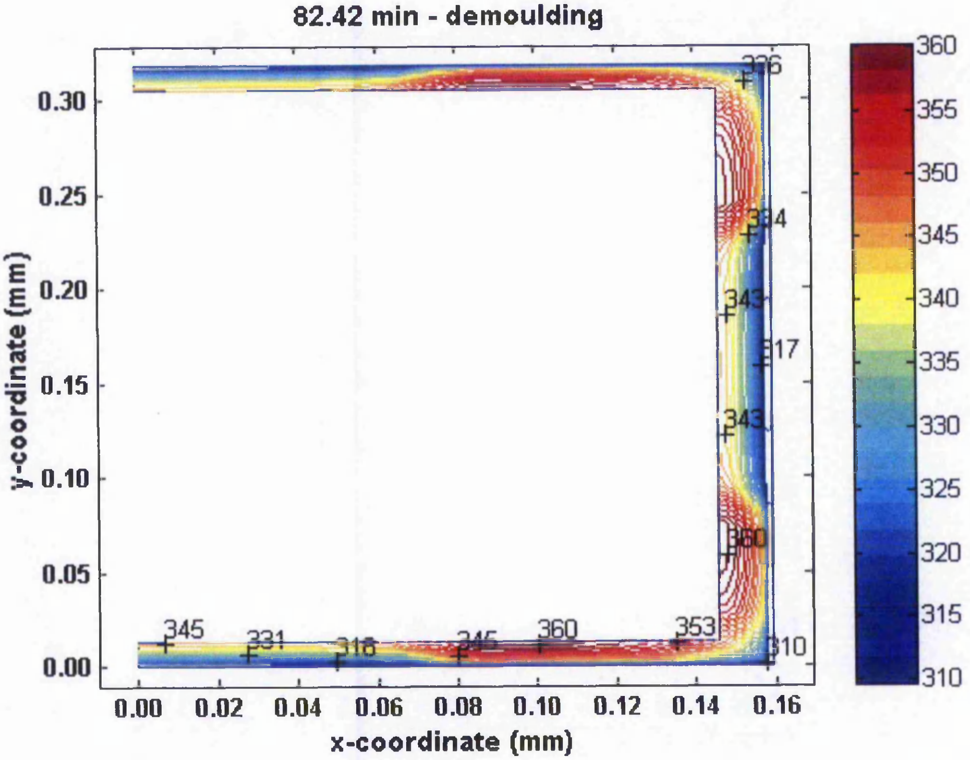

Figure 6-30: Demoulding temperatures inside a 12 mm corner-warped part for external cooling process

6-33 display the calculated contour plots for warped and un-warped parts during the external-internal cooling process. Generally, the temperatures of the inner and outer layers of the parts are lower than the cores. Figure 6-31 shows that the inner and outer layers are at similar temperatures. This means that the external-internal cooling helps to balance the cooling rates on both surfaces, which give a uniform temperature distribution at the core. Compared with Figures 6-28 to 6-30, Figures 6-31 to 6-33 indicate that the external-internal cooling helps to limit the temperature gradients inside the parts.

Chen's off-line experimental results [28] indicate that the warpage started at the *crystalline melting temperature*, T_{cm}. However, an early mould-part separation may be

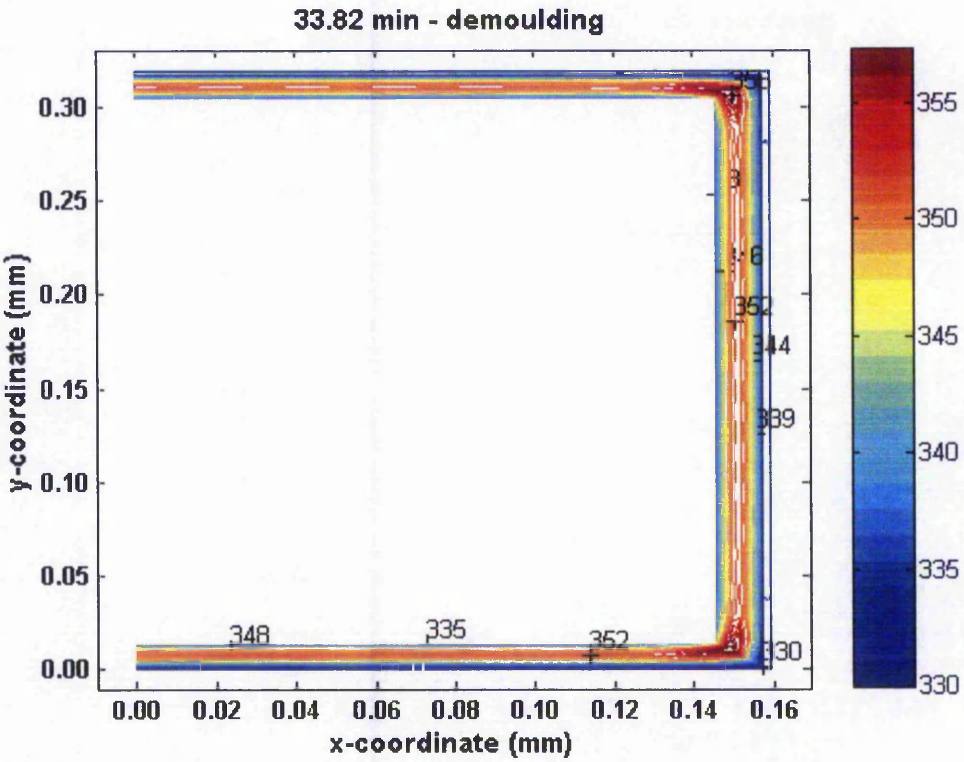

Figure 6-31: Demoulding temperatures inside a 12 mm un-warped part for external-internal cooling process

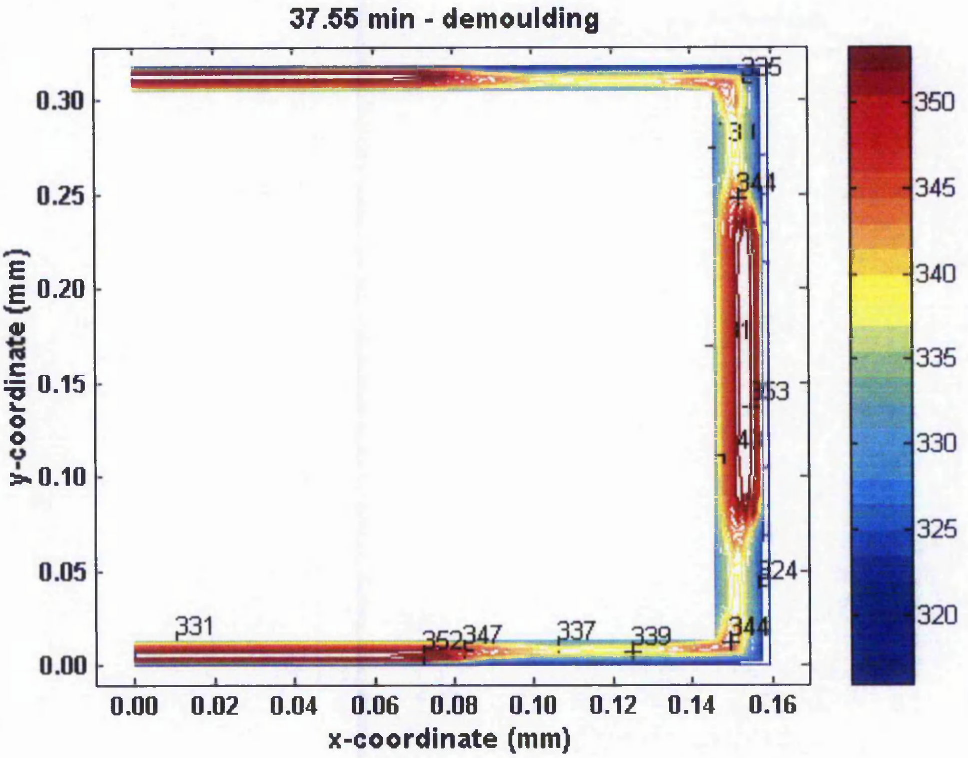
37.55 min - demoulding

Figure 6-32: Demoulding temperatures inside a 12 mm centre-warped part for external-internal cooling process

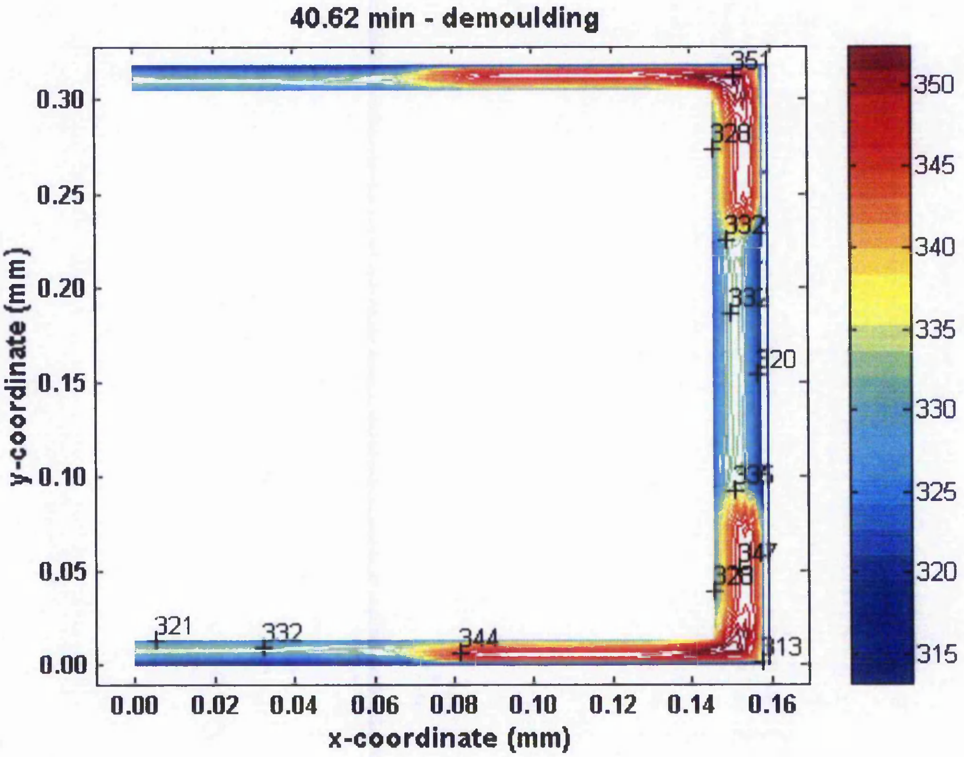
40.62 min - demoulding

Figure 6-33: Demoulding temperatures inside a 12 mm corner-warped part for external-internal cooling process

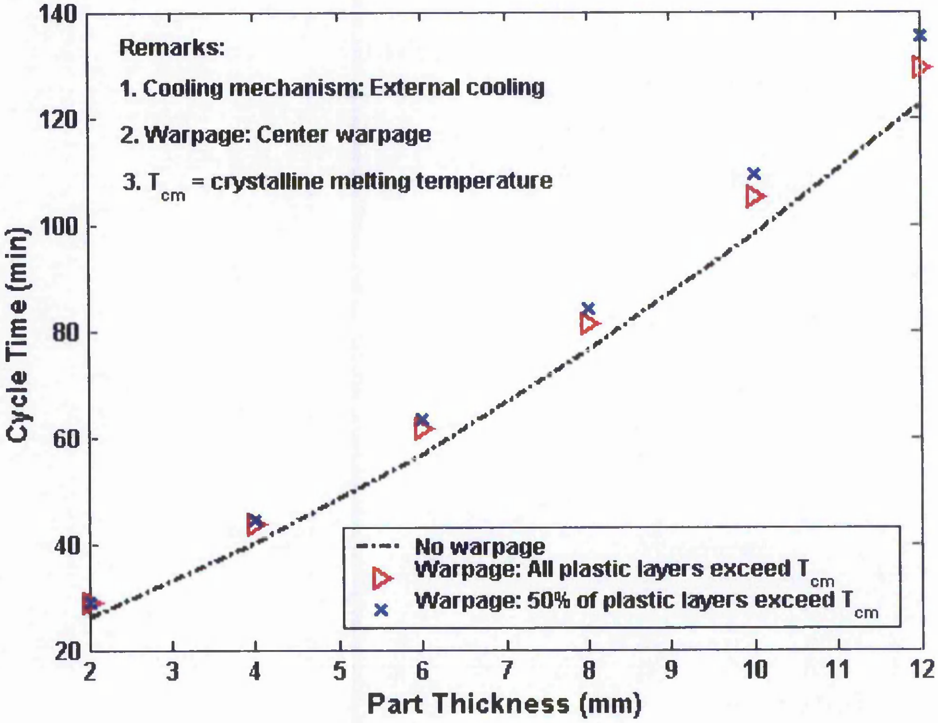

Figure 6-34: Comparisons of cycle times between warped and un-warped parts for external cooling process

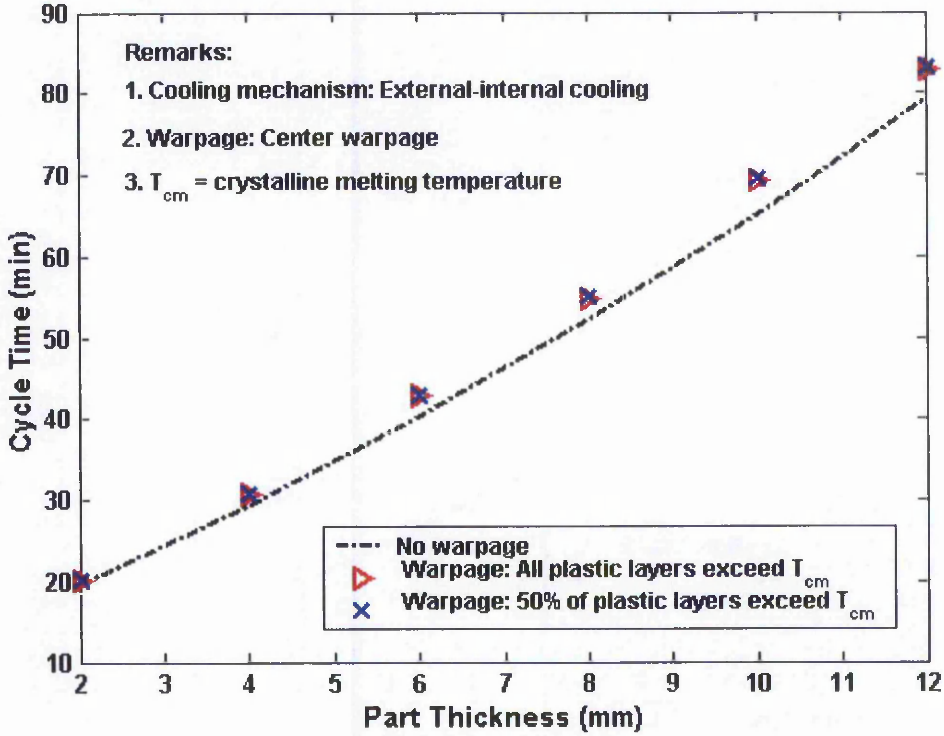

Figure 6-35: Comparisons of cycle times between warped and un-warped problems for external-internal cooling process

possible if excess release agent is applied to the mould surface [26]. Figures 6-34 and 6-35 study the effects of the plastic solidifying stage for warpage on the cycle times during the external and external-internal cooling processes, respectively. As expected, the warpage decreases the efficiency of cooling. Interestingly, Figure 6-34 indicates that the cycle times for parts less than $8mm$ are almost unaffected by the physical stage of the polymer when warpage begins. The effect only becomes evident when the part thickness is above $8mm$. The physical stage has a negligible effect on the cycle times when the external-internal cooling method is modelled (Figure 6-35).

Figures 6-36 to 6-40 show the 8-stage parametric contours for each different cooling condition as discussed above. The parametric simulations delineate the temperature changes in the $12mm$ parts when they are solidified and cooled down to $80\ {}^{0}C$, the demoulding temperature. The figures also show the influence and importance of the multi-dimensional heat transfer in warpage analysis.

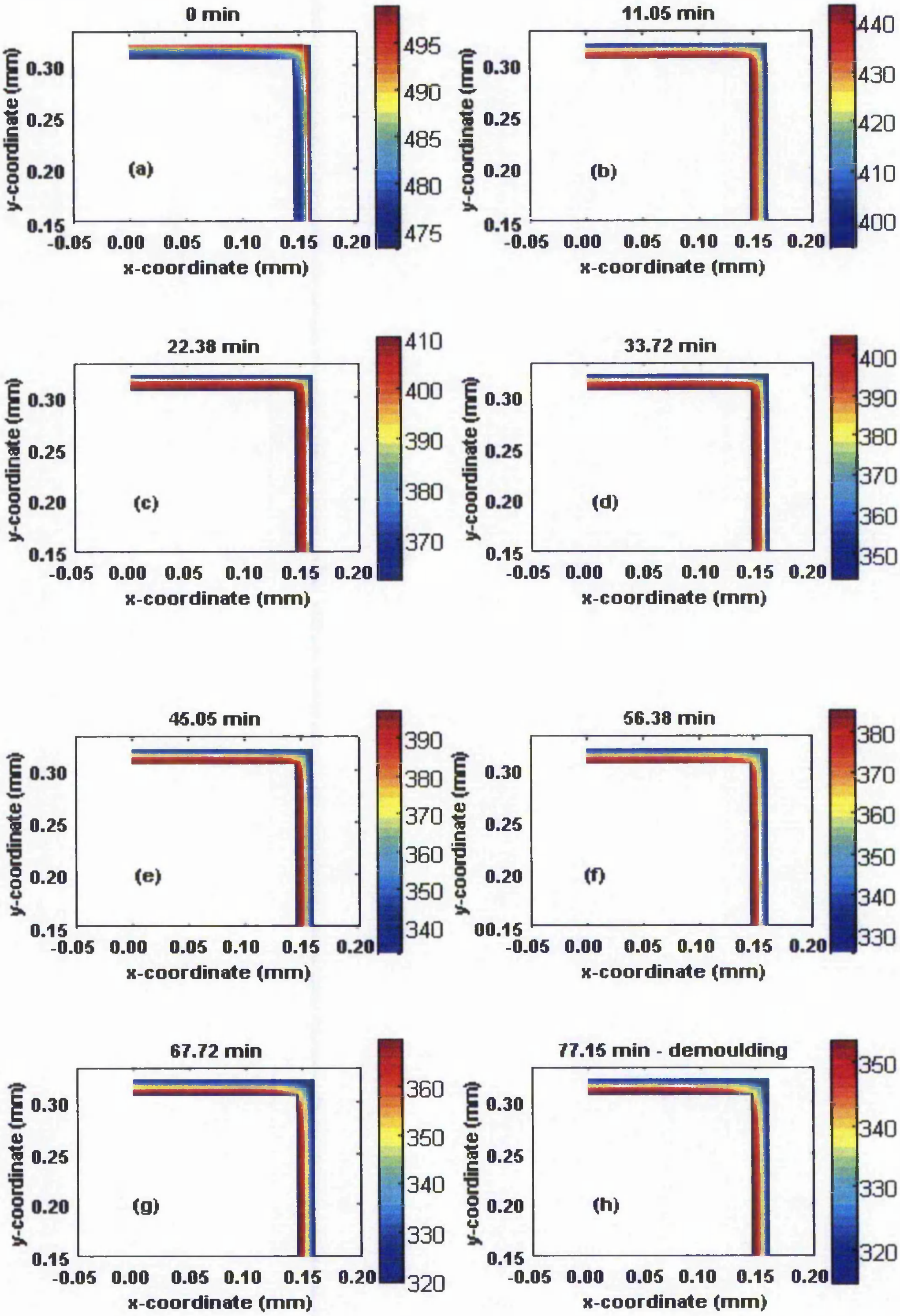

Figure 6-36: Parametric contour plots of a 12 mm un-warped part during external cooling process

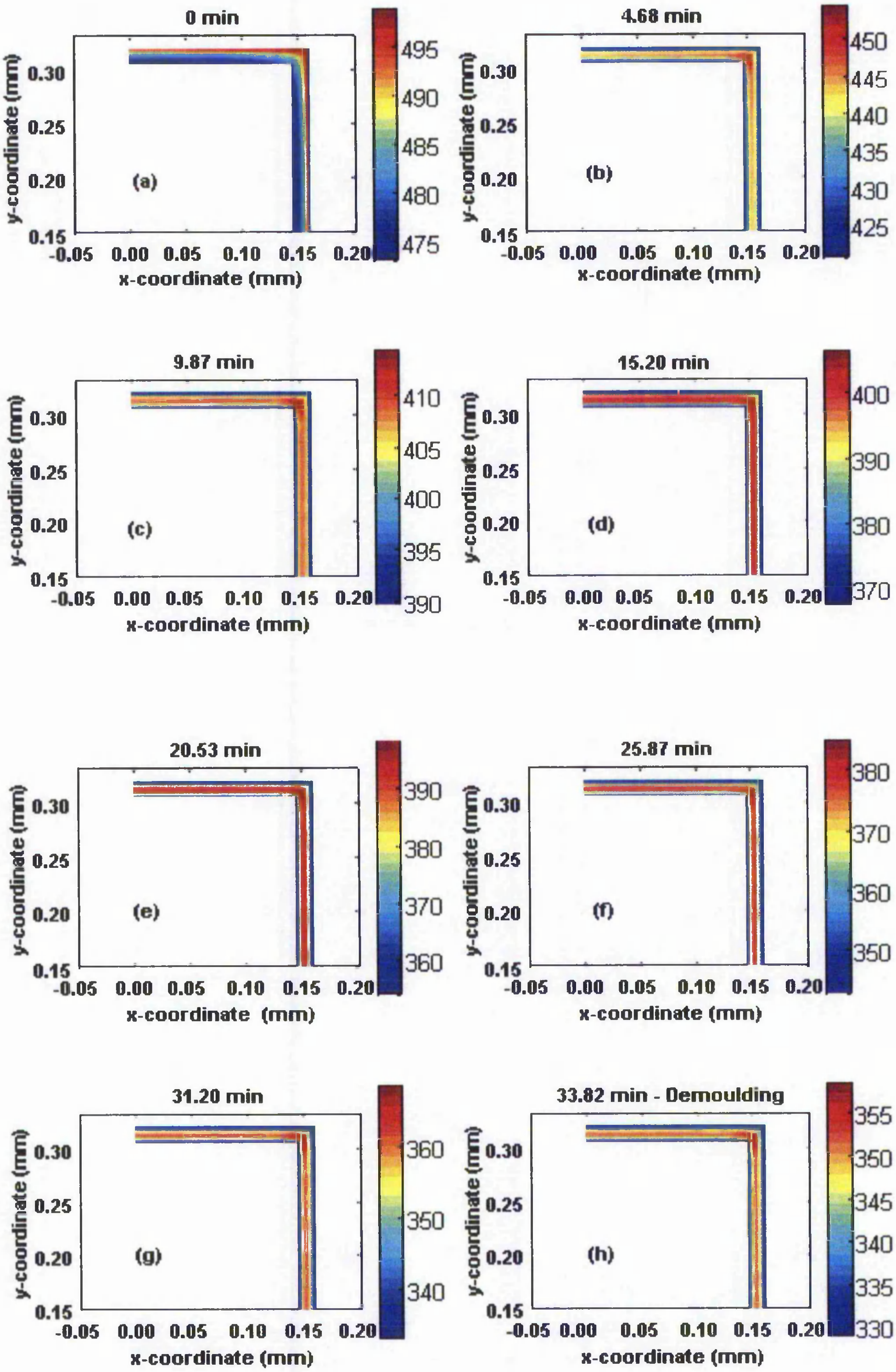

Figure 6-37: Parametric contour plots of a 12 mm un-warped part during external-internal cooling process

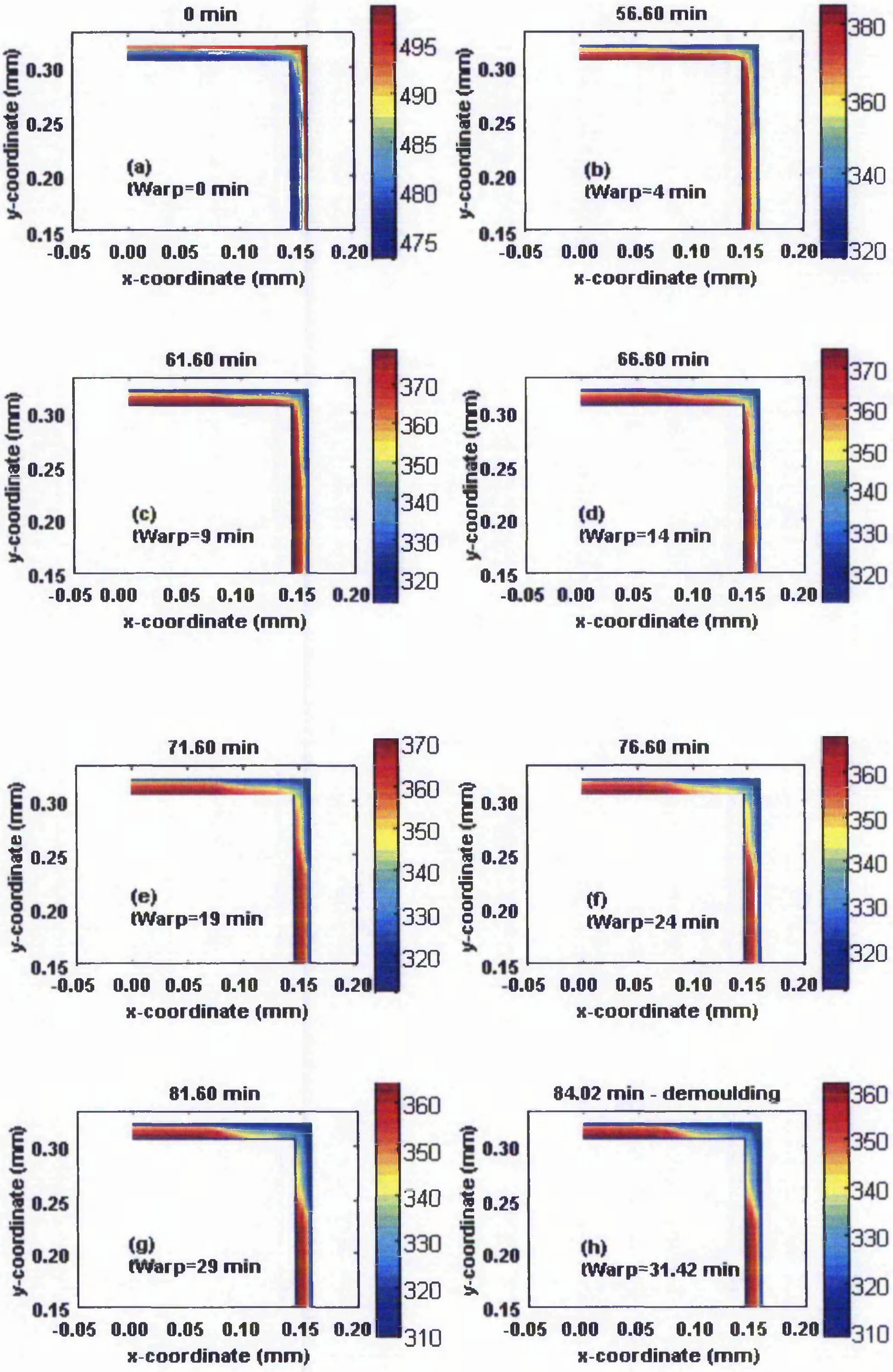

Remark: 'tWarp' – total time since warpage begins

Figure 6-38: Parametric contour plots of a 12 mm centre-warped part during external cooling process

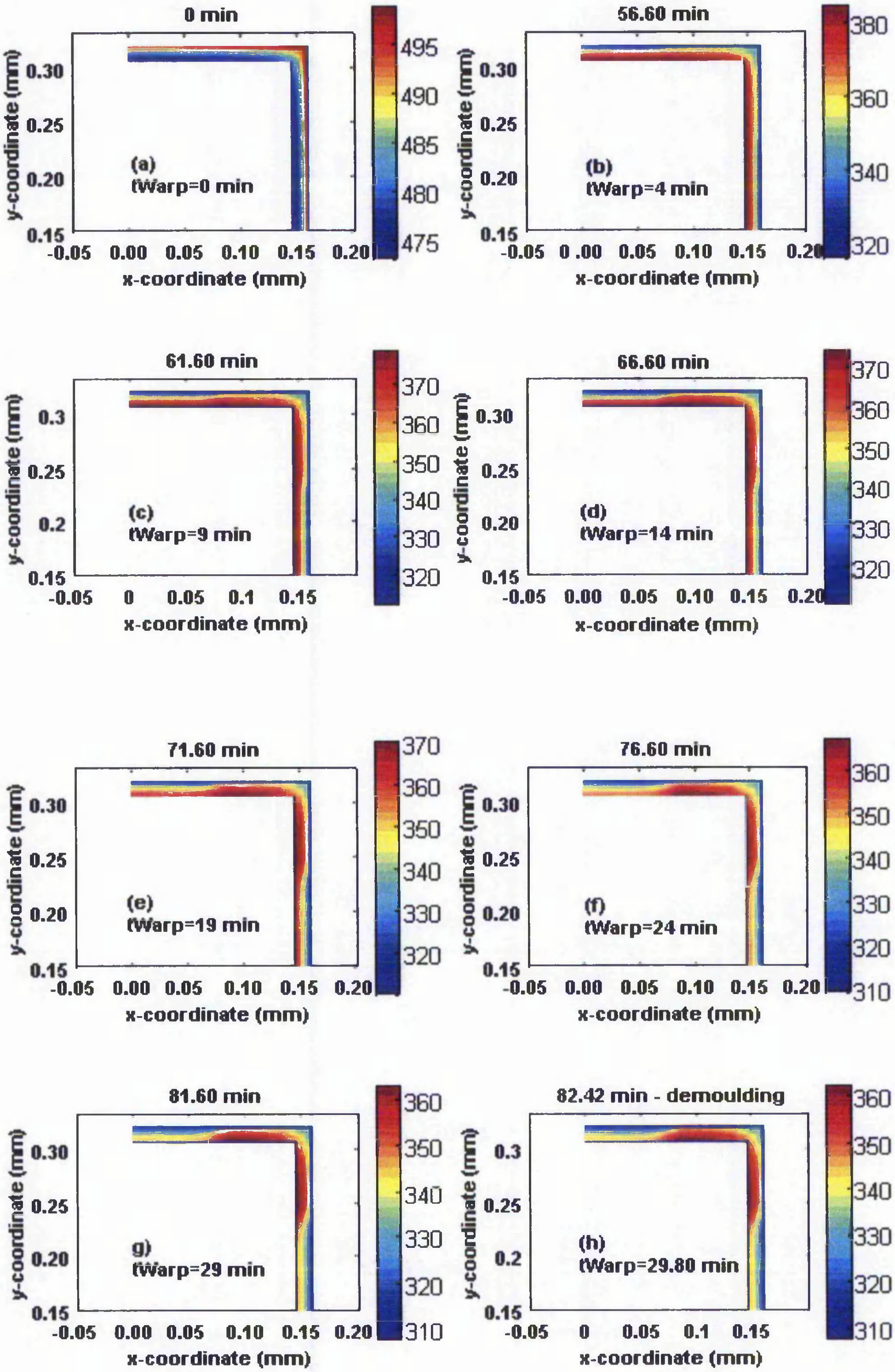

Remark: 'tWarp' – total time since warpage begins

Figure 6-39: Parametric contour plots of a 12 mm corner-warped part during external cooling process

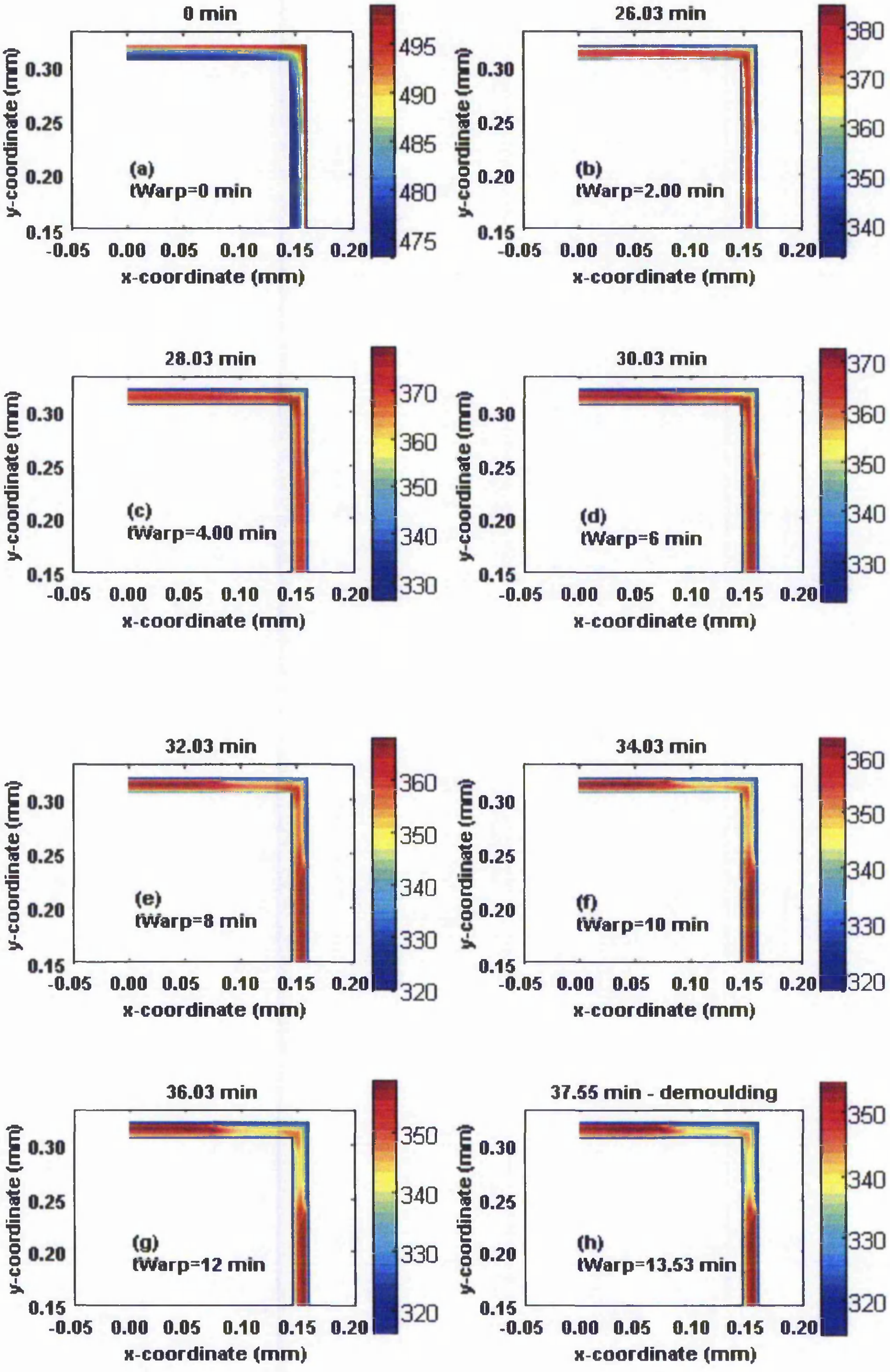

Remark: 'tWarp' – total time since warpage begins

Figure 6-40: Parametric contour plots of a 12 mm centre-warped part during external-internal cooling process

6.8 Dimensional Analysis of Process Parameters

Dimensional analysis can reduce the number of parameters in a rotomoulding study. According to Frank and Mark [59], the results obtained from this method are rather incomplete without experimental data. Unfortunately, experimental data for the different physical quantities are often not available for rotational moulding. This is because the experimental methods to measure these data are costly and too involved to be practical. Here, some new and Gogos *et al.*' [53,37] dimensionless groups are used to study the physical, boundary and time conditions of the rotational moulding system, quantitatively. The relationships of the dimensionless groups in Gogos *et al* [53] to rotational moulding have been evaluated by using various numerical approaches. The evaluations assumed to be able to compensate for the lack of empirical data for the present dimensional analysis. Consequently, this allows further use of the dimensionless groups for studying the effects of the external heating, external cooling, external-internal cooling and warpage on the rotomoulding cycles.

The adopted dimensionless groups are:

$\Pi_1 = \dfrac{t_{ov} h_{ov}}{\rho_m c_m \delta_m}$ = Dimensionless heating time (*New*)

$\Pi_2 = \dfrac{t_{cy} h_{ov}}{\rho_m c_m \delta_m}$ = Dimensionless cycle time

$\Pi_3 = \dfrac{\rho_{P,l} c_{p,l} \delta_{p,l}}{\rho_m c_m \delta_m}$ = Plastic to mould thermal capacitance ratio

$\Pi_4 = \dfrac{\rho_{P,mu} c_{p,mu} \Delta T_{p,mu}}{\rho_{p,l} c_{p,l} \Delta T_{p,l}}$ = Dimensionless latent heat per unit volume for plastic phase change (*New*)

$\Pi_5 = \dfrac{k_{p,l}}{\delta_p h_{ov}}$ = Dimensionless plastic conductance

$\Pi_6 = \dfrac{k_m}{\delta_m h_{ov}}$ = Dimensionless mould conductance

$\Pi_7 = \dfrac{T_d - T_{oc}}{T_o - T_{oc}}$ = Dimensionless demoulding temperature

$\Pi_8 = \dfrac{h_{ov}}{h_{oc}}$ = External heating to cooling heat transfer coefficient ratio

$\Pi_9 = \dfrac{h_{in}}{h_{oc}}$ = Internal air to external cooling heat transfer coefficient ratio

$\Pi_{10} = \dfrac{h_{\text{int}}}{h_{oc}}$ = Warpage to external cooling heat transfer coefficient ratio (*New*)

The dimensionless plots of the 'Base case' (base case) in the following figures are constructed from the experimental data for the $4\,mm$ part as given in Table 6-4.

Figures 6-41 to 6-48 demonstrate the influences of the key dimensionless process parameters on the dimensionless heating time, Π_1, and dimensionless cycle time, Π_2. With similar cooling methods, either external or external-internal cooling, all the dimensionless plots for the warped parts in general show a similar line pattern as their corresponding un-warped parts; Π_2 is shifted upwards approximately by a constant value for the dimensionless groups Π_3, Π_4, Π_5, Π_6, Π_9, and Π_{10}, and not by a constant value for the dimensionless groups Π_7, Π_8, and Π_9. The upward shifts of Π_2 due to warpage are comparatively small for the external-internal cooling method compared with the external cooling method. As a whole, Figures 6-41 to 6-48 indicate that the external-internal cooling method is still more important then the external cooling method in shortening the cycle times for the dimensionless groups Π_3 to Π_9 (i.e. lower value of Π_2).

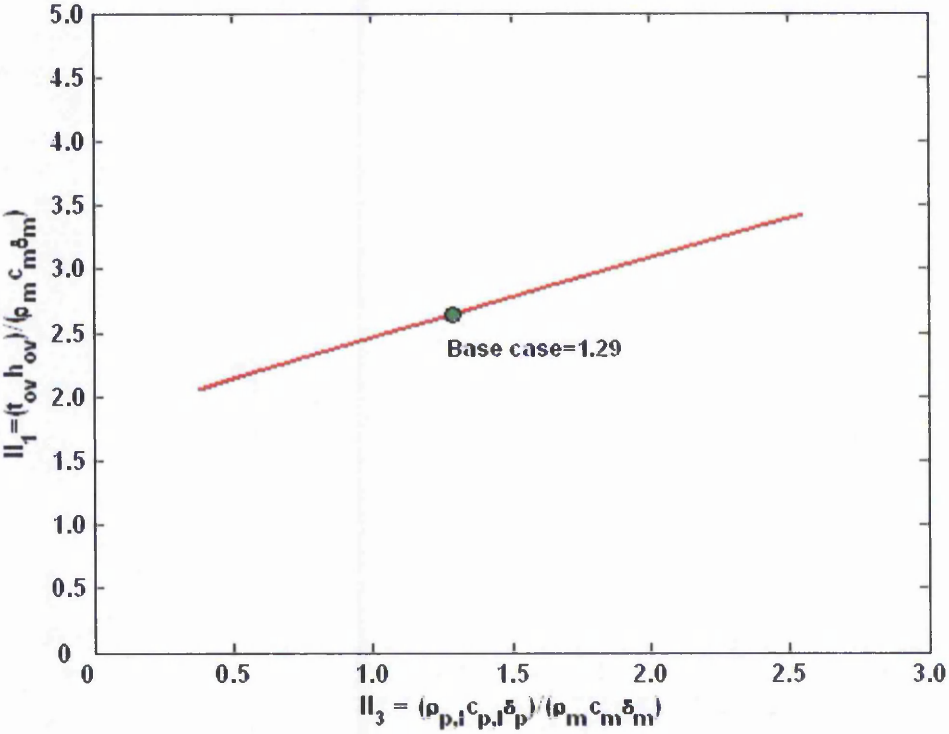

Figure 6-41 (a): Dimensionless heating time (Π_1) versus dimensionless plastics to mould thermal capacitance ratio (Π_3)

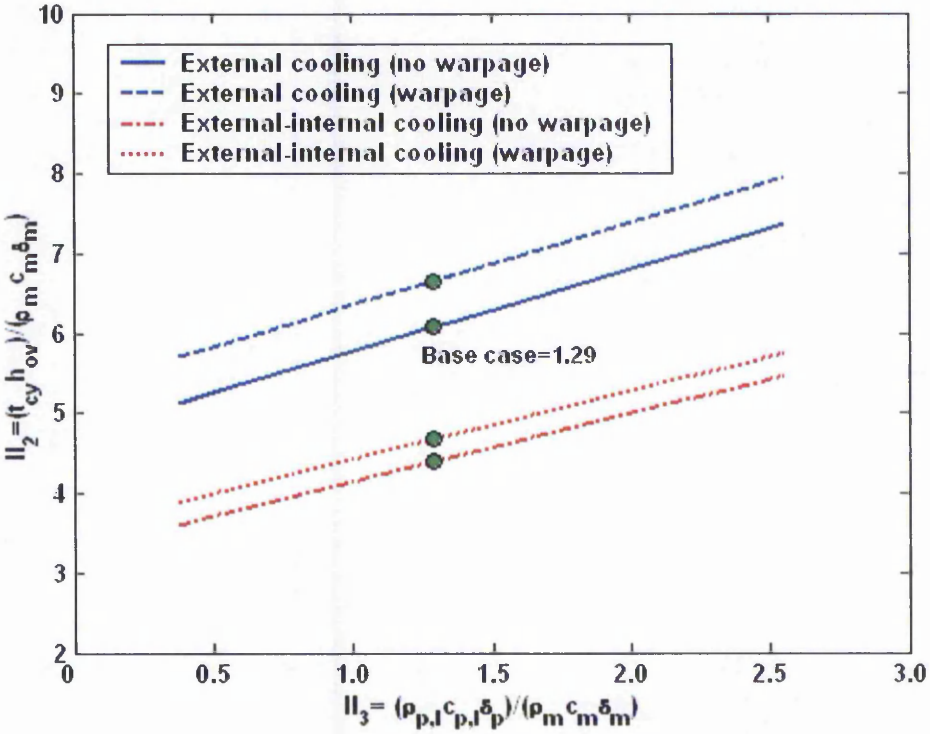

Figure 6-41 (b): Dimensionless cycle time (Π_2) versus dimensionless plastics to mould thermal capacitance ratio (Π_3)

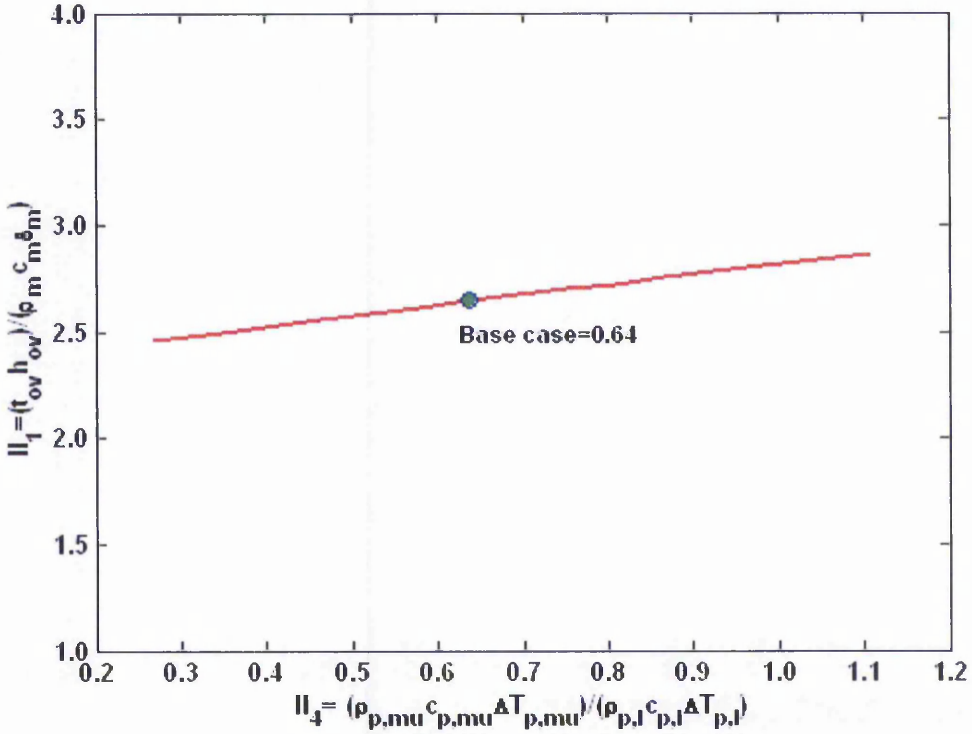

Figure 6-42 (a): Dimensionless heating time (Π_1) versus dimensionless latent heat per unit volume for plastic phase change (Π_4)

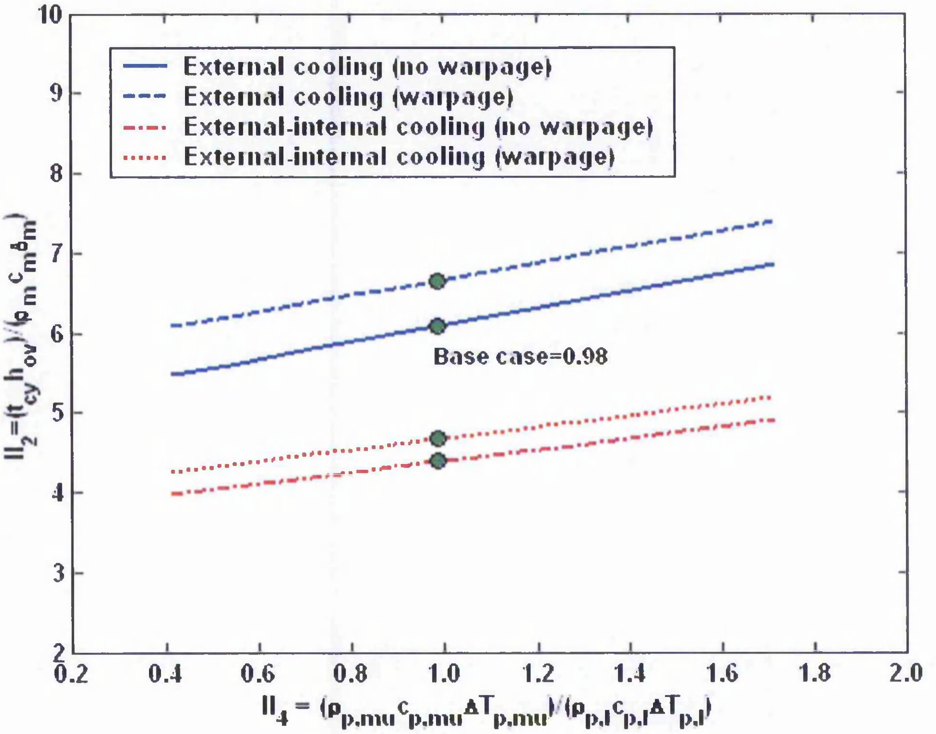

Figure 6-42 (b): Dimensionless cycle time (Π_2) versus dimensionless latent heat per unit volume for plastic phase change (Π_4)

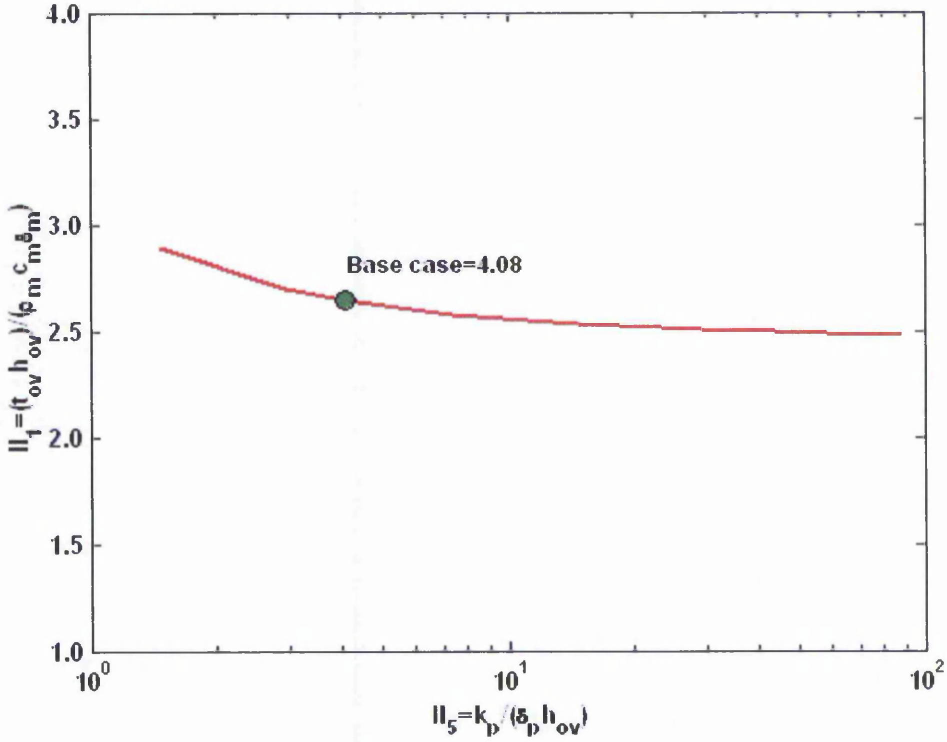

Figure 6-43 (a): Dimensionless heating time (II_1) versus dimensionless plastic conductance (II_5)

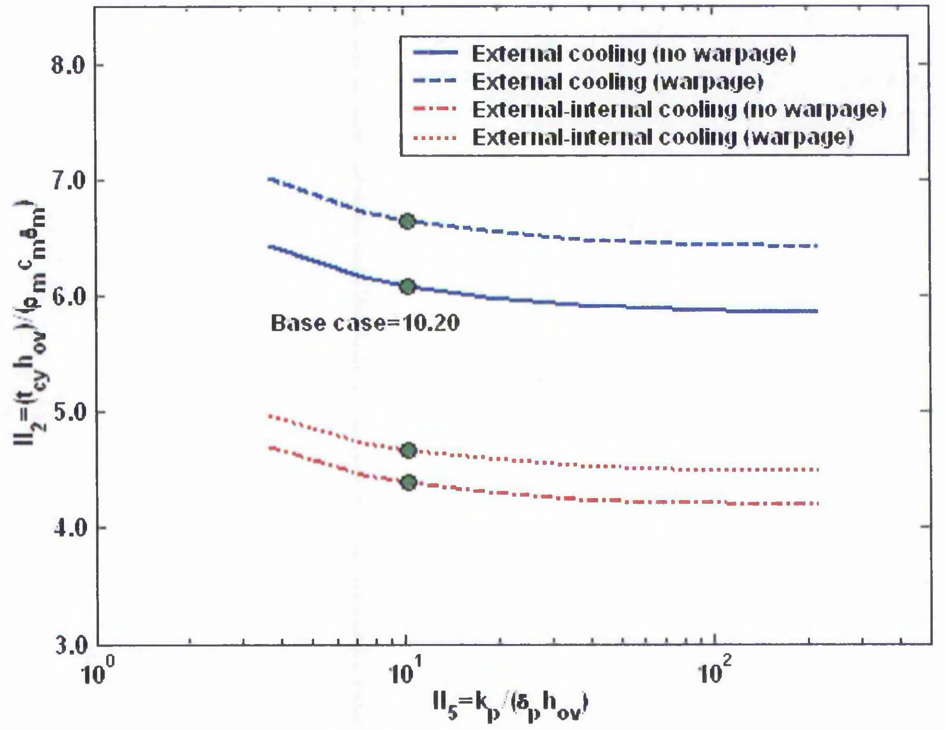

Figure 6-43 (b): Dimensionless cycle time (II_2) versus dimensionless plastic conductance (II_5)

During the dimensional analysis, the variations of each polymer related dimensionless group (Π_3, Π_4, and Π_5) are only based on the selected phase change region that is appropriate (i.e. liquid phase – with subscript l). This is to keep the remaining dimensionless groups constant at the value corresponding to the base case. The selected region is a matter of study interest. The relationship between the dimensionless cycle time, Π_2, and the dimensionless groups of the polymer Π_3, Π_4 and Π_5 are plotted in Figures 6-41(b), 6-42 (b) and 6-43 (b), respectively. In these figures, the differences between Π_2 for the two different cooling methods could be larger if the property variations for *similar parts*, warped parts or un-warped parts, involved a wider temperature range to allow for a phase changes. Thus the cooling methods have considerable influence in enhancing the dimensionless group Π_2.

The magnitudes of Π_3 represent the plastic to mould thermal capacitance ratio and Π_4 represent the dimensionless latent heat per unit volume for plastic phase change. According to Figures 6-41 (a), (b) and Figures 6-42 (a), (b), the dimensionless heating time, Π_1, and dimensionless cycle time, Π_2, increase linearly with the increasing Π_3 and Π_4, respectively. The magnitudes of Π_4 indicate that Π_1 and Π_2 are dependent on the melting and crystallization temperature ranges; the wider the phase change temperature the larger the values of Π_4. Since Π_4 represents the dimensionless latent heat of absorption or release per unit volume, any change in the latent heat for a phase change, a linear relationship between Π_1 and Π_4 (or Π_2 and Π_4) will be predicted.

Figures 6-43 (a) and (b) illustrate that if the dimensionless plastic conductance Π_5 is smaller than the base case, Π_1 and Π_2 increase moderately with decreasing Π_5. When

Π_5 is larger than the base case, the values of Π_1 and Π_2 are almost approaching asymptotically. This suggests that any increase in the magnitude for the poor polymer thermal conductivity does not really improve the *process times* (heating time, t_{ov}, and cycle time, t_{cy}) of this pressure-free rotomoulding process; as the thermal conductivity of the polymer does not vary appreciably for most polymers.

According to Figures 6-44 (a) and (b), neither Π_1 nor Π_2 is sensitive to the change in the dimensionless mould conductance, Π_6. The capability of Π_6 in expediting the process times is limited by the dimensionless group Π_5 that is due to the poor thermal conductivity of the polymer. Thus, Π_6 is regarded as a negligible factor for improving the process times of rotational moulding.

The value of Π_7 is a measure of the demoulding temperature. Its relationship to Π_2 is plotted in Figure 6-45. For Π_7 smaller than the base case, i.e. decreasing the demoulding temperature, T_d, the dimensionless cycle time Π_2 increases moderately with decreasing Π_7 for all the cooling circumstances. However, the continuous decreasing Π_7 eventually results in a steep increase in Π_2. At this stage, warpage becomes important and prevents any improvement in the dimensionless cycle time, Π_2, especially when the external cooling method is used. For external-internal cooling, the variation of Π_2 is comparatively small between warped and un-warped parts when there is a further decrease in Π_7. This implies that external-internal cooling requires less additional cooling time to solidify warped products. It also indirectly implies that external-internal cooling could possibly prevent producing 'over' un-solidified parts

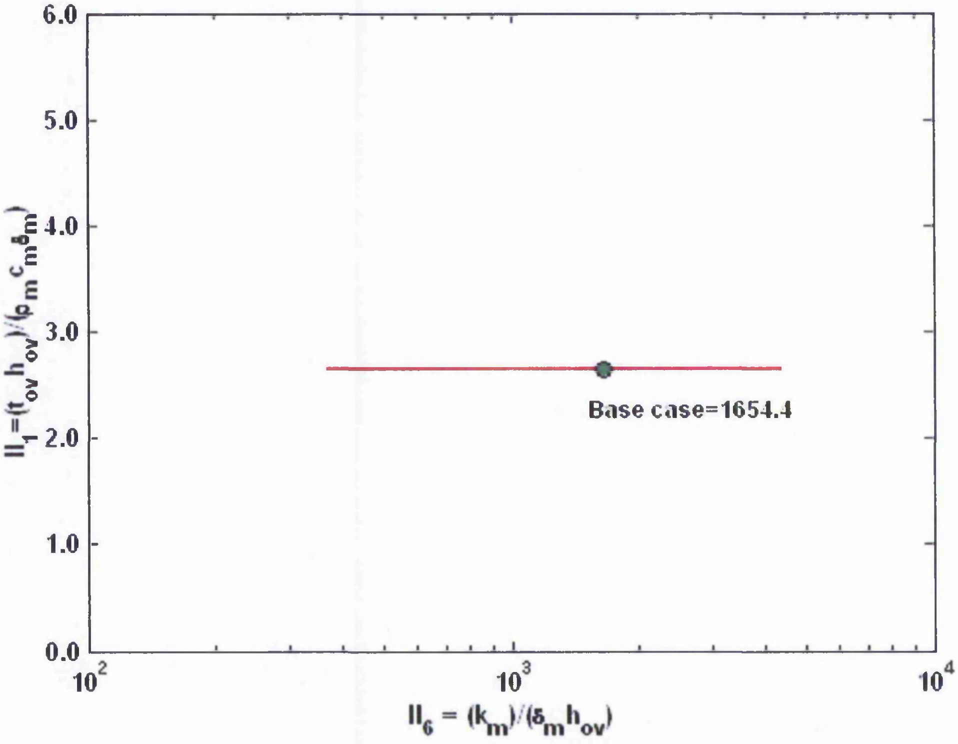

Figure 6-44 (a): Dimensionless heating time (Π_1) versus dimensionless mould conductance (Π_6)

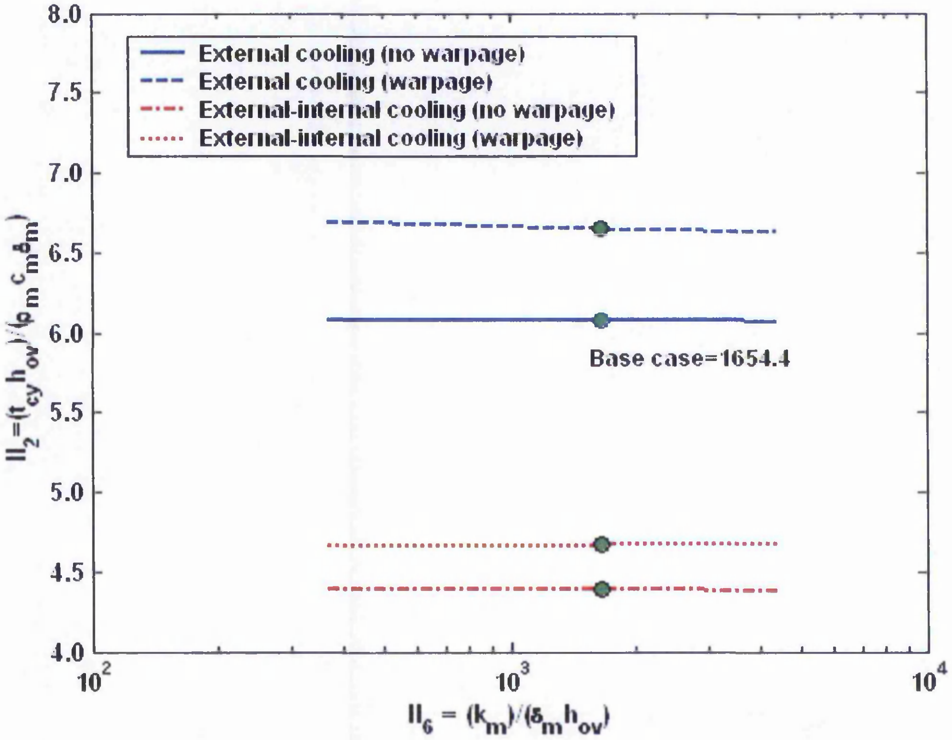

Figure 6-44 (b): Dimensionless cycle time (Π_2) versus dimensionless mould conductance (Π_6)

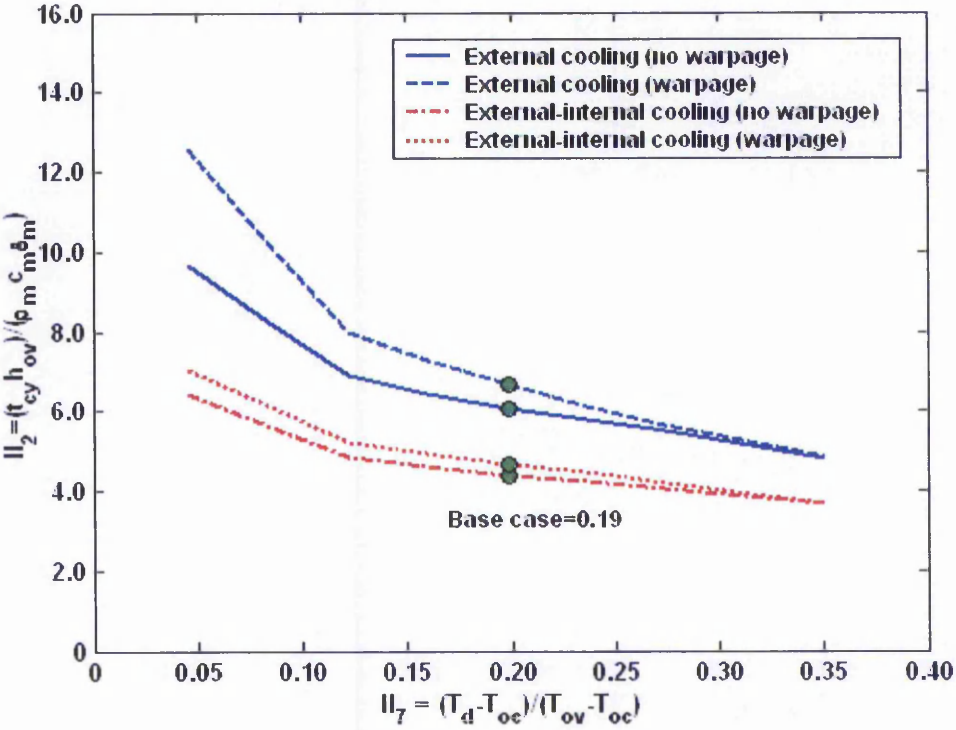

Figure 6-45: Dimensionless cycle time (Π_2) versus dimensionless demoulding temperature (Π_7)

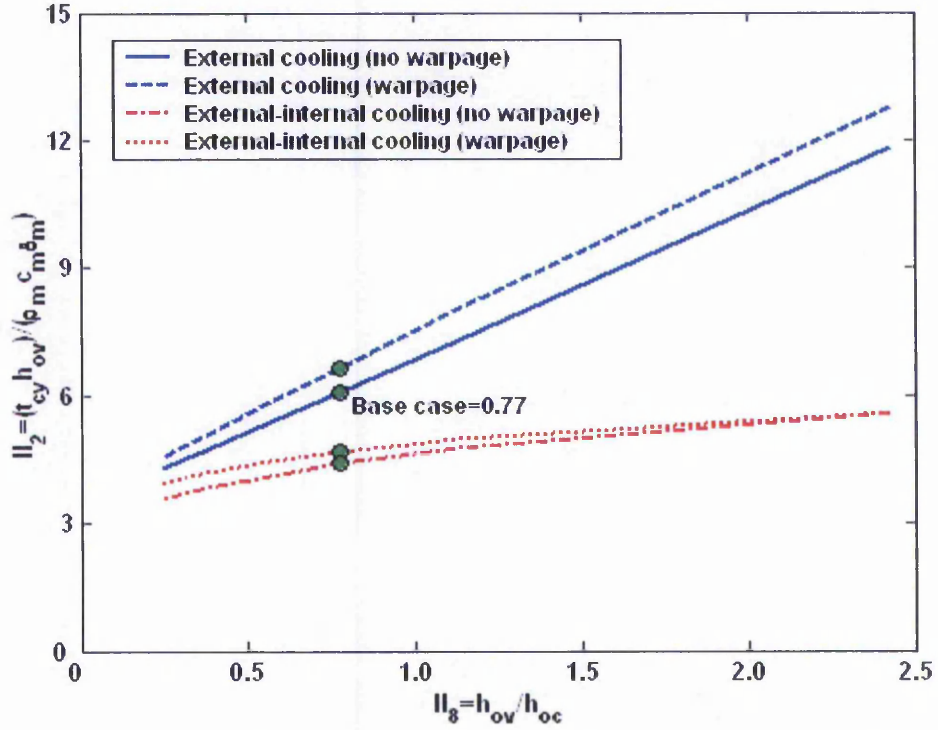

Figure 6-46: Dimensionless cycle time (Π_2) versus external heating to cooling heat transfer coefficient ratio (Π_8)

even if the warpage cannot be detected in practice. So the external-internal cooling method is a promising technique to improve the cycle time and to maintain the quality of the final products. When the dimensionless group Π_7 is larger than the base case, Π_2 is no longer affected by warpage. This is because the warpage occurs a short time after the demoulding temperature is reached. The dimensionless cycle time, Π_2, however, is still influenced by the method of cooling.

The curves in Figure 6-46 show that the dimensionless cycle time Π_2 increases with increasing the dimensionless group representing the external heating to cooling heat transfer coefficient ratio, Π_8. The plots, however, generally lack linearity. For two-side cooling (external-internal cooling), Π_2 increases almost monotonically with increasing Π_8 above the base case (corresponds to a decrease in h_{oc}). This is because the cooling process could still continuous from the internal plastic surface, even when Π_8 is high. In contrast, Π_2 for the one-side cooling model (external cooling) is almost linearly sensitive to the change of Π_8. The dimensionless group Π_2 is significantly improved by the internal-external cooling method compared to the external cooling method.

As shown in Figure 6-47 (a), Π_2 of the external cooling method is not sensitive to the magnitude of internal air to external cooling heat transfer coefficient ratio, Π_9, which corresponds to change in h_{in}. The dimensionless cycle time Π_2 is influenced by h_{oc} which is inversely proportional to h_{in}. With the external-internal cooling method, Figure 6-47 (b) shows that decreases in Π_9 from the base case leads to dramatic increase in Π_2. For Π_2 larger than the base case, however, Π_9 is gradually becomes asymptotic.

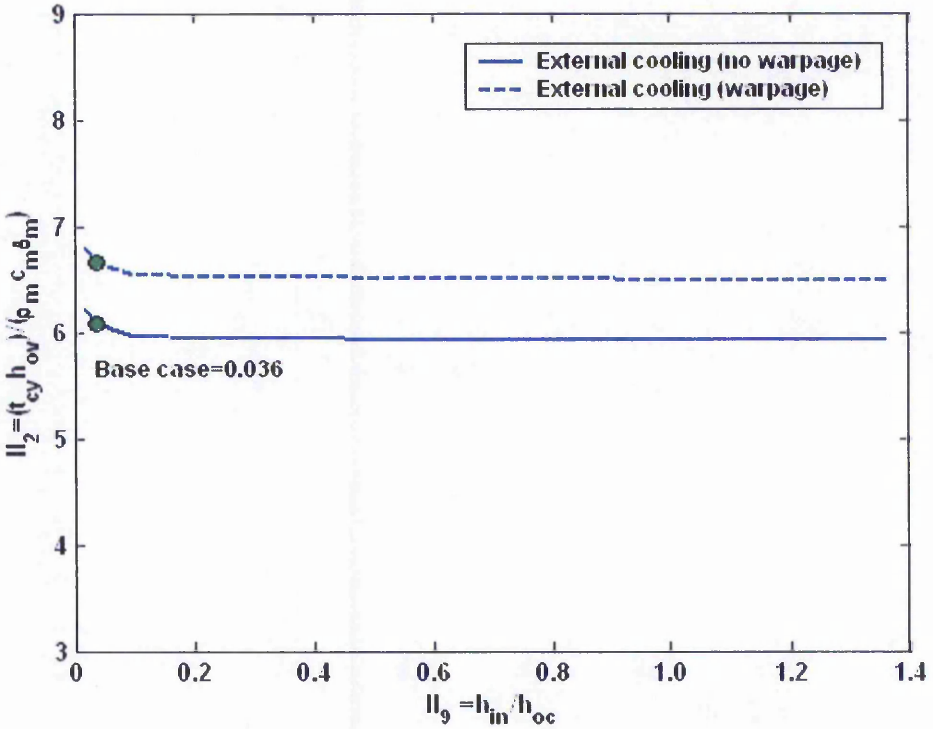

Figure 6-47 (a): Dimensionless heating time (II_1) versus internal air to external cooling heat transfer coefficient ratio (II_9)

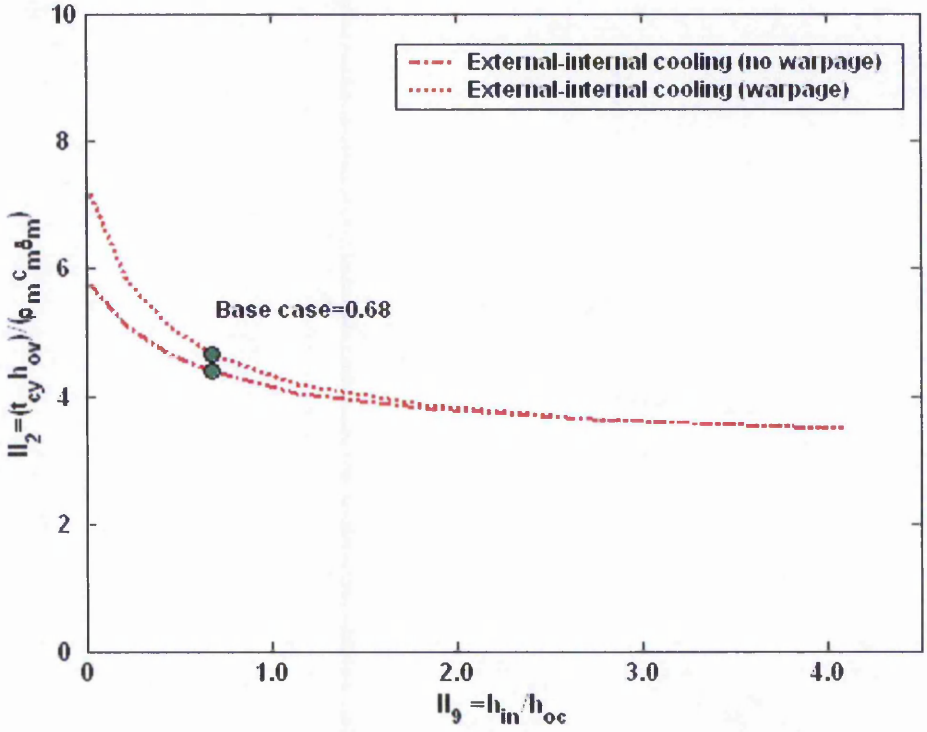

Figure 6-47 (b): Dimensionless cycle time (II_2) versus internal air to external cooling heat transfer coefficient ratio (II_9)

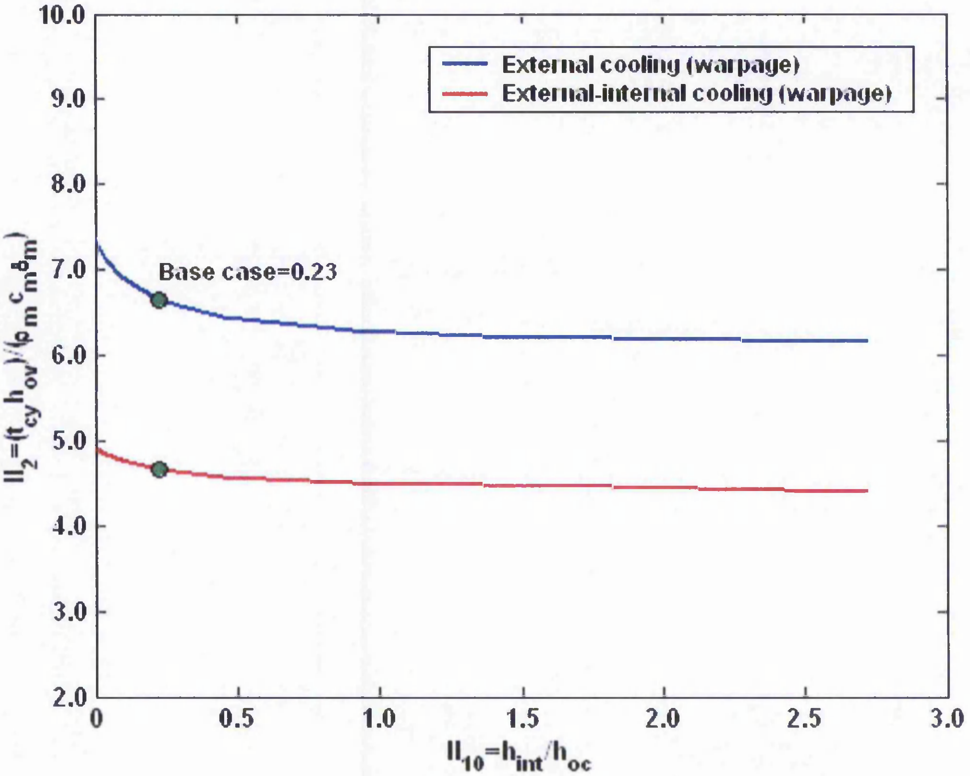

Figure 6-48: Dimensionless cycle time (Π_2) versus air gap to external cooling heat transfer coefficient ratio (Π_{10})

This implies that there is a limit for the cooling method to improve Π_2, which is because of the poor thermal properties of plastics. A large Π_9 can be produced by increasing h_{in}; for example, by blowing high velocity air into the mould. However, this may potentially blow the mould apart when a high internal pressure builds up. The magnitude of Π_{10} represents warpage to external cooling heat transfer coefficient ratio. Figure 6-48 shows that the dimensionless cycle time, Π_2, is generally not sensitive to Π_{10}. Thus, h_{int} can be set to a constant value for warpage modelling of the rotational moulding process.

CHAPTER 7

CONCLUSIONS

As a result of the numerical studies carried out in this research, the following conclusions have been drawn:

1. A new two-dimensional slip flow methodology has been derived to simulate the heat transfer problem in the rotational moulding process.

2. With the slip flow methodology:
    - (i) The thermal modelling for the heating powder stage has been simplified by obviating the considerations of the mixing powder, the powder pool tracking and the changeable powder mass inside the enclosed mould.
    - (ii) The SDM and MDM models have been developed for the modelling of the rotational moulding process, in which the latter provides a better heat transfer description for the internal air.
    - (iii) A semi-implicit approach has been introduced into these slip flow models for predicting the internal air temperature inside the dynamic rotating mould. Thus the numerical difficulties in predicting the heating temperature of this complex, multi-interacting internal air can be simulated by using the continuous-based finite element procedure.

3. The SDM and MDM models are stable and capable to predict satisfactory temperature profiles, heating time and cycle time of the rotomoulding system for part thickness up to $12\,mm$.

4. The MDM model can predict more aspects of the process behaviour and gives better temperature profiles for the heating cycle of rotational moulding than the SDM model, without affecting the computational time. The former requires a marginal variation of h_{ov} for different categories of part thickness, but the latter needs only a constant input of h_{ov} for the simulations.

5. The MDM model is an *improvable model* for better predictions because the numerical topology for constructing the layer-based plastic deposition is flexible.

6. The predicted internal air temperature profiles resemble the experimental results and can identify the six major processing stages in the rotational moulding cycle.

7. The coincident node technique has shown its flexibility in handling problems with a changeable contact surface.

8. The proposed *efficient algorithm* for describing the phase change is capable of handling the melting and solidification problems with an acceptable level of accuracy. The algorithm has minimized the numerical non-linearity and consequently the simulation time.

9. The MDM results show that the heating plateau of the internal air temperature profile is mainly caused by the melting process of the polymer instead of the formation of the first coated plastic layer onto the inner mould surface.

10. The initial numerical studies on warpage predict that:

(i) Most temperatures inside the warped portions of the rotomoulded part are higher than the internal air temperature during the cooling.

(ii) The internal air temperature for the warped part might be a misleading guide to the optimum demoulding time under the 'common-practice' demoulding air temperature of $80\,^{0}C$ by rotomoulders.

(iii) Warpage will reduce the appearance of the crystallization-induced plateau in the internal air temperature profile. Any similar observation in the experimental air profiles might possible indicate that the part has warpage.

(iv) Warpage disturbs the heat-flow direction and the temperature distribution inside the warped part significantly.

(v) With external cooling, it is only with thicker parts that the onset of warpage could have an influence on the cycle time.

(vi) With the external-internal cooling, the onset of warpage has no influence on the cycle time.

(vii) Warpage causes the formation of a heterogeneous layered structure inside the final products.

(viii) Warpage prolongs the cycle time because of the heat inversion and the poor heat transfer across the warped portion.

(ix) Multi-dimensional thermal modelling is important to understand the heat transfer behaviour inside the warped parts.

11. External-internal cooling can minimize the cycle time and even straighten the temperature gradient inside rotomoulded products.

12. The dimensionless heating time, II_1, and cycle time, II_2, are:

(i) Sensitive to dimensionless groups: plastic to mould thermal capacitance ratio (Π_3), dimensionless latent heat per unit volume for plastic phase change (Π_4), dimensionless demoulding temperature (Π_7), external heating to cooling heat transfer coefficient ratio (Π_8), and internal air to external cooling heat transfer coefficient ratio for internal cooling (Π_9 of internal cooling process).

(ii) Insensitive to dimensionless groups: dimensionless plastic conductance (Π_5), dimensionless mould conductance (Π_6), internal air to external cooling heat transfer coefficient ratio (Π_9 of no internal cooling process), and warpage to external cooling heat transfer coefficient ratio (Π_{10}).

13. The results from the dimensionless demoulding temperature (Π_7) shows that the internal-external cooling could help to minimize possible 'over' under-solidified part when a warped part is cooled under a normal (un-warped) process condition.

CHAPTER 8

FUTURE WORK

Several improvements and studies are suggested for the future research development of the rotational moulding process. They include:

1. To further studies the refinement of the comparatively improvable MDM model. The future developments can be:

   (i) Improving the less satisfied *Stage 2* of the predicted air temperature profile in the rotational moulding cycle.

   (ii) Improving the topological structure for the layer-based plastic bed, and thus the 'additional' energy transfer from the mould to the mixing bed can be overcome and a constant value of the external heat transfer coefficient can be used.

   (iii) Improving the capability of MDM model for modelling the part thickness beyond $12\,mm$.

   (iv) Modelling the multiple-layered foam products of the rotational moulding.

2. To further reduce the computational time (i.e. Galerkin Alternating Direction Method).

REFERENCES

[1] D. Ramazzotti, Rotational molding – the state of the art, SPE (Society of Plastics Engineers), October 1975, pp.43-63.

[2] R. J. Crawford and J. L. Throne, Rotational molding technology. Portland: William Andrew Inc, 2001.

[3] P. F. Bruins, Basic principles of rotational molding. New York: Gordan and Breach, Science Publishers, 1971.

[4] G. L. Beall, Rotational molding – design, materials, tooling, and processing. Munich: Hanser Publishers, 1998.

[5] Rotational Moulding, Cinderella process ready for the high tech ball, Plastics & Rubber Weekly, January 1987, 24, 19.

[6] M. P. Kearns, R. J. Crawford, and N. Corrigan, A comparison between open flame and hot air heating methods for the rotational moulding of plastics, ANTEC, 2000, pp.1360-1365.

[7] M. J. Wright, A. G. Spence and R. J. Crawford, An analysis of heating efficiency in rotational moulding, ANTEC, 1997, 439, pp.3184-3188.

[8] Gleann Beall Plastics Ltd, Rotational molding: today and tomorrow, ANTEC, 1997, pp.3178- 3183.

[9] M. A. Rao and J. L. Throne: Principles of rotational molding. Polymer Engineering and Science, 1972, 12, pp.237-264.

[10] R. J. Crawford, Rotational moulding of plastics. England: Research Studies Press Ltd, 1996.

[11] X. Liang, Prediction of the rotational moulding cycle. PhD Thesis, Queen's University, 1996.

[12] D. Ramazzotti, Rotational Molding – a quick update, Plastic Engineering, 1975, pp.32-35.

[13] M. Narkis and N. Rosenzweig, Polymer powder technology. Chichester: John Wiley & Sons, 1995.

[14] P. J. Nugent, Theoretical and Experimental Studies of Heat Transfer During Rotational Molding Process. PhD Thesis, Queen's University, 1990.

[15] R.J. Crawford, Plastic engineering. Oxford: Butterworth Heinemann, 1998.

[16] W. Michaeli, Plastics Processing: An Introduction. Porland: Hanser Gardner Publications, 1995.

[17] http://www.ferryindustries.com/rot_mold.html, 2003 (date accessed).

[18] J. L. Throne, Powder flow during rotational molding, ANTEC, Plastics: Annual Technical Conference, 2002, 1, pp.67-70.

[19] http://www.foamandform.com/minutes/rmnew1.php, 2002 (date accessed).

[20] W. Michaeli, Plastic processing: An introduction. 1st ed. Munich: Hanser, 1992.

[21] P. J. Nugent, and R. J. Crawford, Computer simulation of the rotational moulding process for plastics. Plastic and Rubber Processing and Application, 1989, 11, pp.107-124.

[22] E. J. Wright and R. J. Crawford, Computer simulation of the rotational moulding of plastics, ANTEC, 1999, pp.1441-1445.

[23] M. J. Wright and R. J. Crawford, A comparison bewteen forced air convection heating and direct electrical heating of moulds in rotational moulding, ANTEC, 1999, pp.574.

[24] J. A. Scott and R. J. Crawford, An experimental study of heat transfer during rotational moulding of plastic. Plastic and Rubber Processing and Application, 1985, pp.239-248.

[25] R. C. Progelhof, G. Cellier and J. Throne, New technology in rotational molding: powder densification, SPE, 1982, pp 627-629.

[26] R.J. Crawford and K.O. Walls, shrinkage and warpage of rotationally moulded products, SPE, 1999, pp.135-139.

[27] C. H. Chen, J. L. White and Yasuhiko Ohta, Mold pressurization as a method to reduce warpage in rotational molding of polythylene. Polymer Engineering and Science, December 1990, 30, pp.1523-1528.

[28] C. H. Chen, J. L. White and Y. Ohta, A fundamental experimental study of the mechanisms of warpage and shrinkage of polyethylene in rotational molding. Intern. Polymer Processing, 1991, VI, pp.212-216.

[29] K. Iwakura, Y. Ohta, C.H. Chen, and J. L. White, A basic study of warpage and heat transfer in rotational molding, ANTEC, 1989, pp.559-562.

[30] K. Iwakura, Y. Ohta, C.H. Chen and J. L. White, Experimental investigation of rotational molding and the characterization of rotationally molded polyetheylene-parts. Intern. Polymer Processing, 1989, IV, pp 163-171.

[31] S. Bawiskar and J. L. White, comparative study of warpage, global shrinkage, residual stresses, and mechanical behavior of rotationally molded parts produced from different polymers. Polymer Engineering and Science, 1994, 34, pp.815-820.

[32] S. J. Liu and C. Y. Ho, Experimental investigation of the warpage in rotationally molded parts, ANTEC, 1998, 1, pp. 572-576.

[33] A. Spence, Roto-blow moulding, a rotational moulding hybrid, ANTEC, 1998, 1, 984.

[34] R. J. Crawford, M. C. Cramez, M. J. Oliveira, The importance of monitoring mold pressure during rotational molding, ANTEC, 2002, 1, pp. 32-36.

[35] S. Bawiskar and J. L. White, Comparative study of warpage, global shrinkage, residual stresses, and mechanical behavior of rotationally molded parts produced from different polymers. Polymer Engineering and Science, 1994, 34, pp.815-820.

[36] http://www.paulnugent.com, 2002 (date accessed).

[37] G. Gogos, L. G. Olson and X. Liu: Cycle time predictions for the rotational molding process with and without mold/part separation. Polymer Engineering and Science, 1999, 39, pp.617-629.

[38] L. G. Olson, G. Gogos, and V. Pasham, Axisymmetric finite element models for rotational molding. International Journal of Numerical Methods for Heat & Fluid Flow, 1999, 9, pp.515-542.

[39] http://www.scudc.scu.edu/, 2002 (date accessed).

[40] R. J. Crawford, Reducing times in rotational moulding – a challenge, ANTEC, 1998, pp.1108-1111.

[41] X. M. Wang, Computer simulation of rotational moulding, PhD Thesis, Queen's University, 1995.

[42] D. W. Sun and R. J. Crawford, Computer simulation of rotational moulding heat transfer processes. Plastics, Rubber and Composites Processing and Applications, 1993, 19, pp.47-53.

[43] D. W. Sun and R. J. Crawford, Analysis of the effects of internal heating and cooling during the rotational molding of plastic. Polymer Engineering and Science, 1993, 33, pp.132-139.

[44] J. L. Throne: Rotational molding heat transfer – an update. Polymer Engineering and Science, 1976, 16 (4), 257-264.

[45] M. T. Attaran, E. J. Wright and R. J. Crawford, Computer modelling of the rotational moulding process, ANTEC, 1997, 440, pp.3210-3215.

[46] G. H. Ristow, Pattern formation in granular material. Springer Verlag: 1999.

[47] C. L. Tucker III, Computer modeling for polymer processing: fundamentals. New York: Hanser Publishers, 1989.

[48] S. Bawisker and J.L. White, Simulation of heat transfer and melting in rotational molding. Intern. Polymer Processing, 1995, X (1), pp.62-67.

[49] P. J. Nugent and R. J. Crawford, A new process control system for rotational moulding. Plastic and Rubber Processing and Application, 1992, 17, pp.23-31.

[50] P. J. Nugent, E. Little and G. Peev, The use of non-contact temperature sensing in extending process control for rotational molding, ANTEC, 1997,351, pp.3200-3204.

[51] Abu Fara, D.I, Kearns, M.P, and Crawford, R.J, System modelling for the control of the rotational molding process, ANTEC, 1999, pp.366.

[52] L. G. Olson, G. Gogos, V. Pasham and X. Liu: Numerical modeling for rotational moulding of thermoplastics, Proceedings of the ASME Heat Transfer Division, 1997, 1, pp.113-119.

[53] G. Gogos, L. G. Olson, X. Liu and V. Pasham: New model for rotational molding of plastics. Polymer Engineering and Science, 1998, 38, pp.1387-1397.

[54] X. Liang, The development of the computer simulation program for the rotomolding process, ANTEC, 1997, 112, pp.3205-3209.

[55] G. Gogos, L. Olson, X. Liu, and V. Pasham, A model for rotational moling of thermoplastics, Transactions of NAMRI/SME, 1997, 25, pp. 13-18.

[56] X. Liang and R. J. Crawford: Computer simulation of the rotational moulding process. Plastics, Rubber and Composites Processing and Applications, 1994, 20, pp.257-273.

[57] http://www.idealtech.net/warp.htm, 2002 (date accessed).

[58] Z. Tadmor and C. G. Gogos, Principles of polymer processing: 1st ed. New York: John Wiley & Sons, 1979.

[59] F. Kreith and M. S. Bohn, Principles of heat transfer. 4th edn New York: Harper & Row, 1986.

[60] C. Long, Essential heat transfer. 1st ed. Malaysia: Longman, 1999.

[61] J. H. Lienhard, A heat transfer textbook. New Jersey: Prentice-Hall, 1981.

[62] M. Kaviany, Principles of heat transfer. New York: John Wiley & Sons, 2002.

[63] F. Kreith and M. S. Bohn, Principles of heat transfer. 4th ed. New York: Harper & Row, 1986.

[64] J. Duran, Sands, Powders, and Grains: An introduction to the physics of granular materials. New York: Springer, 1997.

[65] F. P. Incropera and D. P. De Witt, Introduction to heat transfer. 2nd New York: John Wiley & Sons, 1990.

[66] J.L. Throne, Plastic process engineering. New York: Marcel Dekker, 1995.

[67] R. W. Lewis and P. M. Roberts, Finite element simulation of solidification problems. Applied Scientific Research, 1987, pp.61~92.

[68] R. W. Lewis, W. K. Sze and H. C. Huang, Some novel techniques for the finite element analysis of heat and mass transfer problems. International Journal For Numerical Method In Engineering, 1988, 25, pp.611-624.

[69] M. Samonds, Finite element simulation of solidification in sand mould and gravity die castings. PhD. Thesis, University of Swansea, 1985.

[70] K. J. Bathe, Finite element procedures in engineering analysis. New Jersey: Prentice-Hall, 1982.

[71] A. J. Dalhuijsen and A. Segal, Comparison of finite element techniques for solidification problems. International Journal For Numerical Methods In Engineering, 1986, 23, pp.1807-1829.

[72] R. W. Lewis, K. Morgon, H. R. Thomas and K. N. Seetheramu, The finite element method in heat transfer analysis. Chichester: John Wiley & Sons, 1996.

[73] W. D. Rolph III and K. J. Bathe, An efficient algorithm for analysis of nonlinear heat transfer with phase changes, International Journal For Numerical Method In Engineering, 1980, 18, pp.119-134.

[74] G. Dhatt and G. Touzot, The finite element method displayed. Chichester: John Wiley & Sons, 1984.

[75] S. Bounds, K. Davey and S. Hinduja, A modified effective capacitance method for solidification modelling using linear tetrahedral finite elements. International Journal For Numerical Methods In Engineering, 1996, 39, pp.3195-3215.

[76] K. K. Tamma and R. R. Namburu, Recent advances, trends and new perspectives via enthalpy-based finite element formulations for applications to solidification problems. International Journal For Numerical Method In Engineering, 1990, 30, pp.803-820.

[77] Y. Jaluria and K. E. Torrance, Computational heat transfer. Washington: Hemisphere Publishing Corporation, 1986.

[78] M. Salcudean and Z. Abdullah, On the numerical modelling of heat transfer during solidification process. International Journal For Numerical Method In Engineering, 1988, 25, pp.445-473.

[79] V. R. Voller and C. R. Swaninathan, Fixed grid techniques for phase change problems: A Review. International Journal For Numerical Method In Engineering, 1990, 30, pp.875-898.

[80] J. N. Reddy, An introduction to the finite element method. 1st ed. New York: McGrew-Hill, 1984.

[81] G. Comini, S. Del Guidice and O. Saro, Conservative equivalent heat capacity methods for nonlinear heat conduction (Inadequate information).

[82] J. N. Reddy and D. K. Gartling, The finite element method in heat and fluid dynamics. Boca Raton: CRC Press, 2000.

[83] E. Pardo and D. C. Weckman, A fixed gird finite element technique for modelling phase change in steady-state conduction-advection problems. International Journal For Numerical Method In Engineering, 1990, 29, pp.969-984.

[84] M. J. Mundim and M. Fortes, An accurate finite element method of solution of phase change problems – based on enthalpy diffusion, pp.79-89 (Inadequate information).

[85] J. Roose and O. Storrer, Modelization of phase changes by fictitious heat flow. International Journal For Numerical Method In Engineering, 1982, 20, pp.217-225.

[86] K. Davey and I. Rosindale, Control volume capacitance method for solidification modelling. International Journal For Numerical Methods In Engineering, 1999, 46, pp.315-340.

[87] D. Burnett, Finite element analysis: from concepts to applications. 1st ed. New Jersey: Addison-Wesley, 1987.

[88] G. Comini and S. Del Guidice, Finite element solution of non-linear heat conduction problems with special reference to phase change. International Journal For Numerical Method In Engineering, 1974, 8, pp.613-624.

[89] K. Morgan, R. W. Lewis and O. C. Zienkiewicz, An improved agorithm for heat conduction problems with phase change. International Journal For Numerical Method In Engineering, 1977, pp.1191-1195.

[90] A. S. Usmani, R. W. Lewis and K. N. Seetharamu, Finite element modelling of natural-convection-controlled change of phase. International Journal For Numerical Method In Engineering, 1992, 14, pp.1019-1036.

[91] M. Samonds, R. W. Lewis, K. Morgan and R. Symberlist, Finite element modelling of the mold-metal interface on casting simulation with coincident nodes or thin elements. Chapter 13 in Computational Techniques In Heat Transfer; 1st ed. Swansea: Pineridge Press, 1985, pp.331-354.

[92] J. S. Hsiao and B. F. Chung, An efficient algorithm for finite element solution to two-dimensional heat transfer with melting and freezing. Transaction of The ASME, May 1986, 108, pp.462-464.

[93] R. J. Crawford and P. J. Nugent, Impact strength of rotationally moulded polyethylene articles. Plastic, Rubber and Composites Processing and Applications, 1992, 17, pp.257-273.

[94] J. L Throne, Some factors influencing cooling rates of rotationally molded parts. Polymer Engineering and Science, 1972, 12, pp.335-339.

[95] J. Godinho, A. M. Cunha, and R. J. Crawford, Property variations across the wall thickness of rotationally moulded polyethylene products, ANTEC, 1996, pp.2848-2852.

[96] V. Nassehi, Practical aspects of finite element modelling of polymer processing. Chichester: John Wiley & Sons, 2002.

[97] C. Taylor and T. G. Hughes, Finite element programming of the navier-stroke equations. Swansea: Pineridge Press Limited, 1981.

[98] L. G. Olson, R. Crawford, M. Kearns, and N. Geiger, Rotational Molding of Plastics: Comparison of Simulation and Experimental Results for an Axisymmetric Mold. Polymer Engineering And Science, 2000, 40, pp.1758-1764.

[99] Y. O. Kwon and H. C. Bang, The finite element method using MATLAB. 2nd ed. Baca Raton: CRC Press, 2000.

[100] J. H. Mathews and K. D. Fink, Numerical methods using MATLAB. 3rd ed. U.S.A: Prentice Hall, 1999.

LIST OF PUBLICATIONS

[1] K. K. Lim, A. Ianakiev and J.B. Hull, Numerical Modeling For Rotational Molding With Non-Isothermal Heating, Journal of Plastic, Rubber and Composites: Macromolecular Engineering, 2003, 32, 10, pp. 421-430.

[2] K. K. Lim, A. Ianakiev and J.B. Hull, Predictions of heating cycle for rotational molding with non-isothermal heating, LUXFEM Conference (1st International Conference on Finite Element Application), Luxemburg, 2003.

[3] K. K. Lim and A. Ianakiev, Two-dimensional slip-flow model of rotational molding, ANTEC, Chicago, 2004, 1, pp. 892-896.

[4] K. K. Lim and A. Ianakiev, Numerical studies on phase change algorithm and warpage/non-warpage problem under various process conditions of rotational molding, ANTEC, Chicago, 2004, 1, pp. 897-901.

APPENDIX A

BASIC VERIFICATION OF FINITE ELEMENT CODES

A simple test has been carried out to verify the essential finite element codes of the program before utilizing them for the research. An example of transient heat conduction, taken from Kwon and Bang [99, pp.140], was chosen due to its basic similarities on the governing energy equation and appropriate boundary conditions with the present research.

Problem:

A plate of size $0.02m$ by $0.01m$, whose heat of conduction coefficient is $k = 0.3W/mC$, is initially at a temperature of $300\,^0C$. While its left and right sides are maintained at the same temperature of $300\,^0C$, the bottom side is insulated and the topside is subjected to heat conduction with a convection coefficient of $h_c = 100W/m^2C$ and an ambient temperature of $50\,^0C$. The material has a density $\rho = 1600kg/m^2$ and a specific heat $c = 0.8J/kgC$. The governing energy equation of this problem is (similar to Equation (3-1)):

$$\rho c\frac{\partial T(x,y,t)}{\partial t} = \nabla(k\nabla T(x,y,t)) \qquad \text{on}\,\Omega \qquad \text{(A-1)}$$

Discussion:

The present finite element mesh is shown in Figure A-1. Satisfactory predicted results are obtained, as shown in Figure A-2. The results, therefore, verify the accuracy of the present finite element codes.

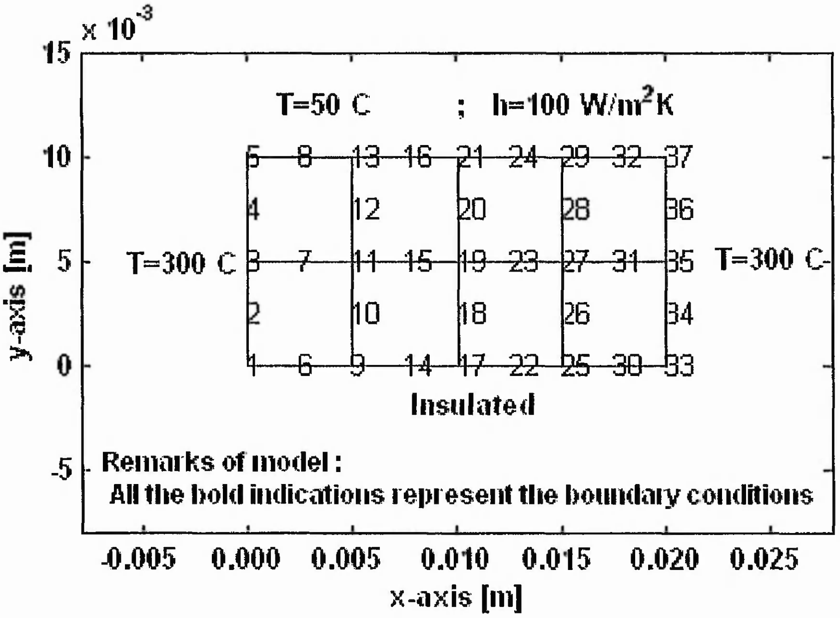

Figure A-1: Finite element mesh of the present eight-noded rectangular element

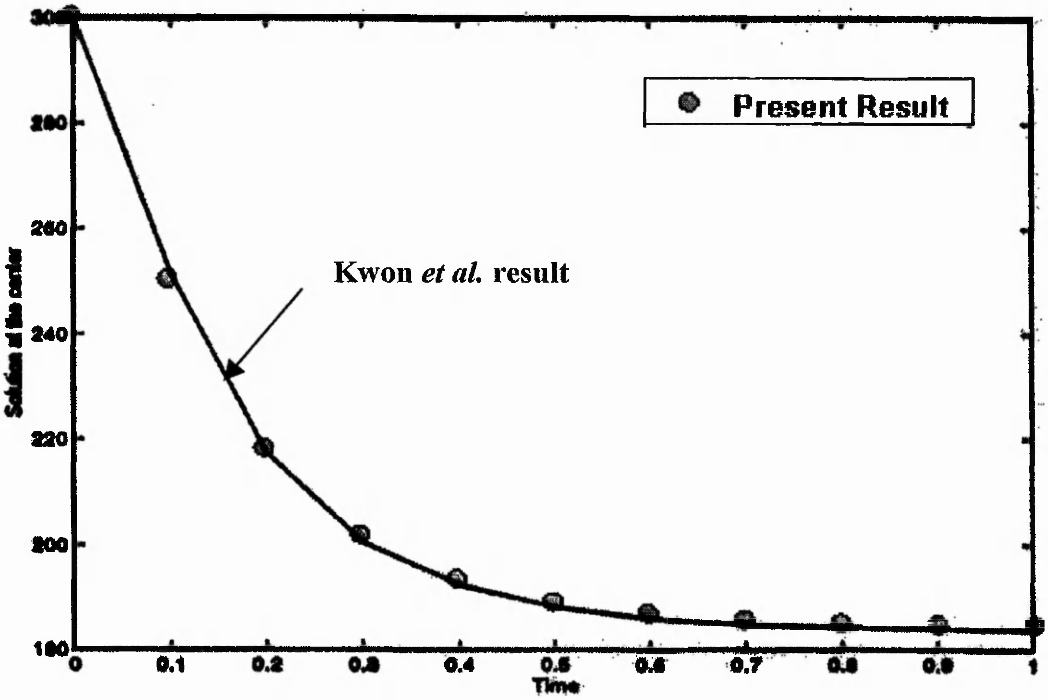

Figure A-2: Comparisons between Kwon et al. and present results

APPENDIX B

RotoFEM PROGRAM STRUCTURE

B.1 Preface of RotoFEM Program

RotoFEM (Rotomoulding Finite Element Modelling) program has been developed for the 2-D thermal modelling of the rotational moulding process. The program was developed based on the multi-layered deposition method (MDM), and it can simulate the heat transfer processes of rotational moulding for up to $12\,mm$ thick parts.

The RotoFEM program consists of two sections - heating and cooling simulations. Each section of the program can be further divided into four mains parts; data inputs, 2-D mesh generation, FEM analysis, and output displays (line plots, contour plots or movie displays). Providing the dimensions (thickness, width and height) of the mould and the part thickness can generate the mesh. Only half of the heating square model will be used for the cooling modelling. This is because of the symmetrical cooling assumption. In addition, the observation points (nodes of data plotting) will be auto-generated at appropriate locations to make the modelling procedure more convenient.

RotoFEM can simulate the problems of phase change, warpage, external heating, external cooling and external-internal cooling. During the external heating or cooling simulation, the internal air temperature is used to monitor the optimum heating and cooling times. The demoulding time is based on the selected nodal temperatures at the centre of the part thickness for the external-internal cooling simulation.

B.2 Structure of RotoFEM and Slip Flow Models

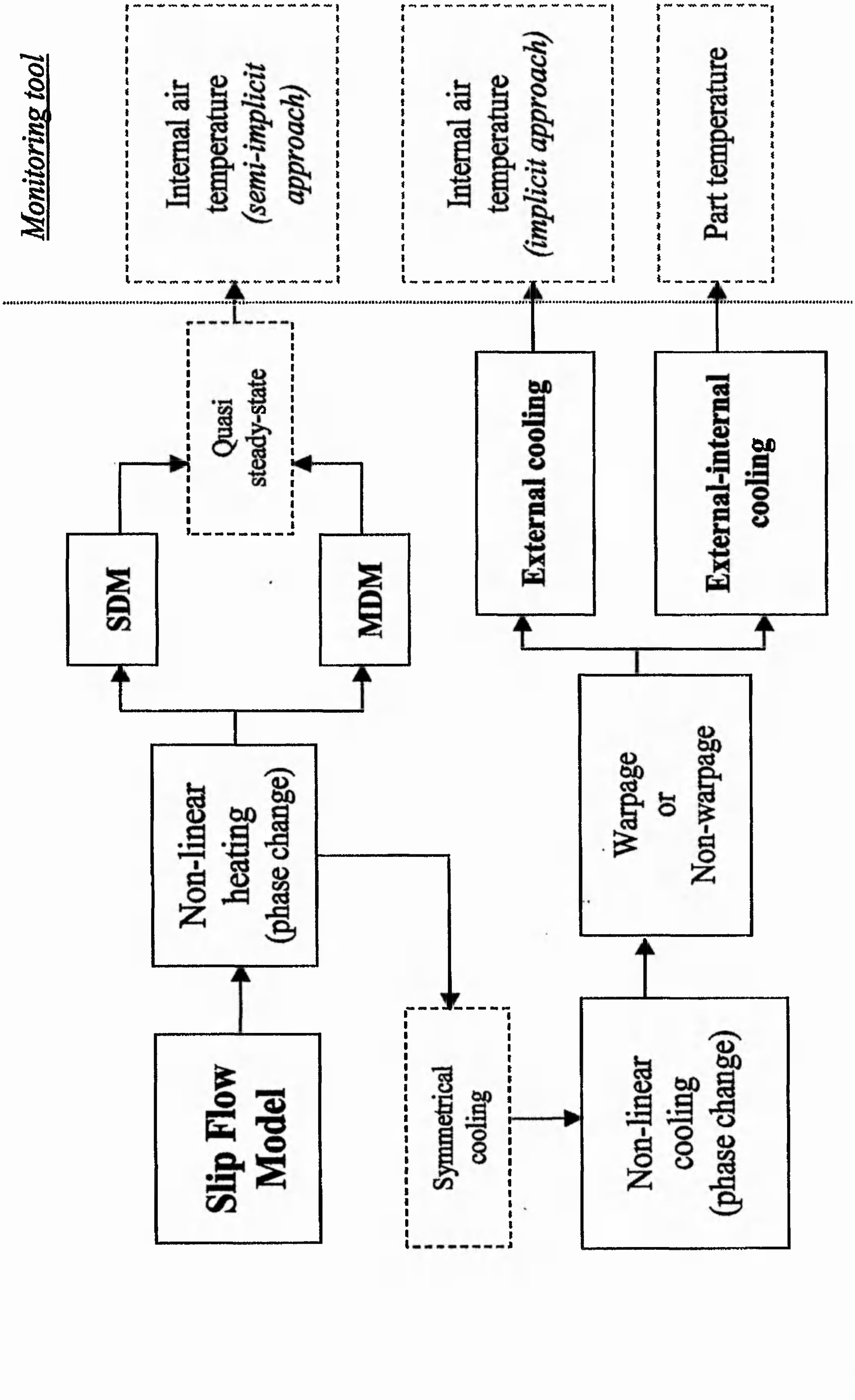

B.3 Data Input for RotoFEM Program

B.3.1 Primary Data Input of Heating Process:

(i) Number of Mesh.

(ii) Initial temperature: Default - same for all materials (mould, polymer and internal air).

(iii) 'Deheating' temperature of internal air: The maximum internal air temperature allowed before the heating cycle is end.

(iv) Oven temperature.

(v) Mould Dimension: width, height and thickness.

(vi) Plastic part thickness.

(vii) Mould and internal fluid properties: specific heat, density and thermal conductivity.

(viii) Non-linear discrete types of polymer properties: specific heat, density and thermal conductivity.

(ix) Temperature margins for the solid, tacky, mushy and liquid polymer phases.

(x) Heat transfer coefficients for the external and internal air.

(xi) Iterative time step, ∂t.

(xii) Convergent criteria: The smaller the value, the faster the ∂t iteration may converge.

B.3.2 Primary Data Input of Cooling Process:

(i) Cooling method: External cooling 'or' External-internal cooling

(ii) External cooling temperature

(iii) Internal cooling temperature

(iv) Demoulding internal air temperature

(v) Warpage simulation: Yes or No

(vi) Warpage location: Centre warpage 'or' Corner warpage

(vii) Warpage criteria 1: Crystalline melting temperature (temperature which a polymer part reaches before warpage appears)

(viii) Warpage criteria 2: Thickness of solid layers reaches the crystalline melting temperature before warpage appeals.

- 50% of part thickness
- 100% of part thickness

(ix) Non-linear discrete type of polymer properties: specific heat, density and thermal conductivity.

(x) Temperature margins for the solid, tacky, mushy and liquid polymer phases.

(xi) Heat transfer coefficients for the external and internal cooling air.

B.4 Main Manual of RotoFEM Code

1. RotoFEM.m: The main program used to simulate the heating and cooling cycles of the rotational moulding process. It contains m-files '*E8RotHeat.m*' and '*E8RotCool.m*', which represent the key heating and cooling programs, respectively.

2. E8RotHeat.m: The program used to model the heating cycle. All the input parameters for the heating cycle are defined in this file, which consists of the following key subroutines:

   (i) E8HProp.m: Data of material properties.

   (ii) E8HMesh.m: Mesh generation.

   (iii) E8HSlipflow.m: Global node renumbering during the *slip flow heating.*

- (iv) E8HEqnCp.m: To compute the non-linear polymer properties.
- (v) E8HGInt.m: To form the global stiffness matrix for the coincident node technique.
- (vi) E8HGMtTAM.m: To evaluate the mass exchange inside the mould due to the thermal interactions between the mould, internal air and external air interface.
- (vii) E8HGMtTAP.m: To evaluate the mass exchange inside the mould and construct the global matrix of the internal air due to the thermal interactions between the polymer, internal air and external air.
- (viii) E8HMovie.m: Movie and contour displays.
- (ix) E8HPlot.m: Temperature profile plot.

3. E8RotCool.m The program used to model the cooling cycle. All the input parameters for the cooling cycle are defined in this file, which consists of the following key subroutines:
    - (i) E8CProp.m: Data of material properties.
    - (ii) E8CCoorLw.m: Coordinated system for warpage or non-warpage simulations.
    - (iii) E8CMeshLw.m: Mesh generation for warpage simulation.
    - (iv) E8CMesh.m: Mesh generation for non-warpage simulation.
    - (v) E8CNLEqn.m: To compute the non-linear polymer properties.
    - (vi) E8CDirectsol.m: Direct solver for the linear problem during the initial cooling stage.
    - (vii) E8CWarpCr: Checking for demoulding criteria.
    - (viii) E8CReNode: Global node renumbering when warpage first appears.

(ix) E8CGInt.m: To form the global stiffness matrix for the coincident node technique.

(x) E8CGMtTAP.m: To evaluate the mass exchange inside the mould due to the thermal interactions between the polymer, internal air and external air.

(xi) E8CContour.m: Contour display.

(xii) E8CMovie.m: Movie display.

(xiii) E8CPlot.m: Temperature profile plot.

B.5 Flow Chart of RotoFEM Solution Procedure

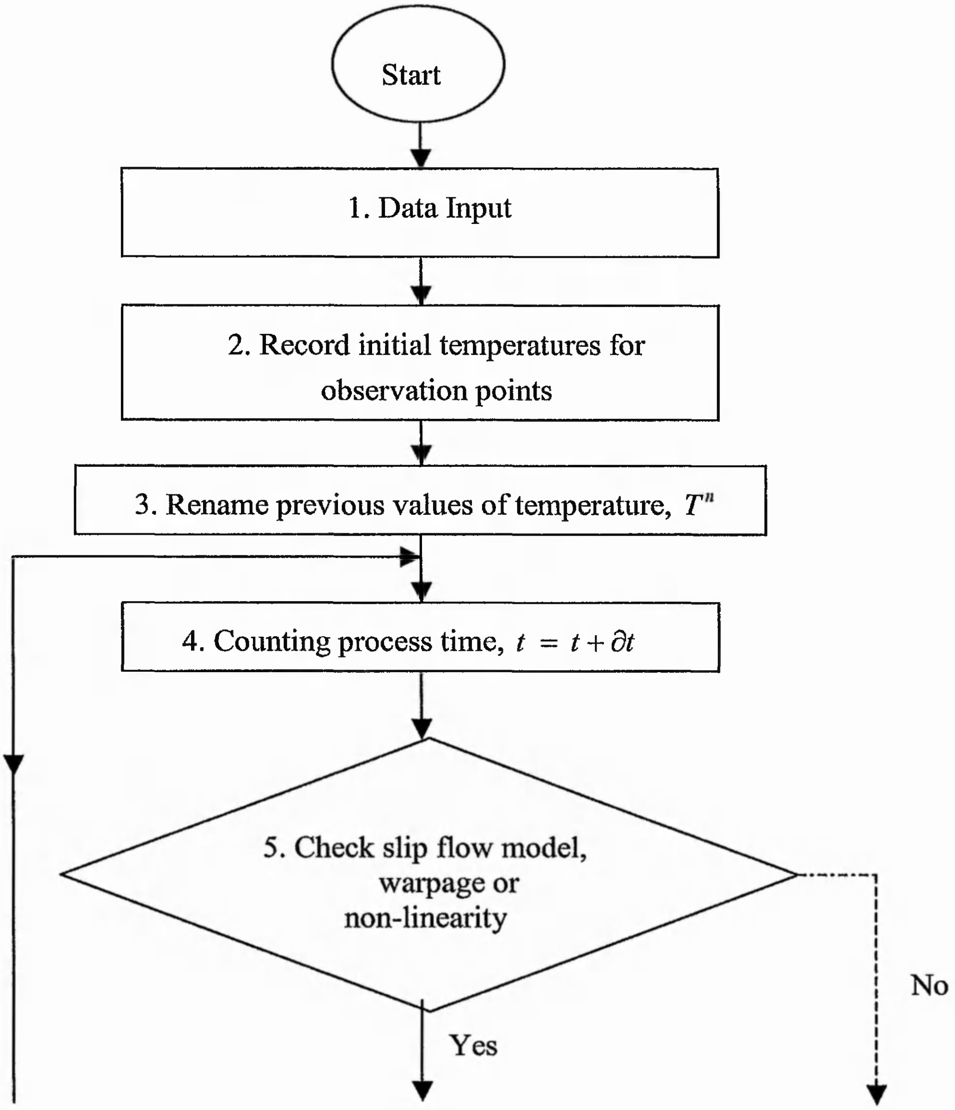

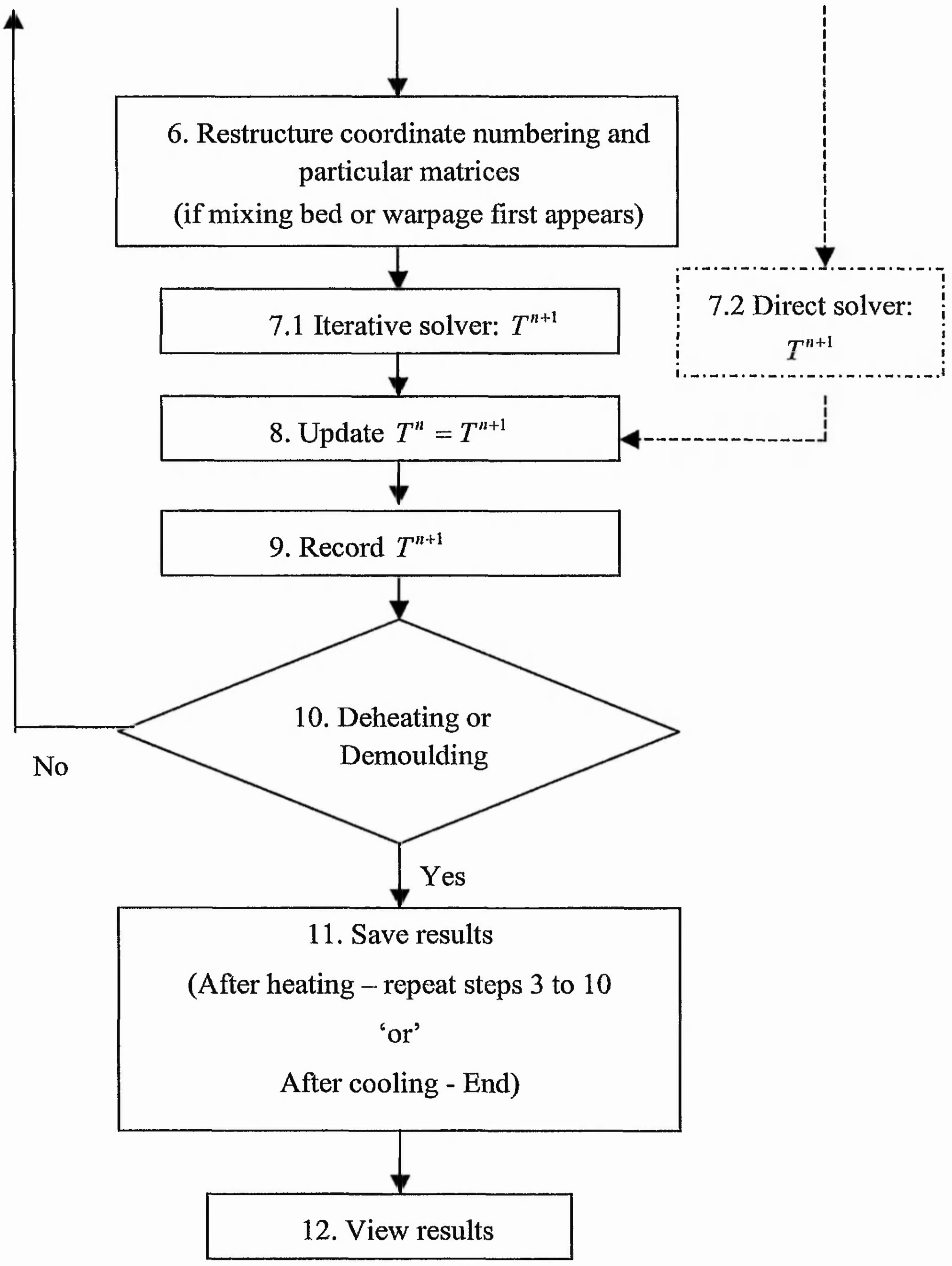
6. Restructure coordinate numbering and particular matrices
(if mixing bed or warpage first appears)
7.1 Iterative solver: T^{n+1}
7.2 Direct solver: T^{n+1}
8. Update $T^{n} = T^{n+1}$
9. Record T^{n+1}
10. Deheating or Demoulding
No
Yes
11. Save results
(After heating – repeat steps 3 to 10
'or'
After cooling - End)
12. View results